A Feasibility Study for an Astrophysical Linear Formation Flying Space Interferometer

Jonah Hansen

A thesis submitted for the degree of
Bachelor of Philosophy (Honours) - Science
with Honours in Astronomy & Astrophysics of
The Australian National University

October, 2019

Acknowledgements and Declaration

Firstly, I want to thank Associate Professor Michael Ireland for supervising me and providing me with support when the project started to lead me down the wrong path. You've been a lot of help, even when you were away for three months, and I absolutely couldn't have done this without you. Thanks also to the RSAA Planets group, who've provided some great ideas to help keeping my project moving forward.

I'd also like to thank all of my fellow honours students, from both astronomy as well as physics and other disciplines. You've been a great support through both the good and bad times. Specifically, I'd like to thank James Beattie, Ella Wang, Wei Shen Oh, Alex Soen, Brendan Orenstein, Patrick Williamson and Adam Rains for helping to edit various parts of my work. Your insights have helped considerably to making this the best thesis that I could have written.

Finally, I'd like to thank my friends, family and churches (Crossroads and Immanuel Woden) for always being there for me. Especially my parents, Mark and Anne, who called me weekly to make sure I was keeping sane. August was a hard period, but your words of encouragement really got me through it all and I wouldn't have this final product without you all.

Also, a special shoutout to Avatar The Last Airbender, which provided me with a means of procrastination during the final week leading up to the submission deadline, and wisdom through the advice of Uncle Iroh.

This thesis is an account of research undertaken between February 2019 and October 2019 at The Research School of Astronomy and Astrophysics, College of Science, The Australian National University, Canberra, Australia.

Except where acknowledged in the customary manner, the material presented in this thesis is, to the best of my knowledge, original and has not been submitted in whole or part for a degree in any university.

Jonah Hansen
October, 2019

Abstract

Space interferometry is the inevitable endpoint of high angular resolution astrophysics, and a key technology that can be leveraged to analyse exoplanet formation and atmospheres with exceptional detail. However, cost blowouts of large missions such as *Darwin* and TPF-I, and inadequate technology readiness levels have resulted in limited developments since the late 2000s. Here, we present a feasibility study into a small scale interferometric array, flying in Low Earth Orbit, that will aim to prove the technological concepts involved with space interferometry while still conducting exciting science. Through the development of equations that capture satellite motion due to the J_2 oblateness of the Earth, we simulate the satellite array to determine whether an ambitiously simple design of one thruster per satellite is enough to maintain a stable interferometer. We find that this design is indeed enough; around 10% of the Δv budget per orbit is used to correct for this perturbation. We also conduct observability simulations to identify what parts of the sky are visible for a given orbital configuration. We find that the main limiting factor is the antisolar angle, the maximum angle between the target star and the point opposite the sun. In engineering the design of this array, this angle must be pushed to be as large as possible in order to obtain maximum coverage of the sky. We conclude with optimism that this design is achievable, but a more detailed control simulation factoring in a metrology system is the next step to demonstrate full mission feasibility.

Nomenclature

Acronyms

Symbol	Description	SI Units
AITC	Advanced Instrumentation and Technology Centre	
ASP	Astrophysical Space-interferometry Pathfinder	
ECI	Earth-centred inertial (frame)	
ELT	Extremely Large Telescope	
ESA	European Space Agency	
HCW	Hill-Clohessy-Wiltshire (equations)	
JWST	James Webb Space Telescope	
LEO	Low Earth Orbit	
LIFE	Large Interferometer For Exoplanets	
LVLH	Local vertical, local horizontal (frame)	
NASA	National Aeronautics and Space Administration	
PFI	Planet Formation Imager	
SAMSI	Spacecraft Array for Michelson Spatial Interferometry	
TPF	Terrestrial Planet Finder	
VLTI	Very Large Telescope Interferometer	

Roman symbols

Symbol	Description	SI Units
$\boldsymbol{a}$	Acceleration vector	$\mathrm{m\,s^{-2}}$
A	Amplitude	–
A	Area	$\mathrm{m^2}$
$\Delta\boldsymbol{b}$	Baseline separation vector ($2 \times \Delta\boldsymbol{r}$)	m
C	Drag coefficient	–

D	Optical path difference	m
d	Optical path length	m
E	Electric field	–
$\boldsymbol{F}$	Force vector	N
F	Flux	$\mathrm{W\,m^{-2}}$
G	Envelope modulation function	–
g	Standard gravitational acceleration	$\mathrm{m\,s^{-2}}$
H	Scale height	m
h	Orbital angular momentum	$\mathrm{kg\,m^2\,s^{-1}}$
I	Intensity	$\mathrm{W\,s^{-1}\,m^{-2}}$
i	Inclination	Rad
I_{sp}	Specific impulse	s
J_2	Earth's oblateness perturbation amplitude	–
J_n, C_m^n, S_m^n	Dimensionless geopotential coefficients	–
k	Wavenumber	$\mathrm{m^{-1}}$
$\boldsymbol{M}$	Change of basis matrix	–
m	Mass	kg
P_m^n	Legendre polynomial	–
$\boldsymbol{Q}$	Quaternion rotation function	–
$\boldsymbol{q}$	Quaternion	–
$\Delta\boldsymbol{r}$	Spacecraft separation vector	m
$\boldsymbol{r}$	Position vector	m
R	Radius	m
r	Radial position	m
r_0	Fried parameter	m
T	Period	s
t	Time	s
U	Potential	J
Δv	Delta v	$\mathrm{m\,s^{-1}}$
$\boldsymbol{v}$	Velocity vector	$\mathrm{m\,s^{-1}}$

V	Visibility	–
$\boldsymbol{X}, \boldsymbol{Y}$	Satellite state vectors	–
Z	Altitude	m

Greek symbols

Symbol	**Description**	**SI Units**
α, δ	Right ascension / declination	Rad
β, λ	Ecliptic latitude / longitude	Rad
γ	Antisolar angle	Rad
δ	Phase difference	Rad
ε	Obliquity of the ecliptic	Rad
θ, ϕ	Polar / azimuthal angle	Rad
θ	Argument of latitude	Rad
κ_n	HCW/Schweighart coefficients	m
$\Delta\lambda$	Wavelength bandpass	m
Λ	Coherence length	m
λ	Wavelength	m
μ	Standard gravitational parameter	$\mathrm{N\,m^2\,kg^{-2}}$
ρ	Atmospheric density	$\mathrm{kg\,m^{-3}}$
τ	Coherence time	s
φ	Phase	Rad
ψ	Angular separation of spacecraft	Rad
Ω	Longitude of the ascending node	Rad
ω	Angular velocity	$\mathrm{s^{-1}}$

Coordinate systems

Symbol	**Description**	**SI Units**
$\mathcal{I}$	ECI frame	–
$\hat{\boldsymbol{x}}, \hat{\boldsymbol{y}}, \hat{\boldsymbol{z}}$	ECI unit vectors	m
$\mathcal{L}$	LVLH frame	–
$\hat{\boldsymbol{\rho}}, \hat{\boldsymbol{\xi}}, \hat{\boldsymbol{\eta}}$	LVLH unit vectors	m
$\mathcal{C}$	Curvilinear LVLH frame	–

$\hat{\boldsymbol{b}}, \hat{\boldsymbol{o}}, \hat{\boldsymbol{s}}$	Baseline unit vectors	m
$\mathcal{B}$	Baseline frame	–
$\hat{\boldsymbol{u}}, \hat{\boldsymbol{v}}$	UV unit vectors	m

Constants from the modified Schweighart & Sedwick (2002) model

Symbol	Description	SI Units
c	Schweighart angular velocity correction	–
k	Schweighart constant	s^{-1}
l	Schweighart cross-track constant	$\mathrm{m\,s}^{-1}$
q	Schweighart cross-track constant	s^{-1}
α	Schweighart motion equation constant	s^{-1}
β	Schweighart motion equation constant	–
γ	Schweighart motion equation constant	–
δ	Schweighart motion equation constant	–
ζ	Schweighart motion equation constant	m
ϕ	Schweighart cross-track constant	Rad
σ	Schweighart constant	s^{-1}

Subscripts

Symbol	Description	SI Units
$\oplus$	Earth	–
c	Chief	–
d	Deputy	–

Other symbols

Symbol	Description	SI Units
Υ	Vernal equinox	–

Contents

Acknowledgements and Declaration iii

Abstract v

Nomenclature vii

1 Introduction 1
- 1.1 The case for space interferometry . . . 1
- 1.2 The basics of interferometry . . . 3
- 1.3 Interferometry in astrophysics . . . 7
  - 1.3.1 Developments in space-based interferometry . . . 9
- 1.4 The Astrophysical Space-interferometer Pathfinder . . . 13
  - 1.4.1 A pathway towards space interferometry . . . 13
  - 1.4.2 Mission design . . . 13
- 1.5 Thesis outline . . . 15

2 Orbit Determination 16
- 2.1 Coordinate frames . . . 16
  - 2.1.1 ECI - Earth-centred inertial frame . . . 16
  - 2.1.2 LVLH - Local vertical, local horizontal frame . . . 16
  - 2.1.3 Curvilinear LVLH frame . . . 17
  - 2.1.4 Baseline frame . . . 19
- 2.2 LVLH orbit determination . . . 20
- 2.3 ECI orbit determination . . . 22
  - 2.3.1 Defining the chief orbit . . . 22
  - 2.3.2 Determining the deputy orbits . . . 23

3 Orbital Perturbations 27
- 3.1 Non-perturbed motion . . . 27
- 3.2 The J2 perturbation . . . 30
  - 3.2.1 The geopotential model . . . 30
  - 3.2.2 J2 in the LVLH frame . . . 30
- 3.3 Atmospheric drag . . . 36

4 Orbital Corrections and Constraints 39
- 4.1 The delta-v budget . . . 39
- 4.2 Correcting during integration . . . 40
- 4.3 Correcting the rest of the orbit . . . 41
  - 4.3.1 One orbit . . . 41
  - 4.3.2 Multiple orbits . . . 43
- 4.4 Reconfiguring the orbit . . . 43
- 4.5 Summary . . . 46

5 Observability of the Satellite Array **48**
5.1 Is it observable? 48
5.1.1 The Sun 48
5.1.2 The Earth 50
5.2 Satellite sky coverage 51
5.3 Filling the UV plane 56

6 Conclusion and Future Work **59**

Bibliography **61**

A Appendix **65**
A.1 Quaternions 65
A.2 The geopotential model 67
A.3 Derivation of the J2 LVLH equations of motion 70

Chapter 1

Introduction

1.1 The case for space interferometry

Since the first confirmed exoplanet detection of 51 Peg b by Mayor & Queloz (1995), there has been a desire to directly image and study exoplanets without relying on indirect methods such as transits and radial velocity measurements. While these methods have produced a large number of exoplanet detections since 51 Peg b, they are limited by selection biases and do not allow many of the properties of the planet to be studied. In particular, one of the major goals of exoplanet research is identifying potentially habitable worlds that may harbour life. To determine this, one would need to study the atmosphere of the planet. Radial velocity techniques cannot provide atmospheric information, and current transmission spectroscopy is not precise enough to obtain high quality data (Defrère et al., 2018).

This is where direct imaging becomes important - by directly imaging an exoplanet, it is possible to obtain information about the atmosphere and surface, and therefore determine if a "biosignature" is present. According to Léger et al. (2011), a biosignature is "an observable feature of a planet, such as its atmospheric composition, that our present models cannot reproduce when including the abiotic physical and chemical processes we know about". Biosignatures were first studied by Sagan et al. (1993), who used the Galileo probe to look back at Earth and determine if a biosignature could be found *a priori*. This study was successful, finding that a multitude of molecules such as O_2 were significantly out of thermodynamical equilibrium and were inexplicable through abiotic processes. Extending this analysis to exoplanets is a tantalising research goal.

However, many obstacles stand in the way of direct imaging of an exoplanet. The most prominent of these concerns separating the emission of the planet from that of its host star. As calculated by Angel & Woolf (1997), the contrast between the star and a 300 K terrestrial planet (using the Sun/Earth ratio as an analogue) is an astounding 10^{10} in visible light. That said, a judicious choice of wavelength can reduce this contrast by multiple orders of magnitude; viewing in the mid-infrared (10 μm) reduces the contrast to 10^7 (Angel & Woolf, 1997). The contrast over different wavelengths can be seen in the plot by Defrère et al. (2018) (Fig. 1.1). There are other reasons for choosing the mid-infrared as well - Angel et al. (1986) found that there are multiple molecular lines between 7 and 17 μm, specifically H_2O at 7 μm, O_3 at 9.7 μm and CO_2 at 15 μm. O_3 is particularly useful as it can be used as a tracer for O_2. These molecules are ideal for determining biosignatures, especially for life on Earth as we know it.

While the mid-infrared contains many advantages over the visible, there are still two main complications. The first issue is that while the emission from a 300 K exoplanet peaks in the mid-infrared, the Earth's emission peaks as well. Fridlund (2002) finds

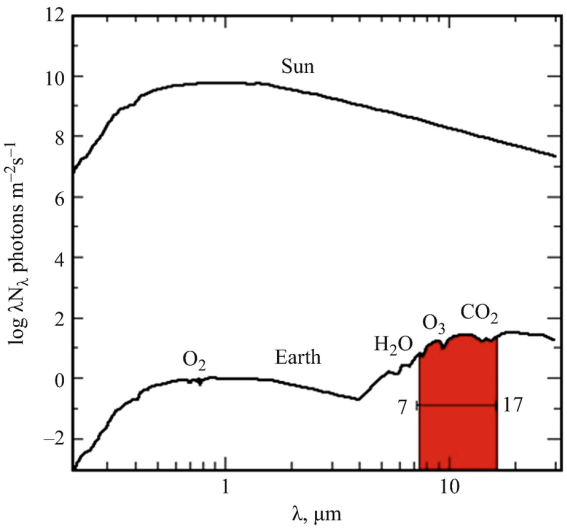

Figure 1.1: Contrast between the Sun and the Earth (as analogues for a terrestrial exoplanet system) for different wavelengths as viewed from 10 pc away. Also contains molecular signatures that are conducive to detecting biosignatures. Plot obtained from Defrère et al. (2018).

that ground-based telescopes would be overwhelmed by their own 300 K emission at wavelengths longer than 1.7 μm, as well as having to manage the bright atmospheric emission. A telescope located in space would not have these issues as it would not have to compensate for the atmosphere and could be passively cooled to far below 300 K.

The other main issue regarding exoplanet imaging is the angular resolution required: for a planet 1 AU out from a host star at 10 pc, an angular separation of 0.1″ would be required. This corresponds to a mirror diameter of at least 60 m for a conventional aperture telescope (Angel & Woolf, 1997), a size double that of the Extremely Large Telescope (ELT) class telescopes currently being constructed. Hence, even for a mid-infrared space telescope such as the James Webb Space Telescope (JWST), exoplanet imaging is out of reach due to the angular resolution required (Defrère et al., 2018). For this reason, interferometry was found to be the ideal method to circumnavigate this issue, as an interferometric baseline can function as a large aperture. With interferometry, one can achieve high spatial resolution with small apertures; ideal for space-based telescopes (Angel & Woolf, 1997). Quanz et al. (2018) also find that a mid-infrared interferometer would be complementary to or even better than an optical/near-infrared space telescope at detecting exoplanets. This is significant as the costs for a large scale space-based mid-infrared interferometric mission (such as *Darwin*) would be more economical ($\sim$\$1.2B (Cockell et al., 2009)) than the equivalent space-based optical telescope (e.g. LUVIOR at $<$ \$10B National Aeronautics and Space Administration (2019)).

These two problems regarding sensitivity and angular resolution are related to each other. For example if one was to look for exoplanets of a fixed temperature around a dim M type star, while the sensitivity requirements would be lower, the angular resolution requirements would be larger. This is due to the distance of the habitable zone of a stellar system being inversely related to the stellar flux of the star (Kasting et al., 1993). A plot from Defrère et al. (2018) in Fig. 1.2 illustrates the relation between the angular resolution and sensitivity required for different types of stars. Thus, in order to study a majority of terrestrial planets without selection biases, one cannot simply neglect one

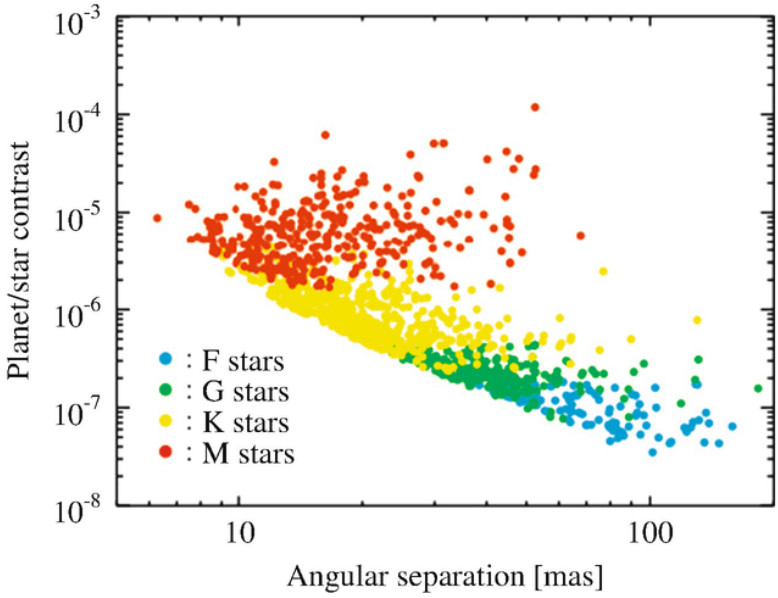

Figure 1.2: Contrast between a planet and star compared with their angular separation for different types of stars. Due to the inverse relationship, in order to image exoplanets to the fullest extent, one must have high sensitivity as well as high angular resolution. Plot obtained from Defrère et al. (2018).

of these problems - both must be addressed. Fig. 1.3 shows the relationship between the sensitivity and angular resolution requirements for various stars, comparing the current and potential capabilities of ground and space-based telescopes. As can be seen, space-based telescopes such as JWST will have the sensitivity to start probing these systems, but lack significantly in angular resolution. Conversely, the ELT class of telescope will just have the angular resolution but not the sensitivity required due to their location on the ground. For these reasons, space-based interferometry has been deemed the best way forward in directly imaging exoplanets (Fridlund, 2002).

1.2 The basics of interferometry

Interferometry is the science of measuring the interference of electromagnetic waves (Lawson, 2000). It is emerging as an important tool in astronomy, as it allows access to high angular resolution measurements of objects that single aperture telescopes simply cannot achieve; whether that be due to cost or from a fundamental engineering standpoint. A brief description of how an astronomical interferometer functions follows.

If we consider two telescopes with positions $\boldsymbol{x_1}$ and $\boldsymbol{x_2}$, the separation between the two is known as the baseline of the system $\Delta\boldsymbol{b} = \boldsymbol{x_2} - \boldsymbol{x_1}$. Then let us consider a star located at a position $\boldsymbol{s}$ from the centre of the pair of telescopes. The 'pointing' direction, or star vector, is then given by $\hat{\boldsymbol{s}}$. Using the scalar field approximation, we find that the monochromatic electromagnetic fields incident on each telescope are given by

$$\begin{aligned} E_1 &= A_1 e^{-ik\hat{\boldsymbol{s}}\cdot\Delta\boldsymbol{b}} e^{-i\omega t} \\ E_2 &= A_2 e^{-i\omega t}, \end{aligned} \tag{1.1}$$

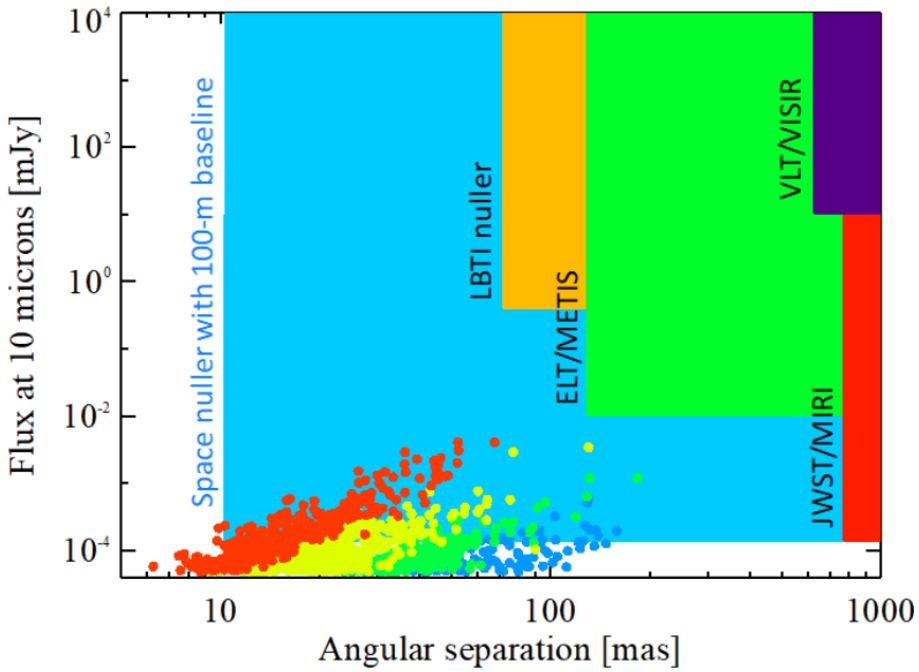

Figure 1.3: Capabilities for directly imaging Earth like exoplanets with various ground and space-based telescopes. Only a space interferometer will allow us to probe a significant sample of these planets. Figure taken from Defrère et al. (2018).

where k is the wavenumber of the field and ω is the angular frequency (Haniff, 2007). Fig. 1.4, taken from Lawson (2000), illustrates this setup. If we assume that the waves are then propagated through different optical paths, d_1 and d_2, and are directly combined at a detector, we find the fields obtain further phase differences ($\delta_j = kd_j$) based on these lengths. Just before entering the combiner, the electric fields can be described by:

$$\begin{aligned} E_1 &= A_1 e^{-ik\hat{\boldsymbol{s}}\cdot\Delta\boldsymbol{b}} e^{-i\omega t} e^{-ikd_1} \\ E_2 &= A_2 e^{-i\omega t} e^{-ikd_2}. \end{aligned} \tag{1.2}$$

Now, an optical detector measures the time averaged intensity (denoted by $\langle\rangle$) of the incident electric fields (Haniff, 2007):

$$I = \langle |E|^2 \rangle = \langle E^* E \rangle. \tag{1.3}$$

An interferometer measures the superposition of the two electric fields arriving from the two telescopes. If we assume equally sensitive telescopes (setting $A_1 = A_2 = A$), then the detected intensity is given by:

$$\begin{aligned} I &= \langle |E_1 + E_2|^2 \rangle \\ &= \langle |E_1|^2 \rangle + \langle |E_2|^2 \rangle + \langle E_1 E_2^* \rangle + \langle E_2 E_1^* \rangle \\ &= A^2 (2 + e^{-i(kd_1 + k\hat{\boldsymbol{s}}\cdot\Delta\boldsymbol{b} - kd_2)} + e^{i(kd_1 + k\hat{\boldsymbol{s}}\cdot\Delta\boldsymbol{b} - kd_2)}) \\ &= 2A^2 (1 + \cos k(d_1 - d_2 + \hat{\boldsymbol{s}} \cdot \Delta\boldsymbol{b})). \end{aligned} \tag{1.4}$$

The quantity $D = d_1 - d_2 + \hat{\boldsymbol{s}} \cdot \Delta\boldsymbol{b}$ is known as the optical path delay or optical path difference of the measurement. In the space of a delay, the power will vary harmonically

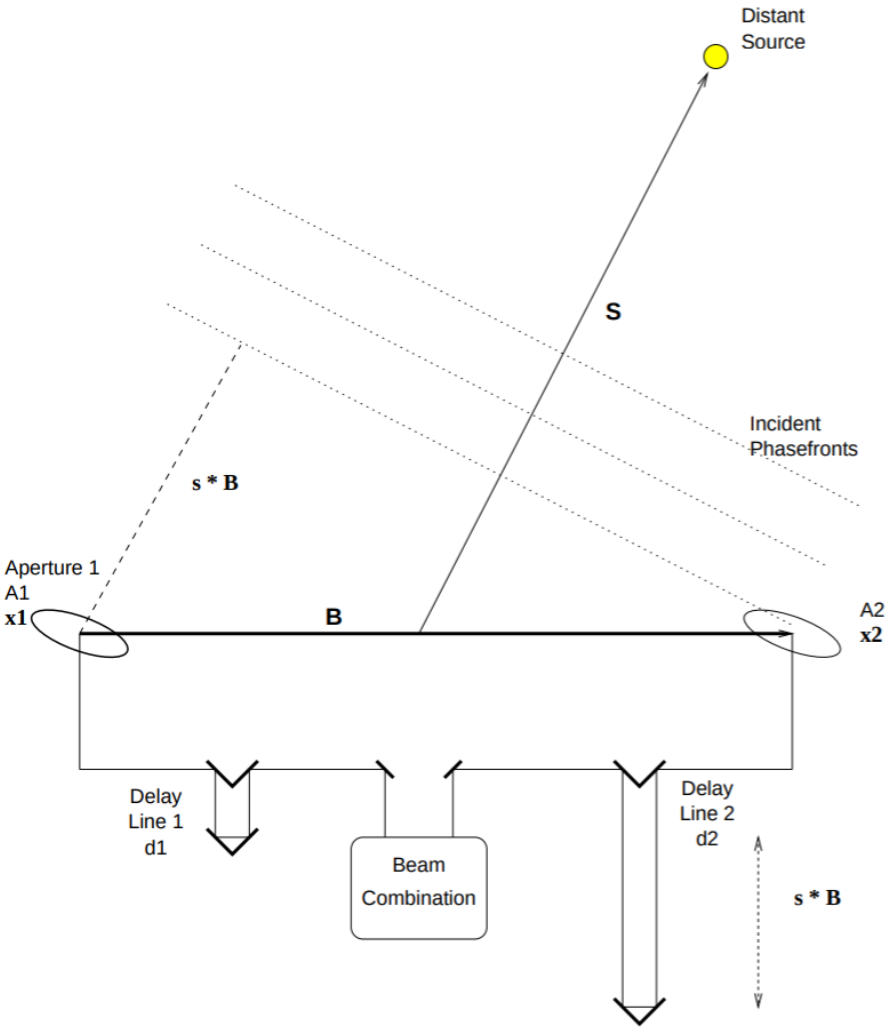

Figure 1.4: A simple interferometer setup, taken from Lawson (2000). Here $\mathbf{B} = \Delta \boldsymbol{b}$ represents the baseline of the interferometer, consisting of telescopes at $\mathbf{x_1}$ and $\mathbf{x_2}$. The position of the target star is denoted $\boldsymbol{s}$, and d_1/d_2 are the two different optical paths (modified through delay lines).

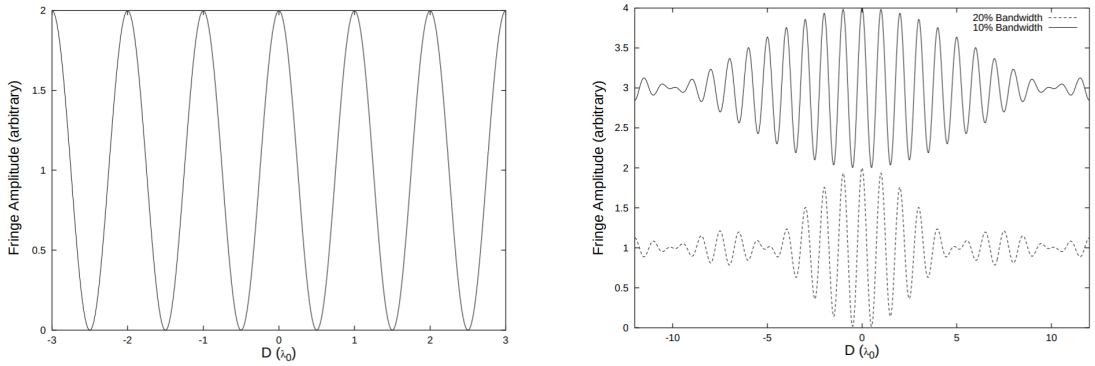

(a) Monochromatic (b) Polychromatic

Figure 1.5: Comparison of the coherence of the interference fringes for monochromatic and polychromatic interferometers. It is given as a function of the optical path delay D. Retrieved from Lawson (2000).

with a period equal to the wavelength of light λ. If we then consider then moving the star vector $\hat{\boldsymbol{s}}$, we see that the adjacent maxima of the power oscillations are found at angular separations $\Delta s = \frac{\lambda}{\Delta b}$. This shows that the theoretical angular resolution that an interferometer can achieve is only determined by the wavelength of light observed and the baseline of the telescopes. The larger the baseline or shorter the wavelength, the better the resolution.

However, interferometers function with a finite bandpass and are hence polychromatic, leading to complexity in the measurement. Haniff (2007) shows that, assuming a uniform response pattern over a wavelength band $\Delta\lambda$ centred at λ_0, the resultant polychomatic intensity is given by

$$\begin{aligned} I &= 2A^2\Delta\lambda\left[1+\frac{\sin\left(\pi D\Delta\lambda/\lambda_0^2\right)}{\pi D\Delta\lambda/\lambda_0^2}\cos(kD)\right] \\ &= 2A^2\Delta\lambda\left[1+\operatorname{sinc}(\pi D/\Lambda)\cos(kD)\right]. \end{aligned} \tag{1.5}$$

A comparison of the monochromatic and polychromatic intensity of the interference fringes is shown in Fig. 1.5. The intensity is effectively the same, except that instead of a constant fringe amplitude, the fringes are modulated by a sinc function with a characteristic scale of

$$\Lambda = \frac{\lambda_0^2}{\Delta\lambda}. \tag{1.6}$$

This quantity is known as the coherence length. The sinc function in equation 1.5 is simply a product of the bandpass function chosen: the modulation function is the Fourier transform of the bandpass. Thus, for generality, the fringe envelope can be written as

$$1 + G(\Lambda, D)\cos(kD), \tag{1.7}$$

where G is the envelope modulation function. Due to this modulation, the signal drops off considerably when offset from $D = 0$. Essentially, Λ determines how precise the delays must be matched in order to maintain maximum power in the fringes (Lawson, 2000).

Considering two separate unresolved sources (such as a star and a planet), Buscher & Longair (2015) show that the resultant combined intensity distribution is simply the sum of each separate intensity distribution:

$$I_{\text{total}} = I(A_1, \hat{\boldsymbol{s}}_1) + I(A_2, \hat{\boldsymbol{s}}_2). \tag{1.8}$$

For an extended source, it is useful to define a quantity known as the complex visibility, given by Lawson (2000) as

$$V(u,v) = \int F(\alpha,\beta) e^{-2\pi i(\alpha u + \beta v)} d\alpha d\beta, \tag{1.9}$$

where F is the brightness distribution of the object as a function of angle on the sky. The relationship between the output intensity and complex visibility is treated in Buscher & Longair (2015):

$$I \propto A(1 + \text{Re}(V(u,v)e^{-ikD})). \tag{1.10}$$

The spatial frequencies u and v are defined by

$$u \equiv \frac{k\Delta b_x}{2\pi} \qquad\qquad v \equiv \frac{k\Delta b_y}{2\pi}. \tag{1.11}$$

Fundamentally, we want to measure the complex visibility, as the flux/brightness distribution is simply the Fourier transform of the visibility. This relation is commonly known as the van Cittert-Zernike theorem (van Cittert (1934); Zernike (1938)). If an interferometer makes visibility measurements spanning a large number of spatial frequencies u and v, one can perform a discrete Fourier transform to identify the brightness distribution of the object. The quality of the distribution is a strong function of the u, v plane coverage - the more measurements taken with different baseline lengths and position angles, the better the image.

Now, it is very difficult to measure the phase of the complex visibility for a two element interferometer. This is because the phase requires knowledge of a reference star path length in an inertial coordinate system to an extremely precise degree. For example, to measure phase to within 3 degrees (a signal to noise ratio of $\sim$20) at visible wavelengths, this reference path length has to be known to within 5 nm. Instead, we can use a technique known as differential phase referencing, where a broad part of the continuum of a spectrum serves as a reference for the phase, and this reference is applied to a narrow science region of interest (Monnier, 2003). For example, if the continuum comes from an unresolved source (say a quasar with a compact core), the reference path length can be computed from this source. Then the emission flux surrounding this continuum emission (e.g. the broad line region around a quasar) can be imaged, with the centre of the image being the unresolved source.

1.3 Interferometry in astrophysics

Interferometry has been invaluable in allowing astronomers to achieve high angular resolution not possible with photometry and spectroscopy. Perhaps one of the best known uses of interferometry is the measurement of stellar diameters. Fizeau (1868) was the first to suggest that one could determine the stellar diameters of the sources

by analysing the interference fringe contrast. However, it was only with the work of Michelson & Pease (1921) that this hypothesis was able to be tested; they calculated the diameters of stars using baselines larger than 3 m.

During this time, McCready et al. (1947) were the first to use interferometry in the radio domain. As a result of the large wavelength, the coherence length is much longer and thus is easier to work with. This led to huge leaps in resolution for radio astronomy, as the long wavelength requires either gigantic telescopes or long baselines. The field of radio astronomy continues to heavily rely on interferometry: the world's current largest radio interferometer, the Event Horizon Telescope, took an image of the event horizon of the black hole at the centre of M87 this year (Akiyama et al., 2019).

Optical interferometry stalled, however, due to the difficulty in dealing with the short coherence length. It was only with the work of Labeyrie (1975), coinciding with the invention of new detectors and other technologies, that the field was re-energised. Labeyrie (1975) was the first to combine the light from two separated telescopes working with optical light to produce interference fringes. This work has continued to this day, and has been instrumental in determining the effective temperatures of stars through an accurate measurement of the angular diameter (Boyajian et al., 2012).

Interferometry has had many other breakthrough discoveries. Rousselet-Perraut et al. (2010) were able to use VEGA instrument on the CHARA interferometer to spatially and spectrally resolve the Hα emission line on the Herbig Ae star AB Aur, which was then used to probe the accretion process of the star. Even more excitingly, the high angular resolution of the PIONIER instrument on the Very Large Telescope Interferometer (VLTI) has allowed stellar surfaces to be directly imaged in the near-infrared without reliance on models (Ohnaka et al. (2017); Paladini et al. (2018)). Stellar surface imaging through interferometry has even allowed us to investigate stellar atmospheric properties, such as convection and starspots, on stars other than the Sun (Roettenbacher et al., 2016).

The Planet Formation Imager (PFI) (Monnier et al., 2018) is a proposed mid-infrared interferometer that aims at imaging the formation process of exoplanets and early planetary systems. It consists of twelve 3 m class telescopes arranged in either a Y or ring array, providing an angular resolution of 0.6 mas at $3.5\,\mu$m or 1.7 mas at $10\,\mu$m. This will allow for the ability to resolve the protoplanetary disks for nearby stars, but will not go far enough to image an exoplanet specifically. However, a space version of PFI, based on the work developed in this thesis, may become a step towards the eventual goal of detecting exoplanetary biosignatures.

Stars and exoplanets are not the only objects that can be studied with interferometry; quasars are also prime candidates, being bright objects that require high angular resolution. The additional presence of a compact central core and a larger, broad line region also allows differential phases to be calculated easily (see Section 1.2). Using the GRAVITY instrument on the VLTI, GRAVITY Collaboration (2018) measured the quasar 3C 273 in unprecedented detail, achieving a resolution of 10^{-5}", which is less than 1 pc in linear distance. Through these measurements, they were able to identify the mass of the black hole, the radius of the accretion disk and the inclination of the disk which matched radio jet observations.

However, GRAVITY Collaboration (2018) also highlighted that ground-based interferometry is currently limited to objects with magnitudes < 12 in the infrared. This is due to atmospheric turbulence, which for interferometry is quantified by the coherence time $\tau \equiv \frac{r_0}{v_{\text{wind}}}$, where r_0 is the Fried parameter (a measure of the quality of optical transmission through the atmosphere) and v_{wind} is the wind speed (Monnier, 2003). The

coherence time sets a limit as to how long the integration can be before the phase of the measured visibility moves more than one radian due to the atmosphere. At 500 nm, $r_0 \sim 10$ cm, and assuming a wind speed of 10 m/s, we arrive at a coherence time of $\tau = 10$ ms. This is an incredibly short integration time, which results in the bright magnitude limit. The main benefit of a space-based interferometer is that we can negate this limit by removing the atmosphere and having a coherence time on the order of 10 s. This is an increase in gain of 1000, leading to an increase of the magnitude limit by 7.5 mag.

Even more recently, and more directly related to this work, Lacour et al. (2019) used GRAVITY on the VLTI to directly image the exoplanet HR 8799e using interferometry. This was the first time that extremely high resolution data was obtained for an exoplanet, in particular a spectrum of the exoplanet's atmosphere. Using this spectrum, Lacour et al. (2019) were able to identify the composition of the planet, finding an atmosphere with a large excess of carbon monoxide and clouds of iron and silicate dust. Such observations have not been possible before, highlighting the importance of high sensitivity, high angular resolution measurements that can only be obtained using optical interferometry. However, it should be noted that all current and proposed interferometers are currently ground-based, leading to restrictions in the integration time and sensitivity due to the atmosphere.

1.3.1 Developments in space-based interferometry

The first design of a space-based interferometer for the purpose of exoplanet research was proposed by Bracewell (1978). His design, known as a nulling interferometer, was the basis for most of the interferometers designed in future years. A nulling interferometer is designed to enhance the planet's light over the power of the star by placing an interference null over the star. This is achieved by having two incident beams of light with the same optical path length and introducing a phase shift of π on one of them (Fridlund, 2004). The light then destructively interferes at the central minimum and constructively interferes at an angle $\theta = \lambda/2\Delta b$ away from the central minimum. If the baseline of the interferometer is adjusted so that the planet is an angle θ away from the star, then the planet's emission is maximised while most of the star's light is removed. The contrast is then limited to light leaks from the the central minimum due to optical and mechanical imperfections (Fridlund, 2004).

While a single two-element nulling interferometer would achieve high angular resolution and sensitivity, there are other issues that need to be addressed. In particular, the zodiacal light from our own solar system would outshine the residual light at 10 μm from a nulled star at 10 pc by a factor of 1000, creating a background-dominated regime (Mennesson & Mariotti, 1997). To compensate for this, Angel & Woolf (1997) proposed using a four-element interferometer, rather than the regular two elements. This configuration is essentially two superimposed Bracewell interferometers with different spacings to provide a very broad and deep central minimum, as well as narrower fringes to separate the diffuse dust and unresolved planets. Other methods of discriminating against the zodiacal light include switching geometrical arrangements or moving the telescopes to modulate the planet signal with respect to the dust (Fridlund, 2002). Léger et al. (1996) proposed to simply locate the interferometer at 4-5 AU, so that the zodiacal dust would not pose a problem. Finally, Martinache & Ireland (2018) presented a technique that allows for a robust exoplanet detection in the presence of optical phase

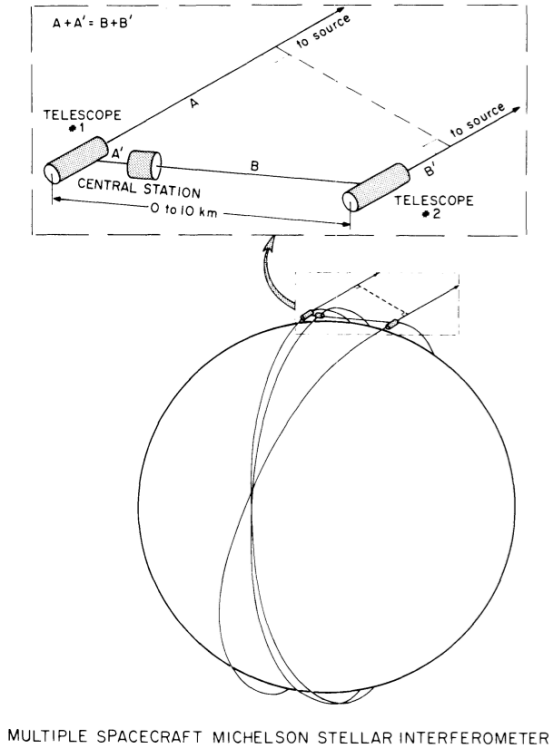

Figure 1.6: Schematic of the SAMSI mission in Low Earth Orbit. Taken from Stachnik et al. (1984).

perturbations without requiring a very deep minimum.

As well as local zodiacal dust, exozodiacal dust must also be considered. As Mennesson & Mariotti (1997) points out, even if an interferometer was located at 4-5 AU from the sun, the exozodiacal light would outshine a 1 AU planet by a factor of 400, and after nulling would still produce a contrast on the order of 30. The eventual solution to this issue was to have an asymmetrical configuration of telescopes, which when rotated would allow the planet and exozodiacal light to be distinguished without ambiguity. This configuration eventually developed into the *Darwin* mission, described later in this chapter (Léger et al., 1996).

Space interferometry was studied extensively in the 1980s and 1990s, particularly by the European Space Agency (ESA) who identified it as a key goal in the Horizon 2000 plan (Fridlund, 2002). As a result of this, many proposals and concepts for missions were developed over several conferences and workshops. Among these were rigid structures such as COSMIC (Traub & Carleton, 1985) and FLUTE (Labeyrie et al., 1980), and free flying interferometers such as OASIS (Noordam et al., 1985), TRIO (Labeyrie et al., 1985) and SAMSI (Stachnik & Gezari, 1985). The last two are of particular note. The TRIO proposal eventually led to the development of the *Darwin* mission (Labeyrie et al., 2000). The other proposal, SAMSI, shares some details in common with the interferometric array that we will investigate in this thesis. It should be noted that all of these proposals are not refereed papers or concepts that reached a preliminary design phase and should be treated as concepts at a feasibility study level.

SAMSI (Spacecraft Array for Michelson Spatial Interferometry) consisted of three telescopes in Low Earth Orbit at identical orbits but for differing inclinations, shown

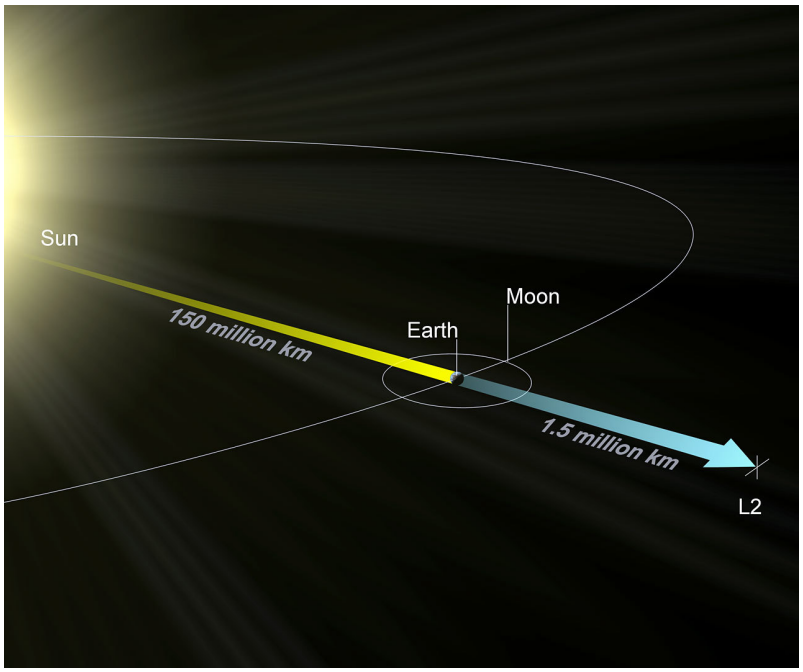

Figure 1.7: Schematic of the location of the L2 Lagrange point compared to the Earth, Moon and Sun. Taken from European Space Agency (2013).

in Fig. 1.6 (Stachnik et al., 1984). The central spacecraft is situated at the equioptical path position of the system, so that the optical path difference between the two side spacecraft is minimised. An optical delay line would then be used to correct for the remaining difference. The SAMSI array would be located at 1000 km above the Earth, where it was deemed that J_2 (the perturbation due to Earth's oblateness) and solar perturbations would be the main perturbations to consider. Atmospheric drag was neglected due to the high altitude of the orbits. Finally, Stachnik et al. (1984) considered that with a 10 km baseline, the interferometer could achieve 10^{-5}" resolution and potentially a magnitude limit of 15-20.

After these initial proposals, two flagship missions were devised: NASA's Terrestrial Planet Finder (TPF) mission (Beichman et al., 1999) and ESA's *Darwin* mission (Léger et al., 1996). Both of these missions were free flying arrays of satellites orbiting around the Sun-Earth L2 point. The L2 Lagrange point is a good location for space observation, as a satellite maintains roughly the same position with respect to the Earth and the Sun. A diagram of the location of L2 with respect to the Earth's orbit is shown in Fig. 1.7.

TPF aimed to study terrestrial exoplanets using four 3.5 m telescopes and one central spacecraft holding the beam combiner, observing at wavelengths between 7-20 μm (Beichman et al., 1999). The particular arrangement was originally the double Bracewell proposed by Angel & Woolf (1997), but eventually became an "Emma X-array", an arrangement consisting of the four telescopes flying in rectangular formation and the beam combiner located about 1200 m above the array (Defrère et al., 2018). Two pathfinder missions were initially identified to demonstrate the technology required for TPF (the Space Interferometry Mission SIM (Shao, 1998) and the Starlight mission (Blackwood et al., 2003)). However neither of the pathfinders, and eventually TPF itself, were funded due to budget cuts in 2007.

Similarly, *Darwin* was originally designed to have six 1.5 m satellites in a hexagonal

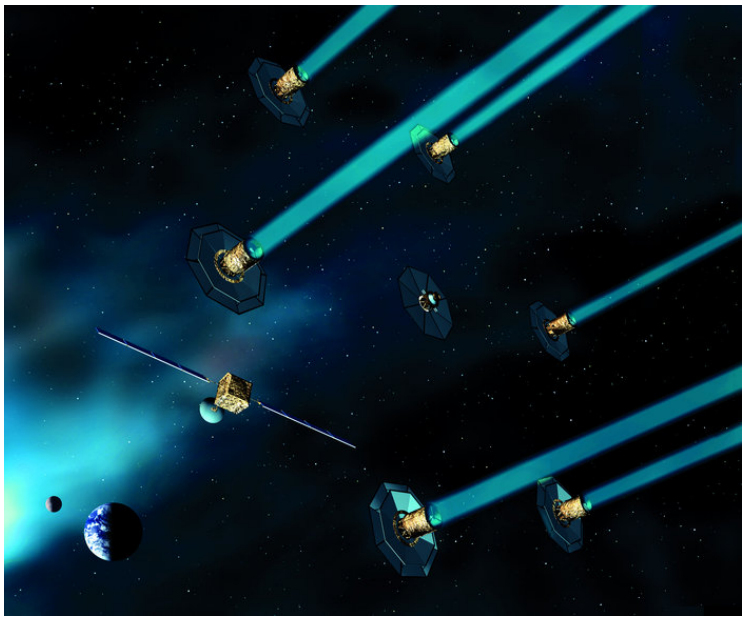

Figure 1.8: Artist concept of the *Darwin* spacecraft in an early configuration. Retrieved from European Space Agency (2003).

configuration, operating between $5 - 10\,\mu$m, with a beam combiner in the middle (Fridlund, 2004). This configuration was designed to allow the use of multiple baselines for better nulling (Angel & Woolf, 1997) and to allow for two dimensional imaging of an exoplanet system. An artist concept of the original *Darwin* satellite constellation is shown in Fig. 1.8. The baselines were designed to be tuned to an individual star so that the habitable zone was always at the angle of maximal constructive interference, a baseline typically around 1 km. In order to distinguish the planet signal from the exozodiacal light, the whole system was designed to be rotated and switched asymmetrically between different orientations, so that the signal was modulated. Eventually, *Darwin* also adopted a four telescope/one beam combiner "Emma X-array" configuration near the end of the design study (Cockell et al., 2009). Again, due to budget cuts, *Darwin* was not funded and ceased being investigated in 2007. ESA is currently planning for the next 30 years as part of the Voyage 2050 process, and a revised *Darwin*-like mission LIFE (Large Interferometer For Exoplanets) (Quanz et al. (2018); Quanz et al. (2019)) is part of the discussion.

A final notable mission proposal is that of *Pegase* (Le Duigou et al., 2006). *Pegase* was to be located at the Sun-Earth L2 Lagrange point and consisted of a linear array of three spacecraft - two light collecting telescopes and a beam combiner. The baseline was designed to be adjustable from 50-500 m, with an angular resolution from 1-20 mas. Le Duigou et al. (2006) designed *Pegase* as a simple two-element Bracewell interferometer. While studies from Angel & Woolf (1997) found this was insufficient to detect terrestrial exoplanets and could not separate exozodiacal light from the planet signal, this was unimportant for *Pegase*, which was to search for hot Jupiters with a much higher flux and at a shorter wavelength (2.5-5 μm) than that of *Darwin*. Like the previous missions, *Pegase* did not move beyond the design phase.

The geometry of *Pegase* is very similar to the array studied in this thesis and can provide insight into the formation flying mechanisms that need to be considered. *Pegase* had a two level control structure: a coarse level control at the satellite level, and fine control at the optics level (Le Duigou et al., 2006). The fine control loops consisted of

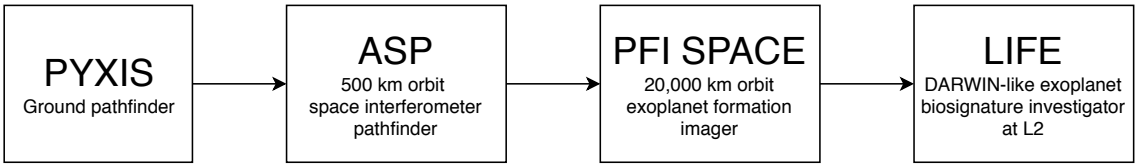

Figure 1.9: A proposed pathway towards achieving high sensitivity space interferometry.

displacing optical delay lines inside the central spacecraft, as well as moving fast steering mirrors. With these controls, the central fringe should be kept steady, as long as the satellites are stable during integration time. To account for this, the coarse control loop split the integration time into short periods of 100 s where the satellite is left drifting under natural perturbations. Then, every two integration periods, thrusters would be used to correct for the perturbations, disrupting the fringe tracking for a short period of time. The fine control loop used integration times of 20 ms. In Chapter 4, we investigate whether a similar model might be adopted for our space interferometer pathfinder.

1.4 The Astrophysical Space-interferometer Pathfinder

1.4.1 A pathway towards space interferometry

The biggest issue with the previous attempts of space interferometry by NASA and ESA was the lack of feasible, smaller scale pathfinders that would allow a development of the technology needed for a large scale mission. Hence, here we propose a pathway that will take steps towards achieving the full technology needed to detect biosignatures on exoplanets. The pathway is shown in Fig. 1.9.

We propose to start with a ground-based robotic system that demonstrates the configuration and interferometric capabilities of an array of satellites. This ground pathfinder, named Pyxis, is awaiting the outcome of an ARC discovery grant proposal (Ireland, DP20). Afterwards, a small nano-satellite array would be launched into orbit to prove the technology developed in the Pyxis stage. Due to the costs of launching, this array would likely be put in Low Earth Orbit (LEO). The next step would be to put a larger satellite array in Mid Earth Orbit, that could act as a space-based version of the current ground-based instrument PFI (Planet Formation Imager). While not sensitive enough to analyse the spectrum of exoplanets, it would be able to detect planets in the process of forming and contribute massively to the field of exoplanet formation. Finally, the flagship sized *Darwin*-type mission at L2 (LIFE) would be ready, having had the various technologies developed in stages and with less uncertainty as to whether this approach is feasible.

1.4.2 Mission design

We now return to stage two in the pathway, a LEO mission with the aim to demonstrate the feasibility of an optical interferometer in space, temporarily named ASP: the Astrophysical Space-interferometer Pathfinder. This thesis' purpose is to investigate the orbital dynamics and observability constraints of such a mission. This mission will be working in the optical part of the spectrum; this is due to the challenges with mid-infrared interferometric technologies (such as earthshine preventing a cooled LEO mission), and the need for ensuring that space interferometry is feasible before

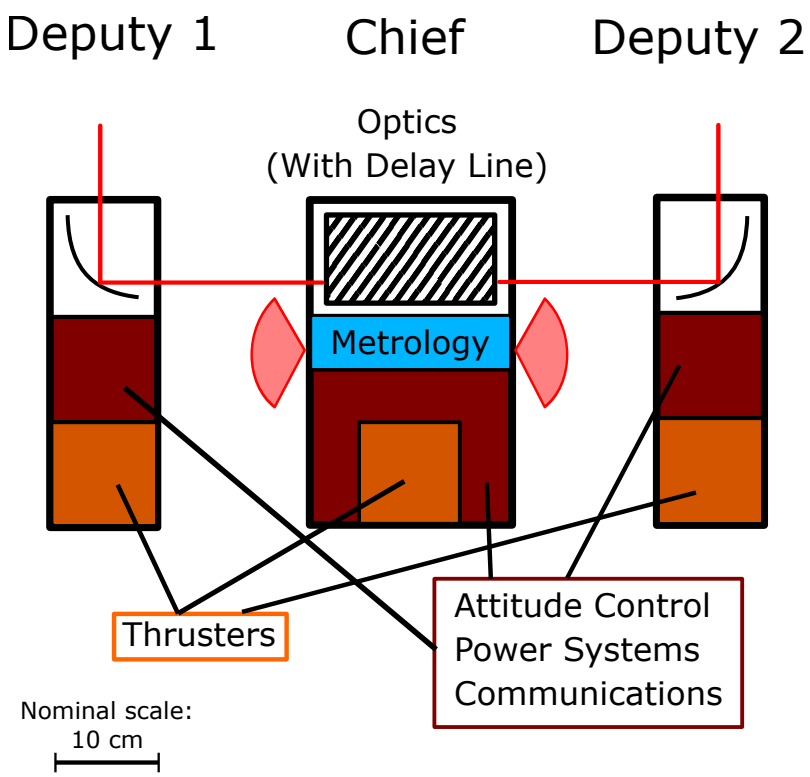

Figure 1.10: Preliminary design of the Astrophysical Space-interferometer Pathfinder (ASP) Mission.

introducing more complications. We also anticipate that this mission will have an altitude of about 500 km and a lifetime of three years.

Our proposed design is to have a linear array of three nano-satellites, two telescopes (hereby called the deputies) and one beam-combiner (called the chief). The telescopes would ideally be 3U CubeSats to minimise cost, containing the optical system, solar power system, attitude control and a single thruster. The beam-combiner would be larger: a 6U CubeSat with the required interferometric optics (including a delay line), ideally one thruster, a solar power system, metrology system, attitude control and communication system. A diagram of this initial design, with required space for each subsystem, is shown in Fig. 1.10. This is an ambitious design in terms of space requirements, and also thruster requirements as each satellite will only have a single thruster.

To comfortably keep track of interference fringes, we need to keep the optical path between the two arms of the interferometer within the coherence length of the beam-combiner. The optical path difference is given by the equation

$$D = |\Delta \boldsymbol{r}_1| - \Delta \boldsymbol{r}_2 \cdot \hat{\boldsymbol{s}} - |\Delta \boldsymbol{r}_2| + \Delta \boldsymbol{r}_2 \cdot \hat{\boldsymbol{s}} \approx 0, \tag{1.12}$$

where $\Delta \boldsymbol{r}$ is the separation of one of the deputies from the chief, and $\hat{\boldsymbol{s}}$ is the unit vector in the direction of the star. To resolve velocities of 100 km/s per spectral channel with a central wavelength of 658 nm, we have to distinguish wavelengths separated by

$$\Delta\lambda = \lambda \frac{v}{c} = 0.2\,\text{nm}$$

This results in a coherence length of about 2 mm. However, an optical delay line inside the beam combiner should be able to alleviate the requirements on the satellites themselves, as was proposed for the *Darwin* mission (Karlsson & Kaltenegger, 2003). If the 6U form factor is adopted, then we can assume 20 cm of space for this line. As this must compensate for both satellites, and because increasing the delay on one satellite will decrease the delay on the other, we have a total tolerance of about 5 cm. Hence, we need to keep the satellites in position such that the optical path difference between the two is less than 5 cm. To achieve this we require an accurate and precise metrology system to know how much to adjust the delay line. The metrology system is not covered in this thesis.

The ultimate aim of this project is to investigate whether this design will be sufficient in terms of thrust and manoeuvrability, so that the array is able to conduct interferometry in a LEO environment.

1.5 Thesis outline

The starting point for this feasibility study was a set of slides from a ten minute presentation given earlier this year, as well as an ARC discovery proposal for Pyxis; a ground-based technology prototype for a linear interferometric array. All work in this thesis continues on from these two documents.

Orbital simulations will be created from scratch, since sophisticated spacecraft dynamics software is proprietary and does not cover sub-orbit motions in great detail, focusing instead on long term orbital motions. The stringent requirement on the optical path difference requires us to examine these sub-orbit perturbed motions carefully, and so a ground-up simulation gives us better insight than preexisting software. This approach also provides greater flexibility by allowing us to analyse the motion in reference frames that have greater scientific significance, such as one with unit vectors in the direction of the interferometer baseline and the target star direction. Finally, we can conduct sky coverage simulations built on the same code, eliminating the requirement to construct an entirely new simulation.

The thesis outline is as follows. In Chapter 2, we will detail the various coordinate frames required and the orbital configuration for the satellites. In Chapter 3 we will introduce perturbations into the orbits, particularly the J_2 gravitational perturbation and atmospheric drag. Chapter 4 outlines a full numerical simulation, designed to identify the thrust and Δv required to keep the satellites in formation. Finally, Chapter 5 explores the sky coverage of the interferometer, its performance in filling the UV plane and potential science targets for the array.

Chapter 2

Orbit Determination

In this chapter, we will introduce the four coordinate frames that will be useful in the development and analysis of the orbital configuration of the satellite array. We will then briefly prove that a linear array will allow us to achieve an optical path difference of zero, before then identifying how such a configuration is defined in an inertial geocentric frame of reference.

2.1 Coordinate frames

2.1.1 ECI - Earth-centred inertial frame

The Earth-centred inertial (ECI) frame is a basic inertial coordinate frame $\mathcal{I}$, centred on Earth with the $\hat{\boldsymbol{z}}$ axis pointing towards true north, $\hat{\boldsymbol{x}}$ pointing towards the Vernal Equinox (Υ) and $\hat{\boldsymbol{y}}$ completing a right-handed coordinate system. This is seen in Fig. 2.1. The ECI frame has basis vectors

$$\mathcal{I} = (\hat{\boldsymbol{x}}, \hat{\boldsymbol{y}}, \hat{\boldsymbol{z}}).$$

2.1.2 LVLH - Local vertical, local horizontal frame

The local vertical, local horizontal (LVLH) frame is a rotating coordinate system, $\mathcal{L}$, with the $\hat{\boldsymbol{\rho}}$ unit vector pointing from the centre of the Earth to the chief satellite, $\hat{\boldsymbol{\xi}}$ pointing along the velocity of the chief satellite and $\hat{\boldsymbol{\eta}}$ pointing in the direction of the orbital angular momentum vector. Essentially, this is a frame rotating with the chief satellite, with the origin at the chief satellite's position. Together, this gives

$$\mathcal{L} = (\hat{\boldsymbol{\rho}}, \hat{\boldsymbol{\xi}}, \hat{\boldsymbol{\eta}}).$$

This frame is useful in that it allows us to calculate the relatively small separation between the spacecraft without encountering major numerical issues due to the large distances in the ECI frame. A visual representation of the coordinate system is shown in Fig. 2.1.

Converting between the ECI and LVLH frames is simple. Let the position of the chief spacecraft in ECI be $\boldsymbol{r}_c$ and the velocity be $\boldsymbol{v}_c$. The unit vectors of the new frame are hence

$$\hat{\boldsymbol{\rho}} = \frac{\boldsymbol{r}_c}{|\boldsymbol{r}_c|} \qquad \hat{\boldsymbol{\xi}} = \frac{\boldsymbol{v}_c}{|\boldsymbol{v}_c|} \qquad \hat{\boldsymbol{\eta}} = \hat{\boldsymbol{\rho}} \times \hat{\boldsymbol{\xi}}. \tag{2.1}$$

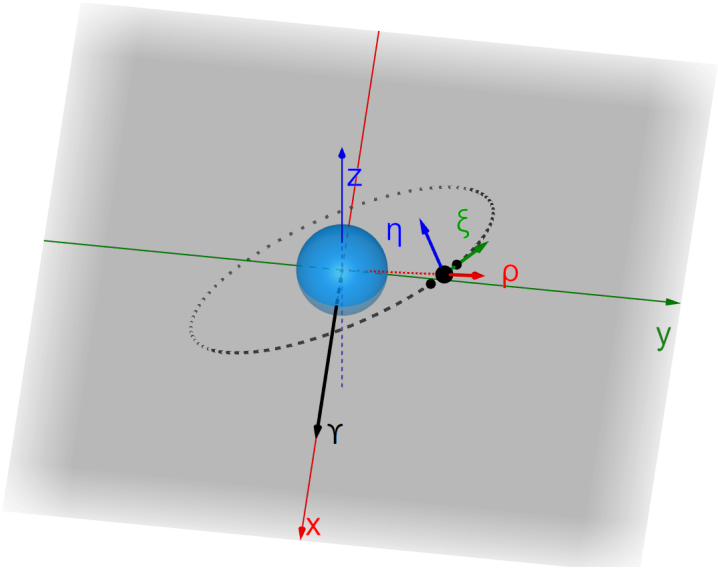

Figure 2.1: Schematic of the Earth-centred inertial (ECI) and the local vertical, local horizontal (LVLH) coordinate systems.

We define the change of basis matrix as

$$\boldsymbol{M}_{\mathcal{I}\to\mathcal{L}} = [\hat{\boldsymbol{\rho}}, \hat{\boldsymbol{\xi}}, \hat{\boldsymbol{\eta}}]^T. \tag{2.2}$$

Then the position of an ECI vector $\boldsymbol{r}_\mathcal{I}$ in the LVLH frame is

$$\boldsymbol{r}_\mathcal{L} = \boldsymbol{M}_{\mathcal{I}\to\mathcal{L}}\boldsymbol{r}_\mathcal{I} - \boldsymbol{M}_{\mathcal{I}\to\mathcal{L}}\boldsymbol{r}_c \tag{2.3}$$

and the velocity of an ECI vector $\boldsymbol{v}_\mathcal{I}$ is

$$\boldsymbol{v}_\mathcal{L} = \boldsymbol{M}_{\mathcal{I}\to\mathcal{L}}\boldsymbol{v}_\mathcal{I} - \boldsymbol{\omega} \times \boldsymbol{M}_{\mathcal{I}\to\mathcal{L}}\boldsymbol{r}_\mathcal{I}, \tag{2.4}$$

where $\boldsymbol{\omega}_\mathcal{L}$ is the angular velocity vector in the LVLH frame, given by

$$\boldsymbol{\omega}_\mathcal{L} = [0, 0, \omega_c] = \left[0, 0, \left|\frac{\boldsymbol{r}_c \times \boldsymbol{v}_c}{r_c^2}\right|\right]. \tag{2.5}$$

Directional vectors, such as $\hat{\boldsymbol{s}}$, can be rotated into the new frame through multiplication with the change of basis matrix $\boldsymbol{M}_{\mathcal{I}\to\mathcal{L}}$.

2.1.3 Curvilinear LVLH frame

The curvilinear LVLH frame, $\mathcal{C}$, is almost identical to the LVLH frame, with the exception that the $\hat{\boldsymbol{\xi}}$ and $\hat{\boldsymbol{\eta}}$ vectors curve around the Earth as lines of latitude and longitude rather than being tangential to the surface of the Earth. The conversion is a fairly straightforward geometrical mapping to a sphere. This is shown in Fig. 2.2.

Consider a satellite with position $\boldsymbol{r}_\mathcal{L} = [\rho_\mathcal{L}, \xi_\mathcal{L}, \eta_\mathcal{L}]$ and velocity $\boldsymbol{v}_\mathcal{L} = [\dot{\rho}_\mathcal{L}, \dot{\xi}_\mathcal{L}, \dot{\eta}_\mathcal{L}]$ in the LVLH frame. The subscript $\mathcal{L}$ denotes the linear frame. The radial position of this satellite with respect to the centre of the Earth is then

$$\boldsymbol{r}_\oplus = [R_\text{orb}, 0, 0] + \boldsymbol{r}_\mathcal{L}, \tag{2.6}$$

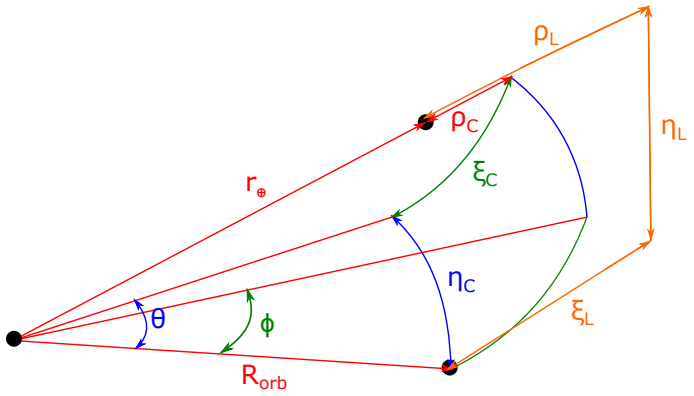

Figure 2.2: Comparing the curvilinear and rectangular LVLH coordinate systems.

where R_{orb} is the radius of the chief orbit. The radial distance is hence $r_\oplus = |\boldsymbol{r}_\oplus|$. We define the azimuthal and polar angle respectively between the deputy and the origin of the LVLH frame as

$$\phi = \tan^{-1}\left(\frac{\xi_\mathcal{L}}{R_{\text{orb}} + \rho_\mathcal{L}}\right) \qquad \theta = \sin^{-1}\left(\frac{\eta_\mathcal{L}}{r_\oplus}\right). \tag{2.7}$$

The rate of change of the radial distance and these angles with respect to time can be found by differentiating these definitions:

$$\begin{aligned} \dot{r}_\oplus &= \frac{\boldsymbol{r}_\oplus \cdot \boldsymbol{v}_\mathcal{L}}{r_\oplus} \\ \dot{\phi} &= \frac{\dot{\xi}_\mathcal{L}(R_{\text{orb}} + \rho_\mathcal{L}) - \xi_\mathcal{L}\dot{\rho}_\mathcal{L}}{\xi_\mathcal{L}^2 + (R_{\text{orb}} + \rho_\mathcal{L})^2} \\ \dot{\theta} &= \frac{\dot{\eta}_\mathcal{L} r_\oplus - \eta_\mathcal{L}\dot{r}_\oplus}{r_\oplus\sqrt{r_\oplus^2 - \eta_\mathcal{L}^2}}, \end{aligned} \tag{2.8}$$

and so the position and velocity in the curvilinear frame is

$$\boldsymbol{r}_\mathcal{C} = [r_\oplus - R_{\text{orb}}, R_{\text{orb}}\phi, R_{\text{orb}}\theta] \qquad \boldsymbol{v}_\mathcal{C} = [\dot{r}_\oplus, R_{\text{orb}}\dot{\phi}, R_{\text{orb}}\dot{\theta}]. \tag{2.9}$$

The inverse relationships are:

$$\begin{aligned} r_\oplus &= R_{\text{orb}} + \rho_\mathcal{C} \\ \phi &= \frac{\xi_\mathcal{C}}{R_{\text{orb}}} & \theta &= \frac{\eta_\mathcal{C}}{R_{\text{orb}}} \\ \dot{\phi} &= \frac{\dot{\xi}_\mathcal{C}}{R_{\text{orb}}} & \dot{\theta} &= \frac{\dot{\eta}_\mathcal{C}}{R_{\text{orb}}}, \end{aligned} \tag{2.10}$$

giving the rectangular LVLH positions as

$$\begin{aligned} \rho_\mathcal{L} &= r_\oplus \cos(\phi)\cos(\theta) - R_{\text{orb}} \\ \xi_\mathcal{L} &= r_\oplus \sin(\phi)\cos(\theta) \\ \eta_\mathcal{L} &= r_\oplus \sin(\theta). \end{aligned} \tag{2.11}$$

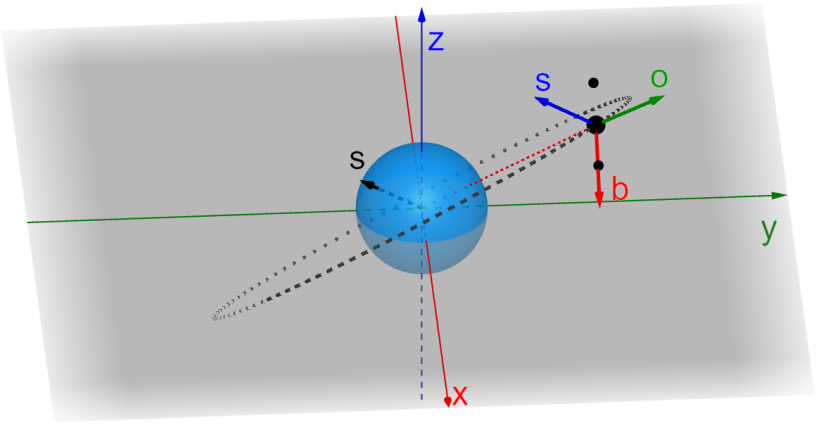

Figure 2.3: Schematic of the baseline coordinate system.

2.1.4 Baseline frame

The baseline frame, $\mathcal{B}$, is another critical frame, which is important for both the analysis of the orbit and the corrections of perturbations. This basis is centred on the chief satellite and has one axis along the baseline, one towards the star and a third orthogonal vector to complete the basis. In this frame, for an ideal, functioning interferometer, we expect the two spacecraft to have no positional component in the star direction and to only move back and forth along the baseline axis.

The frame is defined as follows: the baseline must be tangential to the surface of the Earth, as well as perpendicular to the star vector. To be tangential to the surface of the Earth, the vector must be orthogonal to the chief's position $\boldsymbol{r}_c$. Hence we define the baseline unit vector as

$$\hat{\boldsymbol{b}} = \frac{\boldsymbol{r}_c \times \hat{\boldsymbol{s}}}{|\boldsymbol{r}_c \times \hat{\boldsymbol{s}}|}. \tag{2.12}$$

To round out the basis, the third orthogonal vector is

$$\hat{\boldsymbol{o}} = \hat{\boldsymbol{s}} \times \hat{\boldsymbol{b}}. \tag{2.13}$$

Therefore

$$\mathcal{B} = (\hat{\boldsymbol{b}}, \hat{\boldsymbol{o}}, \hat{\boldsymbol{s}}).$$

A diagram of this frame is shown in Fig. 2.3.

Similarly to the LVLH frame, the baseline frame is centred on the chief spacecraft and is thus rotating. The formalism to change between the ECI frame and this frame is identical. We define the change of basis matrix as

$$\boldsymbol{M}_{\mathcal{I}\to\mathcal{B}} = [\hat{\boldsymbol{b}}, \hat{\boldsymbol{o}}, \hat{\boldsymbol{s}}]^T. \tag{2.14}$$

Then the position of an ECI vector $\boldsymbol{r}_{\mathcal{I}}$ in the LVLH frame is

$$\boldsymbol{r}_{\mathcal{B}} = \boldsymbol{M}_{\mathcal{I}\to\mathcal{B}}\boldsymbol{r}_{\mathcal{I}} - \boldsymbol{M}_{\mathcal{I}\to\mathcal{B}}\boldsymbol{r}_c \tag{2.15}$$

and the velocity of an ECI vector $\boldsymbol{v}_{\mathcal{I}}$ is

$$\boldsymbol{v}_{\mathcal{B}} = \boldsymbol{M}_{\mathcal{I}\to\mathcal{B}}\boldsymbol{v}_{\mathcal{I}} - \boldsymbol{\omega}_{\mathcal{B}} \times \boldsymbol{M}_{\mathcal{I}\to\mathcal{B}}\boldsymbol{r}_{\mathcal{I}}, \tag{2.16}$$

where $\boldsymbol{\omega}_{\mathcal{B}}$ is the angular velocity vector in the baseline frame. Since this frame is not aligned with the orbit, we must first calculate the angular velocity in the ECI frame and then rotate it:

$$\boldsymbol{\omega}_{\mathcal{B}} = \boldsymbol{M}_{\mathcal{I}\to\mathcal{B}}\frac{\boldsymbol{r}_c \times \boldsymbol{v}_c}{r_c^2}. \tag{2.17}$$

We can also transform to and from the LVLH frame in the following manner:

$$\boldsymbol{r}_{\mathcal{B}} = \boldsymbol{M}_{\mathcal{L}\to\mathcal{B}}\boldsymbol{r}_{\mathcal{L}} \qquad\qquad \boldsymbol{v}_{\mathcal{B}} = \boldsymbol{M}_{\mathcal{L}\to\mathcal{B}}\boldsymbol{v}_{\mathcal{L}}, \tag{2.18}$$

where

$$\boldsymbol{M}_{\mathcal{L}\to\mathcal{B}} = \boldsymbol{M}_{\mathcal{I}\to\mathcal{B}}\boldsymbol{M}_{\mathcal{I}\to\mathcal{L}}^{-1}. \tag{2.19}$$

2.2 LVLH orbit determination

Before beginning a more detailed analysis, we need to identify a configuration of this array that will allow for interferometry. Recall that we need to keep the optical path difference of the two deputy spacecraft to within at least 5 cm, where an optical delay line can then compensate the rest. The optical path difference is given by the equation

$$D = |\Delta\boldsymbol{r}_1| - \Delta\boldsymbol{r}_2 \cdot \hat{\boldsymbol{s}} - |\Delta\boldsymbol{r}_2| + \Delta\boldsymbol{r}_2 \cdot \hat{\boldsymbol{s}} \approx 0, \tag{2.20}$$

where $\Delta\boldsymbol{r}$ is the separation of one of the deputies from the chief, and $\hat{\boldsymbol{s}}$ is the unit vector in the direction of the star. In order to control this without large angular mirror actuation, we need an orbital configuration such that the two optical paths are perpendicular to the star vector at all times. That is, $\Delta\boldsymbol{r} \cdot \hat{\boldsymbol{s}} = 0$.

Consider a frame of reference of a circular orbit, where the plane of the orbit is in the $\hat{\boldsymbol{x}} - \hat{\boldsymbol{y}}$ plane. Then, consider a star vector in this frame with spherical coordinates (θ, ϕ), where θ is the polar angle and ϕ is the azimuthal angle from the $\hat{\boldsymbol{x}}$ axis. Finally, suppose that a satellite in this orbit has a phase ωt from the $\hat{\boldsymbol{x}}$ axis. Then, in the LVLH frame, we have that the star vector with respect to the satellite is

$$\hat{\boldsymbol{s}} = [\cos(\phi - \omega t)\sin(\theta), \sin(\phi - \omega t)\sin(\theta), \cos(\theta)]. \tag{2.21}$$

In 1960, Clohessy and Wiltshire developed a set of linear equations of motion describing the motion of a satellite with respect to another in the LVLH frame (hereby called the Hill-Clohessy-Wiltshire (HCW) equations) (Clohessy & Wiltshire, 2012). These equations are an approximation, with no treatment of perturbations and assumptions of

circular orbits. The HCW equations are given by

$$\begin{aligned} \ddot{\rho} &= 3\omega^2\rho + 2\omega\dot{\xi} \\ \ddot{\xi} &= -2\omega\dot{\rho} \qquad\qquad \omega = \sqrt{\frac{\mu}{R_{\text{orb}}^3}} \\ \ddot{\eta} &= -2\omega^2\eta, \end{aligned} \tag{2.22}$$

where ω is the angular velocity of the system, R_{orb} the radius of the chief's orbit and μ the standard gravitational parameter. These equations can be solved with initial conditions $\rho_0, \xi_0, \eta_0, \dot{\rho}_0, \dot{\xi}_0, \dot{\eta}_0$, yielding

$$\begin{aligned} \rho(t) &= 4\rho_0 + \frac{2\dot{\xi}_0}{\omega} - (3\rho_0 + \frac{2\dot{\xi}_0}{\omega})\cos(\omega t) + \frac{\dot{\rho}_0}{\omega}\sin(\omega t) \\ \xi(t) &= \xi_0 - \frac{2\dot{\rho}_0}{\omega} - 6\omega\rho_0 t - 3\dot{\xi}_0 t + \frac{2\dot{\rho}_0}{\omega}\cos(\omega t) + (6\rho_0 + \frac{4\dot{\xi}_0}{\omega})\sin(\omega t) \\ \eta(t) &= \eta_0\cos(\omega t) + \frac{\dot{\eta}_0}{\omega}\sin(\omega t). \end{aligned} \tag{2.23}$$

If we consider grouping with coefficients

$$\begin{aligned} \kappa_1 &= 4\rho_0 + \frac{2\dot{\xi}_0}{\omega} & \kappa_2 &= \xi_0 - \frac{2\dot{\rho}_0}{\omega} \\ \kappa_3 &= -(3\rho_0 + \frac{2\dot{\xi}_0}{\omega}) & \kappa_4 &= \frac{\dot{\xi}_0}{\omega} \\ \kappa_5 &= \eta_0 & \kappa_6 &= \frac{\dot{\eta}}{\omega} \end{aligned} \tag{2.24}$$

and then making the substitution

$$\kappa_3 = A_1\cos(\varphi_1) \qquad\qquad \kappa_4 = A_1\sin(\varphi_1), \tag{2.25}$$

we obtain $\Delta\boldsymbol{r}(t) = [\rho(t), \xi(t), \eta(t)]$, where

$$\rho(t) = \kappa_1 + A_1\cos(\omega t - \varphi_1) \tag{2.26}$$

$$\xi(t) = \kappa_2 - \frac{3\omega}{2}\kappa_1 t - 2A_1\sin(\omega t - \varphi_1) \tag{2.27}$$

$$\eta(t) = \kappa_5\cos(\omega t) + \kappa_6\sin(\omega t) \tag{2.28}$$

Now, we see immediately in Equation 2.27 that if $\kappa_1 \neq 0$, then the orbital angular momentum will change and the spacecraft will fly apart. Thus we set initial conditions such that $\kappa_1 = 0$ to remove this motion. Furthermore, suppose that the initial conditions are chosen such that A_1 is zero. Then the product $\Delta\boldsymbol{r}\cdot\hat{\boldsymbol{s}}$ (using equation 2.23) is

$$\begin{aligned} \Delta\boldsymbol{r}\cdot\hat{\boldsymbol{s}} =& \kappa_2(\cos(\omega t)\sin(\phi) - \sin(\omega t)\cos(\phi))\sin(\theta) \\ &+ \kappa_5\cos(\omega t)\cos(\theta) + \kappa_6\sin(\omega t)\cos(\theta). \end{aligned} \tag{2.29}$$

Finally, if we then set

$$\kappa_5 = -\kappa_2\tan(\theta)\sin(\phi) \qquad\qquad \kappa_6 = \kappa_2\tan(\theta)\cos(\phi), \tag{2.30}$$

we have that $\Delta\boldsymbol{r}\cdot\hat{\boldsymbol{s}} = 0$ for all t. Hence a simple linear array will work for this mission,

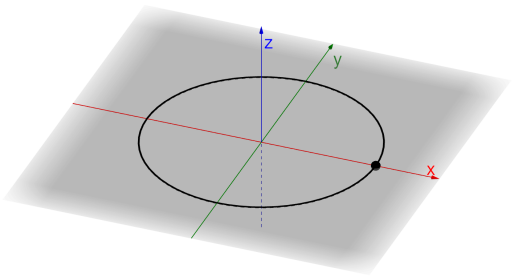

(a) Initial starting position

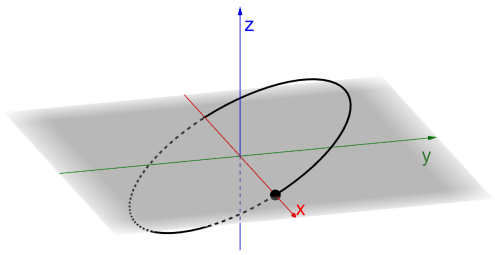

(b) Rotation in inclination about $\hat{\mathbf{x}}$ axis

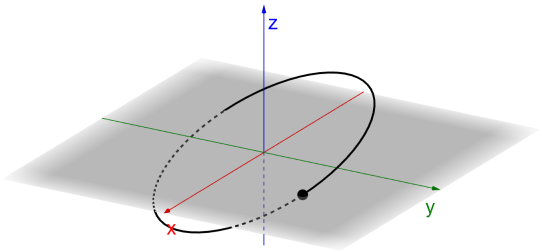

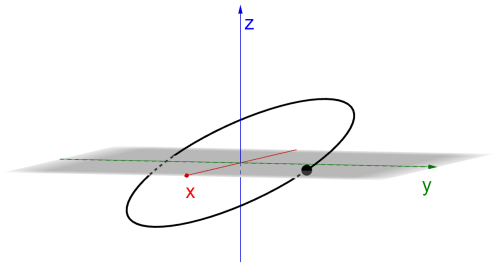

(c) Rotation in longitude about $\hat{\mathbf{z}}$ axis

Figure 2.4: Determining the orbit of the chief beam-combiner satellite

where the deputy satellites move up and down in the $\hat{\boldsymbol{\eta}}$ direction with a period equal to that of the orbital period, with an offset in the $\hat{\boldsymbol{\xi}}$ direction. In terms of orbits, this means that a configuration where the deputies are in orbits identical to the chief, albeit with a small phase and inclination offset, will suffice in keeping the array perpendicular to the star at all times.

2.3 ECI orbit determination

We will now describe how to implement the orbit of the chief satellite in the ECI frame, as well as define rotations that will take the chief orbit and determine the deputy satellite orbits in a manner such that they are perpendicular to the star. This section makes heavy use of quaternions (conventional in spacecraft engineering), a treatment of which can be found in Appendix A.1.

2.3.1 Defining the chief orbit

To define the orbit of the chief satellite, we begin with a circular orbit in the $\hat{\boldsymbol{x}} - \hat{\boldsymbol{y}}$ plane, with radius R_{orb}. R_{orb} can be decomposed into an altitude Z and the Earth's radius R_E, such that $R_{\text{orb}} = Z + R_E$. The satellite starts with a phase (φ) of zero on the positive $\hat{\boldsymbol{x}}$ axis, shown in Fig. 2.4a.

The orientation of a circular orbit is given by 2 parameters: the inclination i_c and the longitude of the ascending node Ω_c. We first rotate in the inclination i_c about the $\hat{\boldsymbol{x}}$ axis;

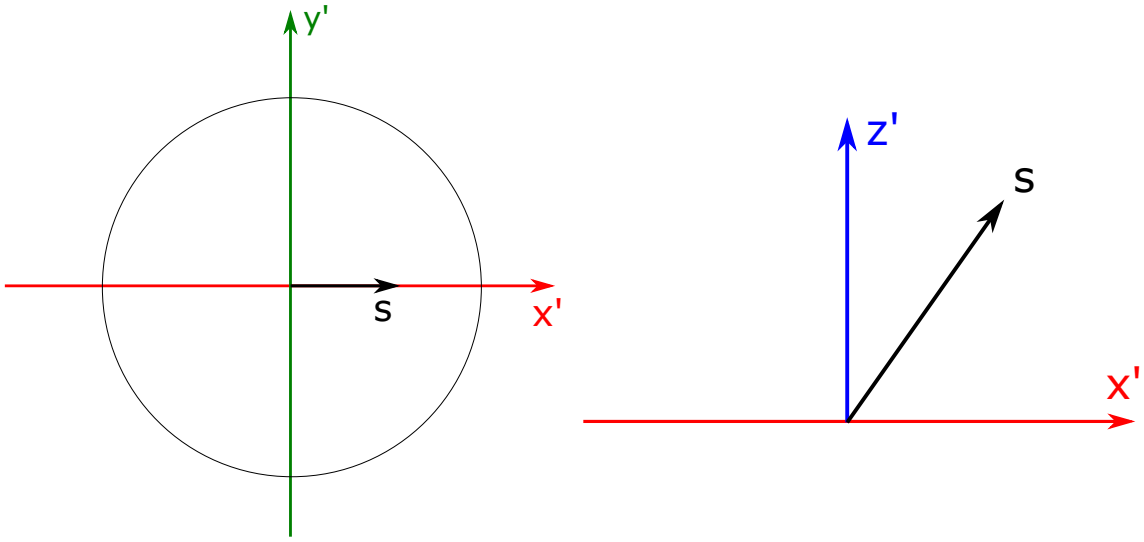

Figure 2.5: Defining the coordinate system for use in orbit determination.

in quaternion form (Fig. 2.4b):

$$\boldsymbol{q}(\hat{\boldsymbol{x}}, i_c).$$

We then rotate in the longitude of the ascending node around the $\hat{\boldsymbol{z}}$ axis (Fig. 2.4c):

$$\boldsymbol{q}(\hat{\boldsymbol{z}}, \Omega_c).$$

This gives us that the satellite, at $t = 0$, has an argument of latitude $\theta = 0$. In other words, the chief satellite crosses the equator at $t = 0$. The full rotation can be combined to give

$$\boldsymbol{q}_c = \boldsymbol{q}(\hat{\boldsymbol{z}}, \Omega_c)\boldsymbol{q}(\hat{\boldsymbol{x}}, i_c).$$

The rotation can be applied to a vector $\boldsymbol{u}$ using

$$\boldsymbol{Q}(\boldsymbol{u}, \boldsymbol{q}_c) = (\boldsymbol{q}_c)\boldsymbol{p}(\boldsymbol{q}_c^{-1}), \tag{2.31}$$

where $\boldsymbol{p} = u_x\boldsymbol{i} + u_y\boldsymbol{j} + u_z\boldsymbol{k}$.

2.3.2 Determining the deputy orbits

Our task is now to identify the rotations that will give us the deputy orbits from the chief orbit. First, we define a star vector $\hat{\boldsymbol{s}}$, which is in the direction of the star to be observed. This can be composed through a simple conversion from right ascension (α) and declination (δ):

$$\hat{\boldsymbol{s}} = [\cos(\alpha)\cos(\delta), \sin(\alpha)\cos(\delta), \sin(\delta)]. \tag{2.32}$$

In the absence of perturbations, we assume that the separation between each of the deputies and the chief spacecraft is equal, and we denote this separation $\Delta\boldsymbol{r}$. Furthermore, recall we require that $\Delta\boldsymbol{r} \cdot \hat{\boldsymbol{s}} = 0$ for all φ.

We now define a new coordinate system, shown in Fig. 2.5, based on the orbital plane of the chief satellite: $\hat{\boldsymbol{z'}}$ is in the direction of the angular momentum of the orbit, $\hat{\boldsymbol{x'}}$ is the unit projection of the star vector on the orbital plane, and $\hat{\boldsymbol{y'}}$ is the remaining orthogonal

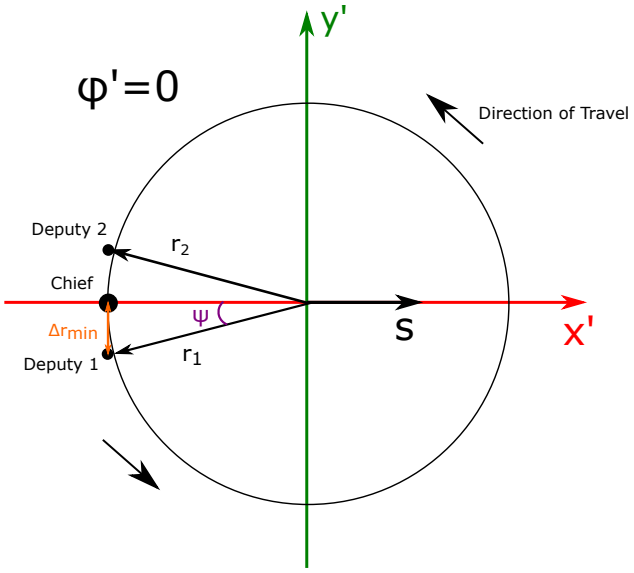

Figure 2.6: Satellite positions at $\varphi' = 0$

vector. Mathematically:

$$\begin{aligned}
\hat{\boldsymbol{z}}' &= \hat{\boldsymbol{h}} = \boldsymbol{Q}(\hat{\boldsymbol{z}}, \boldsymbol{q}_c) = [\sin(i_c)\cos(\Omega_c), \sin(i_c)\sin(\Omega_c), \cos(i_c)] \\
\hat{\boldsymbol{x}}' &= \frac{\hat{\boldsymbol{s}} - \hat{\boldsymbol{z}}'(\hat{\boldsymbol{s}} \cdot \hat{\boldsymbol{z}}')}{|\hat{\boldsymbol{s}} - \hat{\boldsymbol{z}}'(\hat{\boldsymbol{s}} \cdot \hat{\boldsymbol{z}}')|} \\
\hat{\boldsymbol{y}}' &= \hat{\boldsymbol{z}}' \times \hat{\boldsymbol{x}}'.
\end{aligned} \tag{2.33}$$

We let the deputy spacecraft be aligned with the chief spacecraft along the $\hat{\boldsymbol{y}}'$ direction at the new phase $\varphi' = 0$, located on the negative $\hat{\boldsymbol{x}}'$ axis. The separation between the first deputy and the chief at this point is a minimum, defined at this stage to be $\Delta\boldsymbol{r}_{\min}$. If the star vector is in the plane of the orbit, then it is possible that the satellites will have to "pass through each other" and thus the separation will be zero. This separation will need to be redefined later in terms of the maximum separation of the spacecraft to account for this. Nevertheless, for the moment this configuration has an angular separation defined as $\psi = \frac{|\Delta\boldsymbol{r}_{\min}|}{R_{\text{orb}}}$ ($|\Delta\boldsymbol{r}_{\min}| << R_{\text{orb}}$). The other deputy is identical, replacing ψ with $-\psi$. The initial configuration is shown schematically in Fig. 2.6. The position vectors (at $\varphi' = 0$) are hence

$$\begin{aligned}
\boldsymbol{r}_1 &= -\cos(\psi)\hat{\boldsymbol{x}}' - \sin(\psi)\hat{\boldsymbol{y}}' \\
\boldsymbol{r}_2 &= -\cos(\psi)\hat{\boldsymbol{x}}' + \sin(\psi)\hat{\boldsymbol{y}}'.
\end{aligned} \tag{2.34}$$

Since the orbits of the deputy satellites must pass through these points and are circular orbits with a known radius, the orbits are constrained to only one degree of freedom: a rotation about the position vectors described above with respect to the chief orbit.

To identify the angle of rotation, β, we turn to the position of the three satellites at $\varphi' = \frac{\pi}{2}$, the maximum or minimum of the orbit in the $\hat{\boldsymbol{z}}'$ direction and also the point of maximum separation $\Delta\boldsymbol{r} = \Delta\boldsymbol{r}_{\max}$. This is shown in Fig. 2.7. Here, we define θ to be the angle between the star vector $\hat{\boldsymbol{s}}$ and the $\hat{\boldsymbol{z}}'$ axis. That is,

$$\theta = \cos^{-1}(\hat{\boldsymbol{s}} \cdot \hat{\boldsymbol{z}}'). \tag{2.35}$$

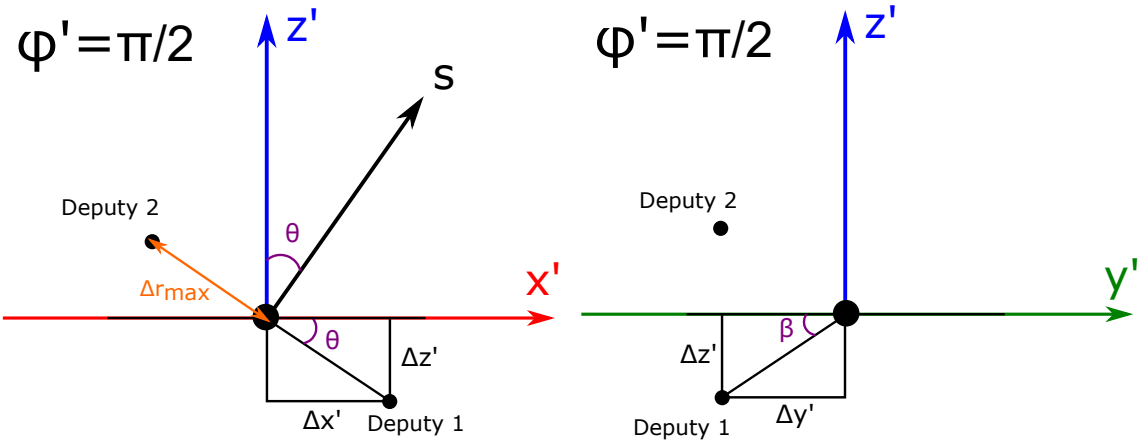

Figure 2.7: Satellite positions at $\varphi' = \pi/2$.

Focusing in on the first deputy satellite (with positive ψ), we can see that at $\varphi' = \frac{\pi}{2}$, it is at a minimum in the $\hat{z}$ direction. Hence, the angle that the satellite makes with the chief orbital plane at this point is the angle of rotation β. From this diagram, we can uncover a few relations:

$$\Delta y' = -R_{\text{orb}} \cos\beta \tag{2.36}$$
$$\Delta z' = -R_{\text{orb}} \sin\beta. \tag{2.37}$$

Now, we know that the angular separation on the orbital plane between the chief and first deputy spacecraft is ψ. Since $|\Delta \boldsymbol{r}_{\text{min}}| << R_{\text{orb}}$, using the small angle approximation we have

$$\begin{aligned}\Delta x' &= \psi |\Delta y'| \\ &= |\Delta \boldsymbol{r}_{\text{min}}| \cos\beta.\end{aligned} \tag{2.38}$$

Finally, we can relate this to the angle between the star vector and $\hat{\boldsymbol{z}}'$ axis, θ:

$$\tan\theta = \frac{\Delta z'}{\Delta x'} = \frac{-R_{\text{orb}} \sin\beta}{|\Delta \boldsymbol{r}_{\text{min}}| \cos\beta}$$
$$\psi \tan\theta = -\tan\beta. \tag{2.39}$$

Furthermore, since $\Delta y' >> \Delta z'$, we can apply the small angle approximation:

$$\beta = -\psi \tan\theta. \tag{2.40}$$

Before we continue, recall that we needed to redefine $|\Delta \boldsymbol{r}_{\text{min}}|$ in terms of the maximum separation,as the minimum needs to be allowed to reach zero when the star is in the orbital plane. Note that

$$\begin{aligned}|\Delta \boldsymbol{r}_{\text{max}}| &= \sqrt{\Delta x'^2 + \Delta z'^2} \\ &= \sqrt{(\psi R_{\text{orb}} \cos\beta)^2 + (R_{\text{orb}} \sin\beta)^2}.\end{aligned} \tag{2.41}$$

Since β is small,

$$\begin{aligned} |\Delta \boldsymbol{r}_{\text{max}}| &\approx R_{\text{orb}} \sqrt{\psi^2 + \beta^2} \\ &= R_{\text{orb}} \psi \sqrt{1 + \tan^2 \theta} \\ \Rightarrow |\Delta \boldsymbol{r}_{\text{min}}| &= |\Delta \boldsymbol{r}_{\text{max}}| \cos \theta. \end{aligned} \tag{2.42}$$

Hence our definition of ψ becomes

$$\psi = \frac{|\Delta \boldsymbol{r}_{\text{max}}| \cos \theta}{R_{\text{orb}}}, \tag{2.43}$$

and the angle of rotation β becomes

$$\begin{aligned} \beta &= -\psi \tan \theta \\ &= -\frac{|\Delta \boldsymbol{r}_{\text{max}}| \sin \theta}{R_{\text{orb}}}. \end{aligned} \tag{2.44}$$

For the other satellite, it should rotate by $-\beta$. Checking the limits shows this works: if the star is straight up ($\theta = 0°$), the orbit would not have to tilt for the star to remain perpendicular. If the star is parallel to the plane of the orbit ($\theta = 90°$), then the minimum separation $|\Delta \boldsymbol{r}_{\text{min}}|$ becomes zero as is required. The orbit will still rotate by β - this simply means that the stars will always be in a vertical line along the direction of the $\hat{\boldsymbol{z}}'$ axis.

So, writing the orbital plane rotations in quaternion form:

$$\begin{aligned} \boldsymbol{q}_{1,\text{plane}} &= \boldsymbol{q}\left(\boldsymbol{r}_1, \beta\right) \\ \boldsymbol{q}_{2,\text{plane}} &= \boldsymbol{q}\left(\boldsymbol{r}_2, -\beta\right). \end{aligned} \tag{2.45}$$

Before the orbital plane is rotated, the phase should be adjusted for each of the deputy satellites such that they start in the positions defined at $\varphi' = 0$. This is a simple rotation about the $\hat{\boldsymbol{z}}'$ axis by ψ in the counterclockwise direction for $\boldsymbol{r}_1$ and clockwise for $\boldsymbol{r}_2$:

$$\begin{aligned} \boldsymbol{q}_{1,\text{phase}} &= \boldsymbol{q}(\hat{\boldsymbol{z}}', \psi) \\ \boldsymbol{q}_{2,\text{phase}} &= \boldsymbol{q}(\hat{\boldsymbol{z}}', -\psi). \end{aligned} \tag{2.46}$$

Combining the two gives the full rotation quaternions for the two deputy orbits, starting from the chief orbit:

$$\begin{aligned} \boldsymbol{q}_1 = \boldsymbol{q}_{1,\text{plane}} \boldsymbol{q}_{1,\text{phase}} &= \boldsymbol{q}(\boldsymbol{r}_1, \beta) \boldsymbol{q}(\hat{\boldsymbol{z}}', \psi) \\ \boldsymbol{q}_2 = \boldsymbol{q}_{2,\text{plane}} \boldsymbol{q}_{2,\text{phase}} &= \boldsymbol{q}(\boldsymbol{r}_2, -\beta) \boldsymbol{q}(\hat{\boldsymbol{z}}', -\psi), \end{aligned} \tag{2.47}$$

and rotation functions for an arbitrary vector along the chief orbit $\boldsymbol{u}' = \boldsymbol{Q}(\boldsymbol{u}, \boldsymbol{q}_c)$:

$$\begin{aligned} \boldsymbol{Q}(\boldsymbol{u}', \boldsymbol{q}_1) &= \boldsymbol{q}_1 \boldsymbol{p} \boldsymbol{q}_1^{-1} \\ \boldsymbol{Q}(\boldsymbol{u}', \boldsymbol{q}_2) &= \boldsymbol{q}_2 \boldsymbol{p} \boldsymbol{q}_2^{-1}, \end{aligned} \tag{2.48}$$

where, to recall:

$$\boldsymbol{p} = u_x' \boldsymbol{i} + u_y' \boldsymbol{j} + u_z' \boldsymbol{k}. \tag{2.49}$$

Chapter 3

Orbital Perturbations

While it would be ideal to analytically investigate the theoretical orbits discussed in the previous chapter, the spacecraft array will experience perturbations to its orbit due to a variety of effects. As we are interested in the behaviour of the array during the orbit, and whether the configuration is stable enough to perform interferometry, these pertubations are critical considerations. Among these perturbations are drag due to the atmosphere, gravitational perturbations due to the Moon and Sun, solar radiation pressure and, most importantly, the non-spherical nature of the Earth's gravitational field.

A schematic of the magnitude of different perturbations at different altitudes is shown in Fig. 3.1 from Montenbruck & Gill (2000). Here it is very apparent that at an altitude of 500 km (a radial distance from the centre of the Earth of 6.8 Mm) that the J_2 gravitational term is the dominating perturbation bar the spherical potential, followed by atmospheric drag contributing a couple of orders of magnitude fewer. For this reason, our simulations will only properly treat the non-sphericity of the Earth's gravitational field, followed by an order of magnitude calculation for drag. In more detailed control simulations, other perturbation effects will need to be considered, but from a feasibility standpoint this should suffice.

From here on, if not explicitly stated, we will be assuming that the altitude of the array is 500 km and the maximum separation between a chief and deputy spacecraft is $|\Delta \boldsymbol{r}_{\max}| = 300\,\mathrm{m}$.

3.1 Non-perturbed motion

Before introducing perturbations, we first should briefly look at the non-perturbed motion of the system. Recall the Hill-Clohessy-Wiltshire (HCW) equations of motion - a set of linear differential equations for calculating the motion of a satellite in the local vertical, local horizontal (LVLH) frame (Clohessy & Wiltshire, 2012):

$$\begin{aligned} \ddot{\rho} &= 3\omega^2\rho + 2\omega\dot{\xi} \\ \ddot{\xi} &= -2\omega\dot{\rho} \qquad\qquad \omega = \sqrt{\frac{\mu}{R_{\mathrm{orb}}^3}} \\ \ddot{\eta} &= -2\omega^2\eta, \end{aligned} \tag{3.1}$$

where ω is the angular velocity of the system, R_{orb} the radius of the chief's orbit and μ the standard gravitational parameter. The advantage of calculating the motion in the LVLH frame is that the distances are on the order of hundreds of metres, rather than the thousands of kilometres in the Earth-centred inertial (ECI) frame. As we want to identify

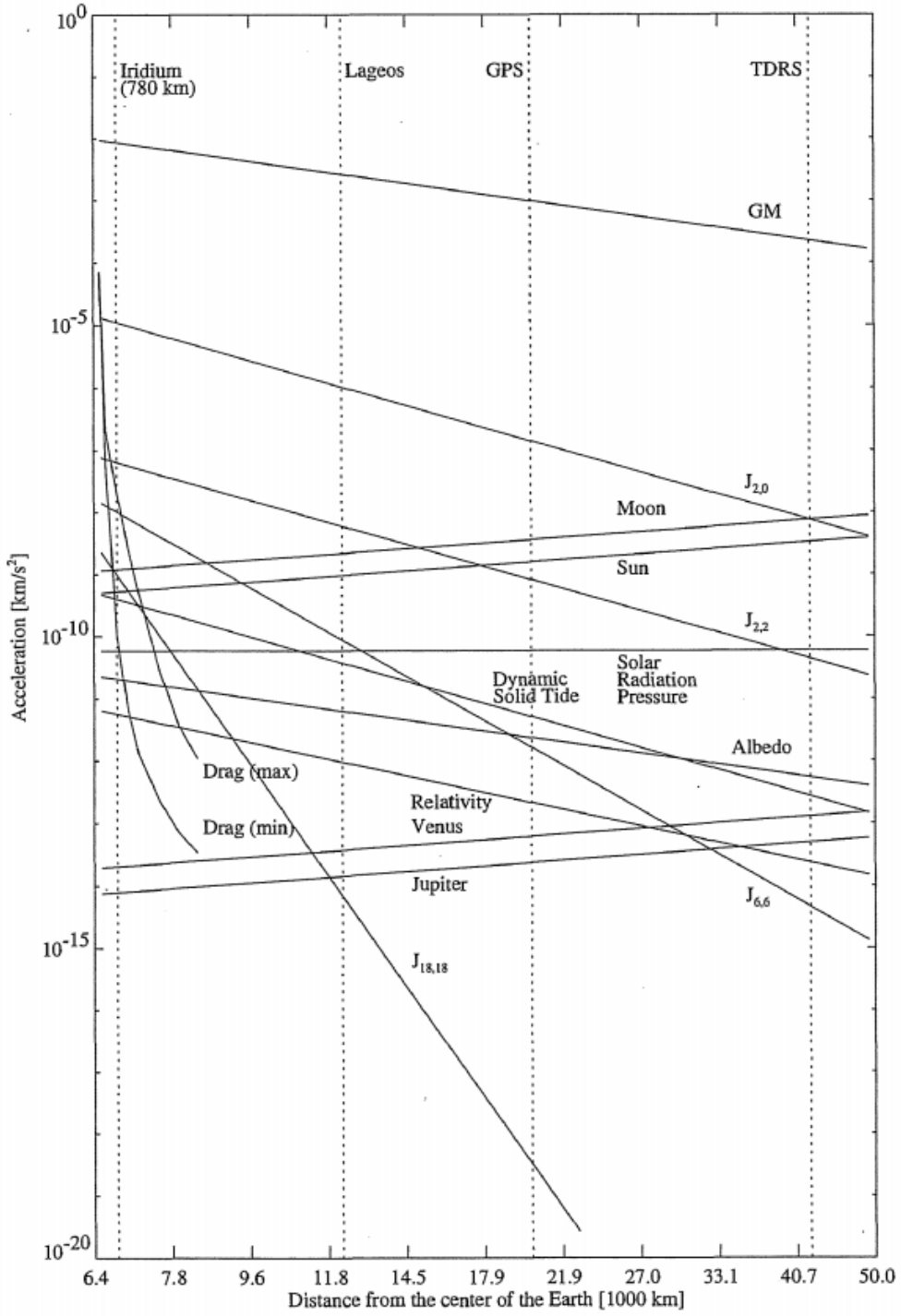

Figure 3.1: Order of magnitude plot for various perturbations acting on satellites at given altitudes. GM refers to the standard gravitational spherical potential, and radiation pressure assumes an area to mass ratio of $0.01\,\mathrm{m}^2/\mathrm{kg}$. Vertical dashed lines represent satellites at various altitudes above the Earth's surface. Plot from Montenbruck & Gill (2000).

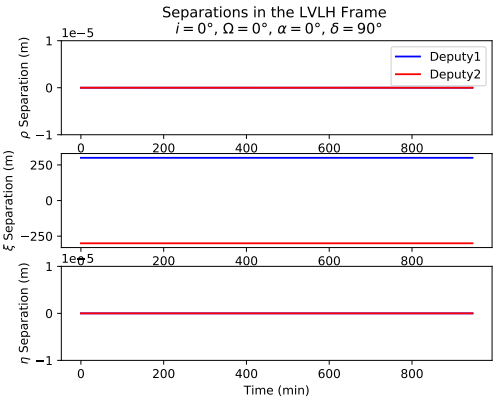

(a) $i = 0°,\ \Omega = 0°,\ \alpha = 0°,\ \delta = 90°$

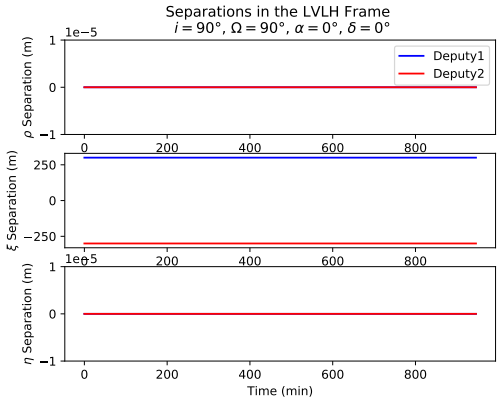

(b) $i = 90°,\ \Omega = 90°,\ \alpha = 0°,\ \delta = 0°$

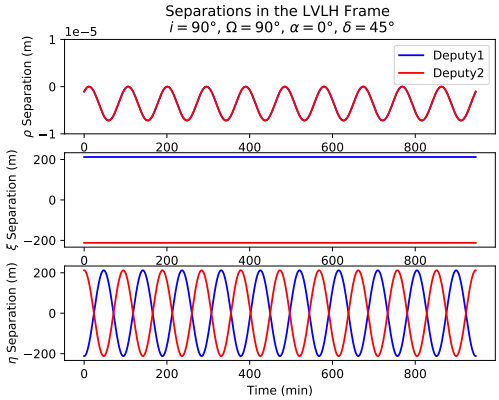

(c) $i = 90°,\ \Omega = 90°,\ \alpha = 0°,\ \delta = 45°$

Figure 3.2: Non-perturbed motion of the two deputy spacecraft with respect to the chief. Plotted over 10 orbits in the curvilinear LVLH frame using the HCW equations for different orbital configurations.

small separations less than a centimetre, this is ideal to avoid numerical errors.

Integrating these equations of motion allows us to see how the array moves through the LVLH frame. To improve accuracy, the curvilinear variant of the LVLH frame was used (see Section 2.1.3). The motion of the two deputies with respect to the chief for three different orbits is shown in Fig. 3.2. Numerical errors due to conversion between the ECI and curvilinear frames were identified up to a level of 10 μm, and so the y axis was prevented from zooming in further than this scale.

We see that in the absence of perturbations, an equatorial orbit (Fig. 3.2a) and a polar orbit (Fig. 3.2b) where the star is perpendicular to the orbital plane (that is, the satellites are following each other in-track) are identical up to numerical errors. The in-track separation ($\Delta\xi$) remains constant over the orbit, and the other separations are zero. For a polar orbit, but with the star at 45° from the orbital plane (Fig. 3.2c), we see that the cross-track motion ($\Delta\eta$) is oscillatory. As explained in Section 2.2, this is due to the satellites moving up and down to stay perpendicular to the star at all points in the orbit. Overall, the motion is stable.

3.2 The J2 perturbation

3.2.1 The geopotential model

For a more complete treatment of these gravitational perturbations, see Appendix A.2.

The Earth's gravitational potential can be expanded in spherical harmonics:

$$U = -\frac{\mu}{r}\left[1 + \sum_{n=2}^{\infty} J_n \left(\frac{R_E}{r}\right)^n P_n^0(\cos\theta) + \sum_{n=2}^{\infty}\sum_{m=0}^{n} \left(\frac{R_E}{r}\right)^n P_n^m(\cos\theta)[C_n^m \cos m\varphi + S_n^m \sin m\varphi]\right]. \tag{3.2}$$

The first few coefficients are listed in Appendix A.2. The J_2 zonal term is the most important by several orders of magnitude, being the Earth's oblateness term, and so truncating the series at this point yields

$$\begin{aligned} U &= -\frac{\mu}{r}\left[1 + J_2 \left(\frac{R_E}{r}\right)^2 P_2^0(\cos\theta)\right] \\ &= -\frac{\mu}{r}\left[1 + J_2 \frac{R_E^2}{2r^2}(3\cos^2\theta - 1)\right], \end{aligned} \tag{3.3}$$

where J_2 is the zonal coefficient, approximately 0.00108. Being a zonal term, we note that J_2 does not change with longitude and is dependent on latitude. The J_2 term of the potential is

$$U_{J_2} = -J_2 \frac{\mu R_E^2}{2r^3}(3\cos^2\theta - 1). \tag{3.4}$$

Expanding back into ECI coordinates and taking the negative gradient gives the force from J_2:

$$\boldsymbol{F}_{J_2} = J_2 \frac{3\mu R_E^2}{2r^5}\left[\left(1 - 5\frac{z^2}{r^2}\right)(x\hat{\boldsymbol{x}} + y\hat{\boldsymbol{y}}) + \left(3 - 5\frac{z^2}{r^2}\right) z\hat{\boldsymbol{z}}\right], \tag{3.5}$$

and so the complete equation of motion in the ECI frame is

$$\ddot{\boldsymbol{r}}_{J_2} = -\frac{\mu}{r^2}\hat{\boldsymbol{r}} + J_2 \frac{3\mu R_E^2}{2r^5}\left[\left(1 - 5\frac{z^2}{r^2}\right)(x\hat{\boldsymbol{x}} + y\hat{\boldsymbol{y}}) + \left(3 - 5\frac{z^2}{r^2}\right) z\hat{\boldsymbol{z}}\right]. \tag{3.6}$$

3.2.2 J2 in the LVLH frame

Calculating the J_2 perturbation would require we integrate the ECI equations of motion (Equation 3.6). Unfortunately, here we are presented with an issue - in the ECI frame, the positions are of the order of thousands of kilometres. As before, it is thus ideal to try and integrate the equations of motion in the LVLH frame.

The simplest approach in developing this equation of motion was conducted by Schweighart & Sedwick (2002). This approach involved linearising the ECI equation of motion in the LVLH frame. A "reference orbit" was also introduced, defined as a circular orbit with a period adjusted for the J_2 perturbation. The equations detail the position and velocity of a satellite in the LVLH frame with respect to the reference orbit position,

rather than the chief satellite. Hence, to find the separation between the chief and deputy spacecraft, the difference between the relative positions of the chief and deputy with respect to the reference orbit must be calculated. A more detailed derivation of the equations described below are found in Appendix A.3.

In the absence of perturbations, the reference orbit is rotating with an angular velocity given by

$$\begin{aligned} \boldsymbol{\omega} &= \omega \hat{\boldsymbol{\eta}} \\ \omega &= \sqrt{\frac{\mu}{R_{\text{orb}}^3}}. \end{aligned} \tag{3.7}$$

Through averaging the angular velocity over the J_2 perturbation, the reference orbit must be adjusted by a factor c, where

$$\begin{aligned} c &= \sqrt{1 + \frac{3J_2R_E^2}{8R_{\text{orb}}^2}(1 + 3\cos(2i))} \\ \implies \boldsymbol{\omega} &= \omega c \hat{\boldsymbol{\eta}}. \end{aligned} \tag{3.8}$$

The main long term effect of J_2 is nodal precession, where the longitude of the ascending node Ω drifts over time. Hence we must correct this through adjusting the reference orbit. The position of the reference orbit at a time t in the ECI frame is then given by

$$\begin{aligned} \boldsymbol{r}_{\text{ref}} = R_{\text{orb}}([&\cos\Omega(t)\cos\theta(t) - \sin\Omega(t)\sin\theta(t)\cos i(t)]\hat{\boldsymbol{x}} \\ +[&\sin\Omega(t)\cos\theta(t) - \cos\Omega(t)\sin\theta(t)\cos i(t)]\hat{\boldsymbol{y}} \\ +[&\sin\theta(t)\sin i(t)]\hat{\boldsymbol{z}}), \end{aligned} \tag{3.9}$$

where

$$\begin{aligned} i(t) &= i_{\text{ref}} - \frac{\sigma}{k}\sin i_{\text{ref}} & \sigma &= \left(\frac{3\omega J_2 R_E^2}{2R_{\text{orb}}^2}\right)\cos i_{\text{ref}} \\ \Omega(t) &= \Omega_0 - \sigma t & k &= \omega c + \sigma\cos i_{\text{ref}} \\ \theta(t) &= kt. \end{aligned} \tag{3.10}$$

One last correction was also applied: correcting the cross-track motion of the satellites (η). This correction is made due to the averaging of the J_2 gradient, which causes errors in the period of the cross-track motion (Schweighart & Sedwick, 2002), and so correcting this results in the differential equation

$$\ddot{\eta} = -q^2\eta + 2lq\cos(qt + \phi), \tag{3.11}$$

where q, l and ϕ are constants defined in Appendix A.3. Putting it all together gives us

the final set of three coupled differential equations:

$$\begin{aligned}
\ddot{\rho} &= 2\omega c\dot{\xi} + (5c^2 - 2)\omega^2\rho - 3\omega^2 J_2 \frac{R_E^2}{R_{\text{orb}}} \frac{3\cos 2kt \sin^2 i_{\text{ref}}}{4} \\
\ddot{\xi} &= -2\omega c\dot{\rho} - 3\omega^2 J_2 \frac{R_E^2}{R_{\text{orb}}} \sin^2 i_{\text{ref}} \sin kt \cos kt \\
\ddot{\eta} &= -q^2\eta + 2lq\cos(qt + \phi).
\end{aligned} \tag{3.12}$$

The given solutions by Schweighart & Sedwick (2002) assume certain initial conditions for $t = 0$. To generalise the equations, a set of solutions for arbitrary initial conditions at $t = t_0$ were created, requiring the following coefficients:

$$\begin{aligned}
\kappa_1 &= \beta^2\rho_0 + \frac{\beta}{\alpha}\dot{\xi}_0 - \beta\zeta(\delta^2 - 4)\cos(2kt_0) \\
\kappa_2 &= \xi_0 - \frac{\beta}{\alpha}\dot{\rho_0} + \frac{1}{2}\zeta(\delta^2 - 4)(\gamma\delta - 3\beta)\sin(2kt_0) \\
\kappa_3 &= -\gamma\rho_0 - \frac{\beta}{\alpha}\dot{\xi}_0 - \zeta(4\beta - 3\delta)\cos(2kt_0) \\
\kappa_4 &= \frac{1}{\alpha}\dot{\rho_0} + 2\zeta(\beta\delta - 3)\sin(2kt_0) \\
\kappa_5 &= \zeta(\beta\delta^2 - 3\delta) \\
\kappa_6 &= \frac{\zeta\delta}{2}(3\beta\delta - \gamma\delta^2 - 4) \\
\kappa_7 &= \eta_0 \\
\kappa_8 &= \frac{\dot{\eta_0} - l\sin(qt_0 + \phi)}{q},
\end{aligned} \tag{3.13}$$

where $\alpha, \beta, \gamma, \delta$ and ζ are constants also defined in Appendix A.3. With the substitution

$$\begin{aligned}
\kappa_3 &= A_1\cos\varphi_1 & \kappa_4 &= A_1\sin\varphi_1 \\
\kappa_7 &= A_2\cos\varphi_2 & \kappa_8 &= A_2\sin\varphi_2,
\end{aligned} \tag{3.14}$$

the final equations for the position of a satellite at a time t, with initial conditions at a time $t = t_0$ are then

$$\begin{aligned}
\rho(t) &= \kappa_1 + A_1\cos(\alpha(t - t_0) - \varphi_1) + \kappa_5\cos(2kt) \\
\xi(t) &= \kappa_2 - \frac{\alpha\gamma}{\beta}\kappa_1(t - t_0) - \beta A_1\sin(\alpha(t - t_0) - \varphi_1) + \kappa_6\sin(2kt) \\
\eta(t) &= A_2\cos(q(t - t_0) - \varphi_2) + l(t - t_0)\sin(qt + \phi).
\end{aligned} \tag{3.15}$$

It should be noted that when the initial conditions of Schweighart & Sedwick (2002) are given, these equations reduce to those in the paper. Furthermore, setting the J_2 parameter to zero reduces the equations to the HCW equations listed in Section 3.1. An extended demonstration of this is found in Appendix A.3.

A diagram showing the deputy satellite positions with respect to the circular reference orbit under the effect of J_2 is shown in Fig. 3.3. Again, due to numerical errors from the conversion between the ECI and curvilinear frames, the y axis scale was prevented from enlarging further than 10 μm. Note also that t_0 was chosen to be at a time $t_0 = T/8$, where T is the period, so that the secular motion of the in-track (ξ) component is largely

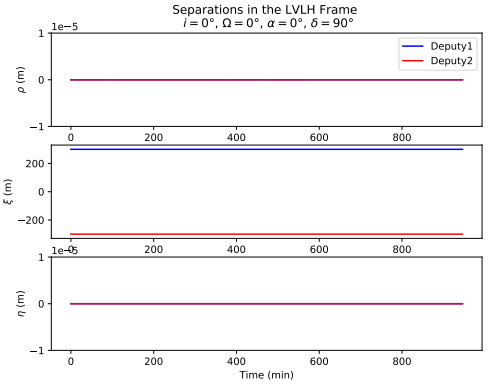

(a) $i = 0°,\ \Omega = 0°,\ \alpha = 0°,\ \delta = 90°$

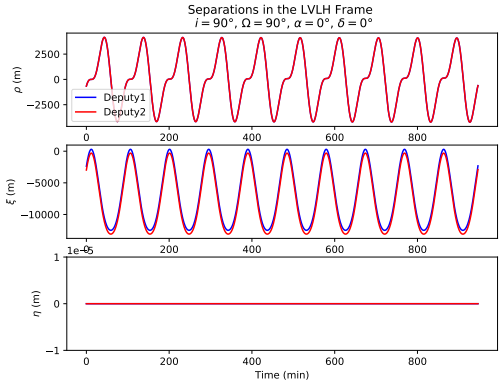

(b) $i = 90°,\ \Omega = 90°,\ \alpha = 0°,\ \delta = 0°$

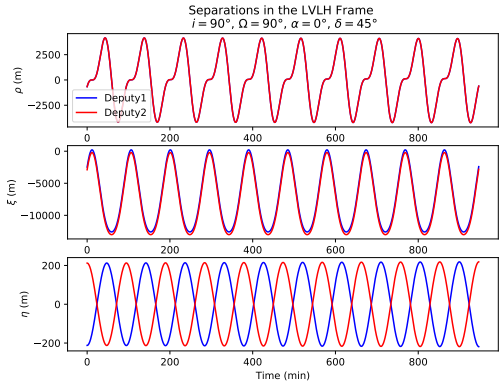

(c) $i = 90°,\ \Omega = 90°,\ \alpha = 0°,\ \delta = 45°$

Figure 3.3: J_2 perturbed motion of the two deputy spacecraft with respect to the reference orbit (n.b. not with respect to the chief), based on the work of Schweighart & Sedwick (2002). Plotted over 10 orbits in the curvilinear LVLH frame for different orbital configurations. Note that the initial conditions were set at $t_0 = T/8$, where T is the period, to remove in-track secular motion.

removed and the periodic nature of the perturbation is viewable.

Under the J_2 perturbation, we see that the equatorial orbit (Fig. 3.3a) is identical to the non-perturbed equivalent up to numerical errors. However, large differences arise in the polar orbit case, both when looking at a star perpendicular to the orbital plane (Fig. 3.3b) and one at 45° from the orbital plane (Fig. 3.3c). The perturbation in this case mainly works on the radial and in-track components of the motion, causing oscillatory behaviour away from the reference orbit. The cross-track motion is largely unaffected, replicating the behaviour of the non-perturbed version.

That being said, when compared against a high precision integration of the ECI equations of motion (equation 3.6), the motions do not agree. A simple example of some of the problems with these equations come from considering a polar orbit, looking at a star perpendicular to the orbital plane (Fig. 3.3b). In this configuration, in the absence of perturbations, the satellites should follow each other in single file around the orbit. Then, when the perturbation is applied, we should expect that an oscillatory phase difference should arise. This is because the chief and deputies are at different latitudes at a given point in time, and so will feel a different magnitude of the J_2 force. When analysing equation 3.15 though, we see that this oscillatory motion will not occur. In the LVLH frame, the only difference in initial conditions between any of the spacecraft in this configuration is the initial in-track offset ξ_0. However, none of the equations have a time varying component including ξ_0 as a parameter, and so the differential perturbation will be zero for all t.

The fundamental reason for this is that Schweighart & Sedwick (2002), like most of the literature on this topic, focus on long term motions of satellites rather than short term sub-orbit motions. This mentality is clearly seen at the beginning of the paper where the J_2 gradient is averaged over a whole orbit, thus removing much of the short term variation from the equations of motion. Furthermore, attempts at subtracting the average and adding the un-averaged gradient were found to be insufficient in matching up with the ECI integration. Hence, these equations are not suitable for our purposes in this thesis, although for long term motions this solution based on the work of Schweighart & Sedwick (2002) may still be very useful.

Rather than deriving a new set of LVLH equation of motion, we instead returned to the ECI equations of motion (Equation 3.6) and integrated these equations directly with a high level of precision due to the large distances involved with the ECI reference frame. As a sanity check, the perturbed motions for a few simple orbit cases were calculated and are shown in Fig. 3.4 and 3.5. These equations were numerically integrated with SciPy's `Solve_IVP` function (Jones et al., 2001), using the Runge-Kutta method of order 5(4) developed by Dormand & Prince (1980). We adopted a relative error tolerance of 1×10^{-12} due to the aforementioned large distances. The tolerance was chosen through a short resolution study, which found that tolerances larger than this resulted in noticeable numerical errors.

The LVLH frame plots (Fig. 3.4) show the differential separation between the deputies and chief that is expected. In an equatorial orbit there is no differential motion, just a constant in-track separation. The minute radial motion shown is an artefact of the fact that the two satellites are not perfectly in a line due to the curvature of the Earth. The polar orbit cases show that, indeed, a phase offset occurs causing oscillatory motion in the radial direction due to the different latitudes of the satellites. The cross-track motion also behaves as in the previous perturbed and non-perturbed cases. The long term motion of the satellites is plotted in Fig. 3.4d, which shows that the radial separation will increase

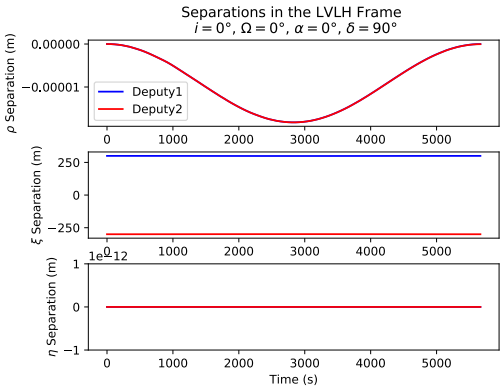

(a) $i = 0°,\ \Omega = 0°,\ \alpha = 0°,\ \delta = 90°$
1 orbit

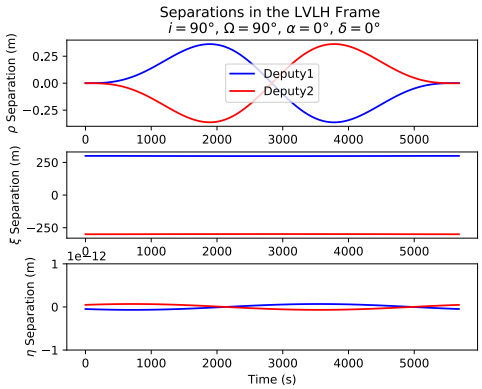

(b) $i = 90°,\ \Omega = 90°,\ \alpha = 0°,\ \delta = 0°$
1 orbit

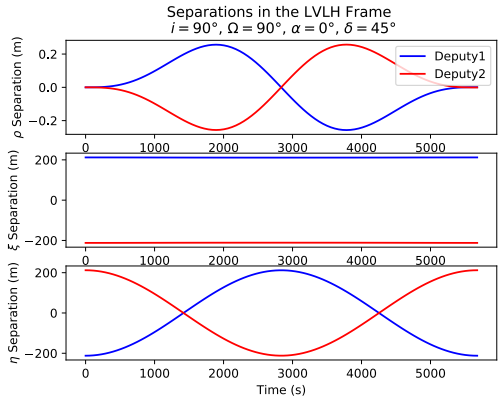

(c) $i = 90°,\ \Omega = 90°,\ \alpha = 0°,\ \delta = 45°$
1 orbit

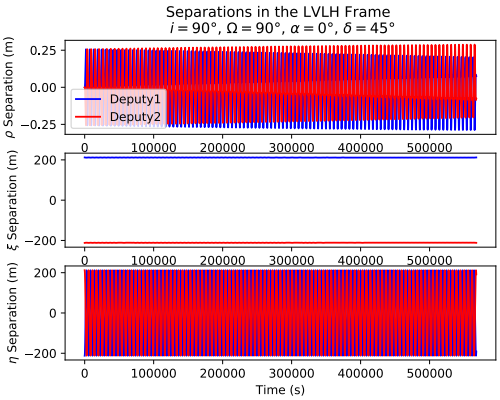

(d) $i = 90°,\ \Omega = 90°,\ \alpha = 0°,\ \delta = 45°$
100 orbits

Figure 3.4: ECI integrated J_2 perturbed motion of the two deputy spacecraft with respect to the chief spacecraft. Integrated using a Runge-Kutta method of order 5(4) (Dormand & Prince, 1980), with a relative error tolerance of 1×10^{-12}. Plotted in the curvilinear LVLH frame for different orbital configurations.

over time if left unchecked, albeit only by a small amount.

Perhaps more importantly, the differential separation in the baseline frame plots (Fig. 3.5) shows the motion that must be corrected over an integration. We see that in all orbits, the J_2 perturbation rotates the baseline about $\hat{\boldsymbol{s}}$ a little on the order of a fraction of a metre, shown by the motion in the $\hat{\boldsymbol{o}}$ direction. It should be noted that Fig 3.5a is an exception, for which the $\hat{\boldsymbol{o}}$ motion is again an artefact of the satellites not being in a line due to the curvature of the Earth. Regardless, this twisting is not important for keeping the optical path length identical between the satellites during integration, and so can be safely ignored. The baseline also appears to behave well, staying constant for configurations with the star perpendicular to the orbital plane, and oscillatory with two periods for other configurations (the baseline breathes in and out twice as the satellites move up and down in the $\hat{\boldsymbol{\eta}}$ direction). The star ($\hat{\boldsymbol{s}}$) direction is the most critical to analyse, as it is in this direction that the primary unwanted motion is caused by J_2 and we want this separation to be zero. The perturbation causes an unwanted separation of 0.5 m for the polar orbit case, looking at a star with 45° declination. This amount of motion should be able to be removed through thrusting during an integration and will be explored in

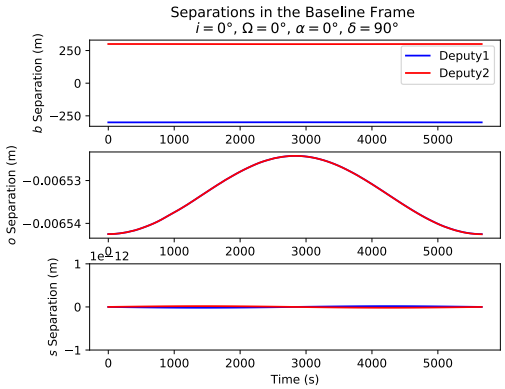

(a) $i = 0°,\ \Omega = 0°,\ \alpha = 0°,\ \delta = 90°$
1 orbit

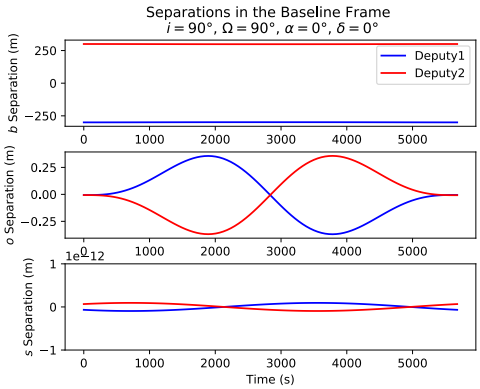

(b) $i = 90°,\ \Omega = 90°,\ \alpha = 0°,\ \delta = 0°$
1 orbit

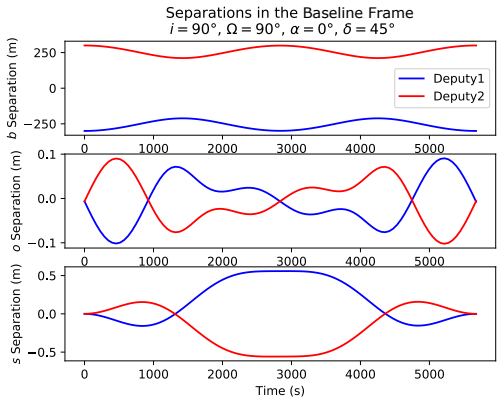

(c) $i = 90°,\ \Omega = 90°,\ \alpha = 0°,\ \delta = 45°$
1 orbit

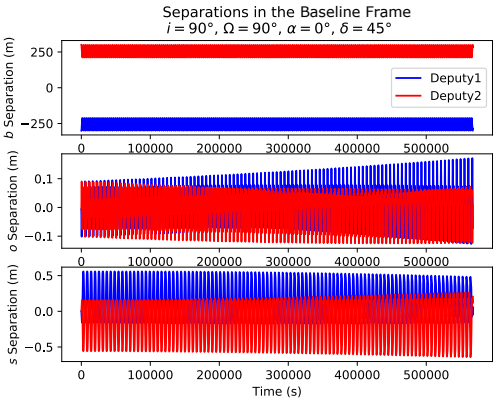

(d) $i = 90°,\ \Omega = 90°,\ \alpha = 0°,\ \delta = 45°$
100 orbits

Figure 3.5: ECI integrated J_2 perturbed motion of the two deputy spacecraft with respect to the chief spacecraft. Integrated using a Runge-Kutta method of order 5(4) (Dormand & Prince, 1980), with a relative error tolerance of 1×10^{-12}. Plotted in the baseline frame for different orbital configurations.

Chapter 4. Overall, we see that the ECI integration method does indeed perform well as long as a very high precision integrator is used.

3.3 Atmospheric drag

We will also do a brief order of magnitude calculation of aerodynamic drag, to determine the effect that it will have on our array and to understand what manoeuvres may be required to correct it. Aerodynamic drag is given by the drag equation (Montenbruck & Gill, 2000):

$$\boldsymbol{a}_{\text{drag}} = -\frac{1}{2}\frac{\rho C A}{m}|v_{\text{rel}}|^2 \hat{\mathbf{v}}_{\text{rel}}, \tag{3.16}$$

where ρ is the density of the atmosphere, A is the cross-sectional area, v_{rel} is the relative velocity of the satellite with respect to the atmosphere, m is the mass of the satellite and C is the drag coefficient.

The relative velocity can be determined through the use of angular velocities:

$$|v_{\text{rel}}| = |\omega \times r - \omega_E \times r|, \tag{3.17}$$

where ω is the angular velocity of the satellite and ω_E is the angular velocity of the Earth. Since $\omega >> \omega_E$, we can approximate the relative angular velocity as the angular velocity of the satellite itself. This corresponds to a linear relative velocity (at 500 km) of about 8 km/s.

From the CIRA Working Group (2012), we find that the atmospheric density at an altitude of 500 km is $8 \times 10^{-13}\,\text{kgm}^{-3}$. We will assume the deputy satellites are 3U CubeSats, with a mass of 4 kg and a cross-sectional area of $0.03\,\text{m}^2$. Since CubeSats are roughly rectangular, the drag coefficient will be assumed to be about two (Moe et al., 2013). This then gives an approximate acceleration due to drag of

$$\boldsymbol{a}_{\text{drag}} \approx -3 \times 10^{-7} \hat{\mathbf{v}}_{\text{rel}}\,\text{m/s}^2.$$

Since drag works against the motion of the satellite, it has the effect of slowing it down. This decreases the energy of the satellite, and so it will lose altitude. Over the long term, this is ideal as a satellite has to be able to deorbit within a time frame of 25 years (European Space Agency, 2015). Starting with the vis-viva law for circular orbits (Montenbruck & Gill, 2000),

$$v^2 = \frac{\mu}{r}, \tag{3.18}$$

and taking the time derivative gives

$$\frac{\mathrm{d}r}{\mathrm{d}t} = \frac{-2\mu}{v^3}\frac{\mathrm{d}v}{\mathrm{d}t}. \tag{3.19}$$

We then want to calculate the characteristic time it will take for the array to drop one scale height $\Delta r = H$, where the scale height is the height at which the atmospheric pressure drops by e. From CIRA Working Group (2012), we identify the scale height at 500 km to be approximately 70 km. The time taken to decend this distance is hence

$$\begin{aligned}\Delta t &\approx \frac{-v^3}{2\mu a_{\text{drag}}}\Delta r \\ &= 4.75\,\text{yr}.\end{aligned}$$

This shows that we should be able to both comfortably achieve our desired mission length of three years, while also deorbiting long before the 25 year deadline.

We also must consider differential drag and the effect it will have on our array. Recall that the optical path difference is the ultimate constraint we have, given by

$$D = |\Delta \boldsymbol{r}_1| - \Delta \boldsymbol{r}_1 \cdot \hat{\boldsymbol{s}} - |\Delta \boldsymbol{r}_2| + \Delta \boldsymbol{r}_2 \cdot \hat{\boldsymbol{s}} \approx 0, \tag{3.20}$$

where $\Delta \boldsymbol{r}_1$ is the separation between the chief spacecraft and the first deputy, $\Delta \boldsymbol{r}_2$ is similar for the second deputy and $\hat{\boldsymbol{s}}$ is the unit vector in the direction of the star. Differential drag will work to change the separation lengths of each spacecraft, shortening one and lengthening the other. To compensate this, instead of installing a thruster to move in the baseline direction, we could change the separation in the star

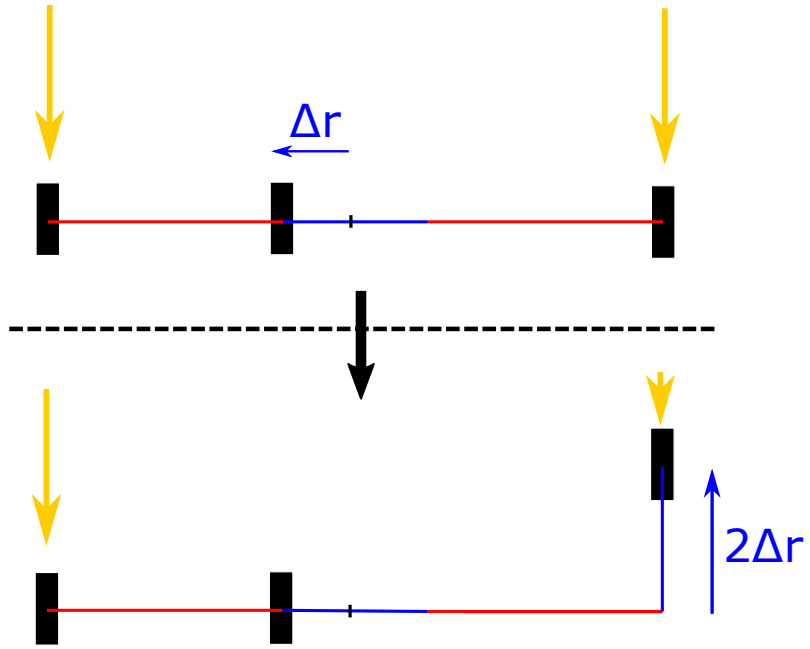

Figure 3.6: Potential routine for correcting for drag. In the top panel, drag has caused the chief to move a distance Δr from the centre of the array. To correct for this, we could boost the deputy with the longer separation up $2\Delta r$ in the direction of the star. Essentially, compensating an increase in $|\Delta \boldsymbol{r}|$ with an increase in $\Delta \boldsymbol{r} \cdot \hat{\boldsymbol{s}}$, so that D is kept close to 0 (see Equation 3.20).

direction and then angle the mirror on the deputy via an actuator. A diagram of this is shown in Fig. 3.6.

We can take the approximation that the satellites are moving in the same direction, at the same velocity, with the same drag coefficient. The only parameters that should really affect differential drag are the mass of each spacecraft and their cross sectional area. The chief spacecraft would likely have twice the mass of the deputies, but by a similar token have twice the cross sectional area, rendering the differential drag to be zero. However, with solar panels, we can make a worst case approximation that the chief and deputies have the same area, meaning that the differential drag will be half that of the absolute drag on a deputy, or about $1 \times 10^{-7}\,\mathrm{ms}^{-2}$. Over half an orbit ($t = 2700\,\mathrm{s}$), we then get a displacement of

$$\begin{aligned} \Delta r &= \frac{1}{2} a t^2 \\ &\approx 35\,\mathrm{cm}. \end{aligned}$$

As the drag displacement shortens one path and lengthens the other (see Fig. 3.6), we must compensate for twice the displacement to make the paths equal. Thus, to correct a change in separation of this magnitude, we could thrust one of the deputies up by 70 cm. Over a 300 m chief/deputy separation, this would correspond to an angular change of 0.1°, and so would remain in the field of view of the chief satellite. Adjusting for this small angular change should also be achievable with an actuator attached to the mirror. Further studies comparing this approach with the power and space constraints of an additional thruster should be conducted in the future.

Chapter 4

Orbital Corrections and Constraints

In the previous chapter, we identified how the satellite array will be perturbed from its original orbit due to the influence of the J_2 geopotential term. What is more significant, however, is how to correct these perturbations. In this chapter, we will describe three categories of orbital corrections and identify the requirements needed to perform these manoeuvres, specifically in terms of the Δv budget. The first two detail the corrections needed during a regular orbit: one during integration (i.e. when the star is being observed) and the other correcting the orbit during the recharge phase (when the array is on the daylight side of the Earth). The final type of orbital manoeuvre are those that are required for when the target of interest or maximum baseline is changed.

4.1 The delta-v budget

In each correction, the most important parameter we will discuss is Δv, which is the change in velocity due to an impulsive manoeuvre (Curtis, 2014). This is related to the amount of fuel required by the manoeuvre by the Tsiolkovsky (or ideal) rocket equation,

$$\Delta v = I_{\text{sp}} g \ln \frac{m_0}{m_f}, \tag{4.1}$$

where I_{sp} is the specific impulse of the thruster, g is the standard gravitational acceleration, m_0 is the wet mass (mass including propellant), and m_f is the dry mass (mass without propellant). This tells us something profound: for a given thruster, the amount of Δv required over the lifetime of the satellite array determines the amount of fuel that is required (Pettit, 2012). Conversely, for a set amount of fuel, it also then determines the amount of Δv that can be used during the mission. This is a concept known as the delta v budget - essentially, Δv can be used as a stand in for the amount of fuel required.

We can do a few approximations to identify the amount of Δv that we have to work with. Considering the Enpulsion Spacecraft Technology (2018) microthruster, we see that for a 3U CubeSat at 5 kg (such as the deputies), a single thruster would provide approximately $\Delta v \approx 1.5\,\text{km/s}$ in total over the lifetime of the thruster, and for a 10 kg CubeSat (such as the chief), this would decrease to about $750\,\text{m/s}$. Having a single thruster for each satellite would be ideal, due to cost, power and space requirements. Assuming a mission length of three years and a period of 90 min (orbital altitude of 500 km), we find that, per orbit, we have a Δv budget of $\sim$0.08 m/s for the deputies and $\sim$0.04 m/s for the chief.

4.2 Correcting during integration

Firstly, we will consider correcting the perturbations during the period of integration - when the array is looking at the star. This is for approximately the first half of the orbit, while the array is on the nighttime side of the Earth. During this time the optical path difference needs to be kept within 5 cm as detailed in Chapter 1. This is the main requirement, and so we will only focus on correcting the components of the optical path difference rather than the total position and velocity. Recall that the optical path difference is given as

$$D = |\Delta \boldsymbol{r}_1| - \Delta \boldsymbol{r}_1 \cdot \hat{\boldsymbol{s}} - |\Delta \boldsymbol{r}_2| + \Delta \boldsymbol{r}_2 \cdot \hat{\boldsymbol{s}} \approx 0. \tag{4.2}$$

where $\Delta \boldsymbol{r}_j$ is the separation between the chief and deputy j. The path difference can be split into two components: the baseline separation and the star separation. The baseline separation is given by:

$$\Delta b = |\Delta \boldsymbol{r}_1| - |\Delta \boldsymbol{r}_2|. \tag{4.3}$$

We also calculate the component of the separation in the star's direction, Δs_j:

$$\Delta s_1 = \Delta \boldsymbol{r}_1 \cdot \hat{\boldsymbol{s}} \qquad\qquad \Delta s_2 = \Delta \boldsymbol{r}_2 \cdot \hat{\boldsymbol{s}}. \tag{4.4}$$

If we take the time series of these values over the course of an orbit, we can also calculate the maximum acceleration they cause, as well as the Δv required to counteract them. This is calculated for a separation Δx below:

$$\begin{aligned} \max(a_x) &= \max(|\ddot{\Delta} x|) \\ \Delta v_x &= \int |\ddot{\Delta} x|, \end{aligned} \tag{4.5}$$

where $\ddot{\Delta} x$ can be found by taking the numerical gradient of the time series twice.

The above way that Δv is calculated assumes that the thrust direction can be in any direction, but under the baseline thruster configuration, all three satellites can only thrust upwards in the $\hat{\boldsymbol{s}}$ direction. Despite this, we can still make an approximation that should give us an upper bound on the required Δv. Considering the $\hat{\boldsymbol{s}}$ direction, if the separation is negative then the satellite must thrust in a positive direction. On the other hand, if the satellite has a positive separation, then rather than thrusting negatively, we can force the other two satellites to thrust positively. Hence, the deputies will thrust at most $2\Delta v_s$: once for their own positive thrusts and once for the other deputy's negative thrusts. Conversely, the chief will only require one of these thrusts - the perturbations on the two deputies should be symmetrical about the chief, and so the combined "negative" thrusts of the deputies should equal Δv_s.

For the baseline direction, as we discussed in Section 3.3 we can compensate a change in the baseline direction with a shift in the $\hat{\boldsymbol{s}}$ direction. Again, we cannot disentangle which of the deputies has a longer baseline at a given point, so as another approximation we will take a worst case scenario and add the Δv in this direction to both of the deputies.

Table 4.1: Table of the maximum Δv required to correct for the J_2 perturbation over half an orbit for various orbital configurations. Taken at an altitude of 500 km with a maximum chief/deputy separation of $|\Delta \boldsymbol{r}_{\max}| = 300\,\text{m}$.

Inclination (i) [°]	Longitude of the ascending node (Ω) [°]	Right Ascension (α) [°]	Declination (δ) [°]	Max Acceleration [$\times 10^{-6}\,\text{m/s}^2$]		Δv [$\times 10^{-3}\,\text{m/s}$]		Percentage of Δv budget	
				Chief	Deputy	Chief	Deputy	Chief	Deputy
0	0	0	90	0.00	0.00	0.00	0.00	0.00	0.00
90	90	0	0	0.00	0.00	0.00	0.00	0.00	0.00
90	90	0	45	0.95	1.91	1.38	2.79	3.46	3.49
45	0	90	20	1.28	2.60	2.10	4.23	5.24	5.29
80	0	80	20	0.97	1.96	1.70	3.41	4.24	4.26

Therefore we have that the maximum Δv for all three satellites is

$$\begin{aligned} \Delta v_1 &< 2\Delta v_s + \Delta v_b \\ \Delta v_2 &< 2\Delta v_s + \Delta v_b \\ \Delta v_c &< \Delta v_s. \end{aligned} \tag{4.6}$$

It should be noted that the Δv_b component will be nearly negligible as J_2 primarily acts on the array as a whole: the zeroth order term is a translation of the whole array, and the first order term is a rotation of the array due to the gradient of J_2. This is what gives rise to the Δv_s component. The baseline component is an asymmetric stretching of the array, which is only influenced by the much higher order tensor terms of the J_2 perturbation.

The time series of the various separations for various orbital parameters were taken, and the Δv calculated for each one. Here, we've assumed an altitude of 500 km and a maximum chief/deputy separation of 300 m. The results are given in Table 4.1. We see that over half an orbit, even in the worst case scenario, we use around 5% of the orbital Δv budget. This is good as it highlights that with a proper control system, even though we have limited ourselves to thrusting in a single direction, we should be able to counteract the perturbation comfortably. To identify the exact Δv required for these orbits using finite thrusts will require a detailed control simulation. This is a priority for future work, as it will also identify the optical path delay residuals that require correction.

We can also do a rough estimate of the Δv required to correct atmospheric drag as explained in Section 3.3. Recall that one deputy was required to thrust 70 cm over half an orbit. This corresponds to a Δv of approximately 0.3 mm/s, or equivalently 0.3% of the budget; a tiny fraction that again highlights that J_2 is the most important perturbation to consider.

4.3 Correcting the rest of the orbit

4.3.1 One orbit

We also need to identify the Δv required to correct the other half of the orbit and get the array back into position. Though we do not have the optical path constraint as before due to the fact we are not taking measurements, we have a secondary constraint in that we must have ample time to charge the array's batteries. Hence, we need to limit the time that the satellites are active and allow the array to passively charge for a majority of the

Table 4.2: Table of the Δv required to correct the recharge portion of the orbit for various orbital configurations. Taken at an altitude of 500 km with a maximum chief/deputy separation of $|\Delta \boldsymbol{r}_{\max}| = 300$ m.

Inclination (i) [°]	Longitude of the ascending node (Ω) [°]	Right Ascension (α) [°]	Declination (δ) [°]	Δv [$\times 10^{-3}$ m/s]	Percentage of Δv budget
0	0	0	90	0.00	0.00
90	90	0	0	0.01	0.01
90	90	0	45	0.86	1.07
45	0	90	20	2.58	3.23
80	0	80	20	0.81	1.01

orbit.

One way to do this is to limit the number of thrusts, but optimise them so that they take the spacecraft as close to the beginning of the orbit as possible. Considering that a thrust is three parameters (three velocity components) and that the end state is six parameters, the minimum number of thrusts we need is two. We will conduct one thrust at 10 minutes after finishing the integration, to allow the array to passively charge for a short period of time. The second thrust will be 10 minutes before restarting integration; a balance between giving enough time for attitude correction and recharging the batteries. These thrusts can be in any direction as we can change where each spacecraft is pointing during this portion of the orbit.

The desired end state of the satellites will not be the initial configuration, as the chief satellite will be perturbed considerably and would require a large amount of thrust to return to the exact same position. As we are only concerned with the relative position of the deputies with respect to the chief, we can safely ignore the absolute position of the chief and allow it to propagate unchecked.

Mathematically, if the chief satellite has an end position $\boldsymbol{r}_c$ and velocity $\boldsymbol{v}_c$, then the angular momentum unit vector of the chief is

$$\hat{\boldsymbol{h}} = \frac{\boldsymbol{r}_c \times \boldsymbol{v}_c}{|\boldsymbol{r}_c \times \boldsymbol{v}_c|}. \tag{4.7}$$

Using this, we can go through the calculations detailed in Section 2.3 to determine the rotations that will convert from the chief's position and velocity into the deputies'. These deputy states are thus the positions and velocities we will aim to arrive at after the remaining half an orbit.

Let us consider that after two thrusts, deputy j has final state vector $\boldsymbol{X}_{\boldsymbol{f}_j} = [r_{bj}, r_{oj}, r_{sj}, \dot{r}_{bj}, \dot{r}_{oj}, \dot{r}_{sj}]$ in the baseline frame. Let us then say that the desired end state vector is $\boldsymbol{Y}_{\boldsymbol{f}_j}$. The residuals are then:

$$\boldsymbol{\Delta X}_{\boldsymbol{f}_j} = \boldsymbol{X}_{\boldsymbol{f}_j} - \boldsymbol{Y}_{\boldsymbol{f}_j}. \tag{4.8}$$

Since we have six unknowns per deputy satellite, and the end state has six parameters, we can explicitly solve for the thrusts such that the residuals are zero: $\boldsymbol{\Delta X}_{\boldsymbol{f}_j} = 0$. This was done using SciPy's `root` function, in particular the hybrid Powell method (Jones et al. (2001); More et al. (1980)).

The initial positions of the spacecraft were chosen to be the end positions after half an orbit had been completed; that is, at the end of the orbit described in the previous section.

To account for the fact that the orbit will have been corrected in some directions during integration, the separation in the star direction was forced to be 0. The combined Δv over the second half of the orbit, using two thrusts to correct for perturbations, is given in Table 4.2 for a number of orbital configurations. Again, we have assumed an altitude of 500 km with a maximum chief/deputy separation of $|\Delta \boldsymbol{r}_{\max}| = 300\,\text{m}$. We immediately see that this does not use up much Δv - it is less than half of the required amount during the integration half of the orbit. Furthermore, we should note that this is a maximum. We are able to relax some of the constraints on the root finder and convert the problem into an optimisation one, where we optimise over the residuals and the Δv vector. In this way, we can further decrease the Δv usage by constraining $\Delta s_1 = \Delta s_2 = \Delta b = 0$ while relaxing the other dimensions. Alternatively, we could choose different thrust times that may allow for a further reduction in Δv.

4.3.2 Multiple orbits

Now, we can then string together these two processes: correcting during integration and finding the ideal two thrusts in the second half of the orbit that will take the array back to the starting position. This is useful to see whether the amount of thrust needed will increase over subsequent orbits.

Interestingly, we found that the Δv usage increased slightly per orbit over the course of ten orbits, albeit only by a small amount: less than 0.5% per orbit. This is smaller than other perturbations that are not being considered at this stage and hence will be disregarded in this feasibility study. We believe that this is likely due to a numerical error in the simulation, and subsequent, more comprehensive simulations will need to remove this drift in Δv.

4.4 Reconfiguring the orbit

We turn to the problem of how much Δv is required to change baselines or targets for the satellite system. This comes in two components: the change in the orbital plane of the spacecraft and the change in phase. This discussion will only consider baseline/star vector changes, and not changes in the chief's orbit. For that reason, we only need to consider the effect on the deputy spacecraft.

Consider two different spacecraft configurations, denoted with subscripts α and β. Our aim is to find the Δv required to change from configuration α to β. We first need to find a point where the two orbits intersect. More specifically, we want the point on the orbit that lies on the intersection of the two orbital planes. This is because at the point where they intersect, we can thrust in a certain direction to immediately change the plane. Since the angular momentum vector is perpendicular to the plane of the orbit, the cross product of the angular momentum vectors of each orbit will give us a vector along this intersection:

$$\boldsymbol{r} = \boldsymbol{h}_\alpha \times \boldsymbol{h}_\beta. \tag{4.9}$$

Of course, we only have the angular momentum vector of the chief orbit. Hence, to get the angular momentum vectors of the deputies, we simply rotate the chief $\boldsymbol{h}_c$ vector by

the associated deputy's quaternion ($\boldsymbol{q}_d$, see Section 2.3):

$$\boldsymbol{h}_{dj} = \boldsymbol{Q}(\boldsymbol{h}_c, \boldsymbol{q}_{dj}), \tag{4.10}$$

where j represents the configuration α or β. Thus, we find the point of intersection is

$$\boldsymbol{r}_d = \frac{\boldsymbol{h}_{d\alpha} \times \boldsymbol{h}_{d\beta}}{|\boldsymbol{h}_{d\alpha} \times \boldsymbol{h}_{d\beta}|} \cdot R_{\text{orb}}. \tag{4.11}$$

We now want to find the time in each of the two configurations that the deputy reaches this intersection point. Firstly, let's take this intersection position ($\boldsymbol{r}_d$) and find the location of the chief at this given moment:

$$\boldsymbol{r}_{cj} = \boldsymbol{Q}(\boldsymbol{r}_d, \boldsymbol{q}_{dj}^{-1}). \tag{4.12}$$

Then, let's rotate the chief orbit onto the $\hat{\boldsymbol{x}} - \hat{\boldsymbol{y}}$ plane, by performing the reverse rotation that was done in determining the orbit:

$$\boldsymbol{r}'_{cj} = \boldsymbol{Q}(\boldsymbol{r}_{cj}, \boldsymbol{q}_c^{-1}). \tag{4.13}$$

We can easily work out the exact phase (angle) that this point corresponds to in the orbit:

$$\phi = \arctan 2(r'_{cjx}, r'_{cjy}). \tag{4.14}$$

Knowing the angular velocity of the orbit, ω, we can work out the time taken to reach that point:

$$t = \frac{\phi}{\omega}. \tag{4.15}$$

Putting it all together gives

$$t_{dj} = \frac{\arctan 2(\boldsymbol{Q}(\boldsymbol{r}_d, \boldsymbol{q}_c^{-1}\boldsymbol{q}_{dj}^{-1})_x, \boldsymbol{Q}(\boldsymbol{r}_d, \boldsymbol{q}_c^{-1}\boldsymbol{q}_{dj}^{-1})_y)}{\omega}, \tag{4.16}$$

where d is the deputy number and j is the greek letter associated with the configuration.

With that, we can now calculate the Δv requirements. First, for the plane change, we can calculate this value directly. That is, propagate each deputy along each of the orbits for the amount of time calculated above, and retrieve the velocity at that time:

$$\boldsymbol{v}_{d\alpha} = \boldsymbol{v}_{t=t_{d\alpha}} \qquad\qquad \boldsymbol{v}_{d\beta} = \boldsymbol{v}_{t=t_{d\beta}}. \tag{4.17}$$

The Δv requirement is simply the magnitude in the difference of the velocities for each orbit:

$$\Delta v_{d,\text{inc}} = |\boldsymbol{v}_{d\alpha} - \boldsymbol{v}_{d\beta}|. \tag{4.18}$$

The phase requirement is more complicated, as it requires what is known as a phasing manoeuvre. This is defined as a transfer to and from its own orbit, using a change in radius (and hence period) that allows it to adjust for the time requirement (Curtis, 2014). We will start by considering a phase change over a single orbit. First, we need to work out the period for the new orbit. This is the old period, plus the extra/lesser time we

Table 4.3: Δv required to change the target or baseline for various declinations and orbital modifications. The change in configuration refers to either looking at a star with an α/δ that is offset from the original target by a few degrees, or a shortening/lengthening of the baseline. Taken at an altitude of 500 km, with $i, \Omega = 0°$, initial $\alpha = 0°$ and default maximum baseline $|\Delta \boldsymbol{b}_{\max}| = 600$ m.

Initial Declination (δ) [°]	Change in Configuration	Δv Plane [$\times 10^{-3}$ m/s]	Δv Phase [$\times 10^{-3}$ m/s]	Δv Total [$\times 10^{-3}$ m/s]
0	$\Delta\delta = 1°$	0.05	0.62	0.67
0	$\Delta\alpha = 1°$	5.80	0.00	5.80
90	$\Delta\delta = 1°$	5.80	0.00	5.80
90	$\Delta\alpha = 1°$	0.00	0.00	0.00
45	$\Delta\delta = 1°$	4.14	0.44	4.58
45	$\Delta\alpha = 1°$	4.10	0.00	4.10
45	$\Delta\delta = 1°, \Delta\alpha = 1°$	5.80	0.44	6.24
45	$\Delta\delta = 2°$	8.34	0.86	9.20
45	$\Delta\alpha = 2°$	8.20	0.00	8.20
45	$\Delta\delta = 2°, \Delta\alpha = 2°$	11.6	0.86	12.4
45	$0.5\times\|\Delta \boldsymbol{b}_{\max}\| = 300$ m	118	12.5	130

have due to the phase difference. In other words:

$$T'_d = T_d + (t_{d\beta} - t_{d\alpha}). \tag{4.19}$$

We can just use T_d, as the periods of the two different configurations should be the same. Now, we can calculate the semi major axis of this transfer orbit using

$$a'_d = \left(\mu \left(\frac{T'_d}{2\pi}\right)^2\right)^{\frac{1}{3}}, \tag{4.20}$$

where μ is the Earth's standard gravitational parameter. The velocity can be calculated using the vis-viva equation (Montenbruck & Gill, 2000):

$$v'_d = \sqrt{\mu \left(\frac{2}{R_{\text{orb}}} - \frac{1}{a'_d}\right)}. \tag{4.21}$$

The Δv is simply twice the difference between this velocity and the original speed - once for transferring into the phasing orbit, and once for returning to the original orbit:

$$\begin{aligned} \Delta v_{d,\text{phase}} &= 2(v'_d - v_d) \\ &= 2\left(\sqrt{\mu \left(\frac{2}{R_{\text{orb}}} - \frac{1}{a'_d}\right)} - \sqrt{\frac{\mu}{R_{\text{orb}}}}\right). \end{aligned} \tag{4.22}$$

This is a maximum bound for the Δv phase requirement, as instead of phasing in a single orbit, we can spend multiple orbits to correct for the same requirement. For N orbits, that means we want $T'_d = T_d + \frac{(t_{d\beta} - t_{d\alpha})}{N}$; for more orbits we require a smaller period change and hence a smaller Δv. Putting it together gives the total Δv for a given deputy d changing between two configurations:

$$\Delta v_d = \Delta v_{d,\text{inc}} + \Delta v_{d,\text{phase}}. \tag{4.23}$$

Table 4.3 shows the Δv required for a variety of star vector changes. It should be

noted that this reconfiguration calculation is agnostic of the Earth's axis, and so the orbital parameters i, Ω are degenerate with α, δ. Hence, both were set to zero. Similarly, the starting right ascension of a star will not affect how much Δv is required to change the configuration and so this was also set to zero in the table. Finally, the altitude of the array was set at 500 km and the maximum baseline separation ($|\Delta \boldsymbol{b}_{\max}| = 2|\Delta \boldsymbol{r}_{\max}|$) was set to 600 m. As we can see, generally the Δv is quite small to change the orientation of the spacecraft by a few degrees: only about 1×10^{-3} m/s or so. Furthermore, we see changing α does not require a phasing manoeuvre, and that changing α and δ at the same time is cheaper than doing both separately.

We can also calculate the maximum Δv for a plane change given a maximum baseline of 600 m. From Curtis (2014), the Δv required for an orbital plane change of angle θ is:

$$\Delta v(\theta) = 2v \sin \frac{\theta}{2}, \tag{4.24}$$

where v is the velocity of the spacecraft. For an altitude of 500 km, recall this is roughly 8 km/s. The maximum angular change of the array is simply $\theta = \frac{|\Delta \boldsymbol{b}_{\max}|}{R_{\text{orb}}} = 8.72 \times 10^{-5}$ radians. This gives a maximum Δv of 0.68 m/s, which while substantial, is the absolute maximum a reconfiguration would require (looking at a star on the complete opposite end of the sky). This is the equivalent of 10 orbits worth of the Δv budget, and so overall we can conclude that the thrust required to change between stars, given they are roughly in the same area on the sky, is minimal.

One final change was included in Table 4.3: that of changing the maximum baseline ($\Delta \boldsymbol{b}_{\max}$). As we can see, halving the baseline to 300 m results in a large Δv of 0.13 m/s. Hence, the maximum baseline should not be varied much unless necessary.

4.5 Summary

Adding these three corrections together gives us the total amount of Δv required. A summary of this is found in Fig. 4.1, showing the three corrections and the amount of Δv required by a deputy satellite to correct for perturbations over the course of a year. This was calculated using the maximum Δv required for the integration and recharging halves of an orbit (using Tables 4.1, 4.2) and multiplying by the number of orbits in a year. Assuming a 500 km orbit with a period of 90 min, this results in 5840 orbits per year. To factor in reconfiguration, we also assumed that a correction of $\sim 5°$ was made per day. This is a rough estimate that should allow us to both change targets, as well as correct for the positioning of the star, where the star will move slightly with respect to the orbit due to the Earth's rotation around the Sun.

Overall, we find that the deputy satellites will use roughly 50 m/s per year, which is 10% of the yearly Δv budget that a single thruster would provide (500 m/s/yr). This is a very useful result, showing that the one thruster model should be sufficient and that we have a large amount of headroom for other thrust requirements, such as the control system and emergency manoeuvres.

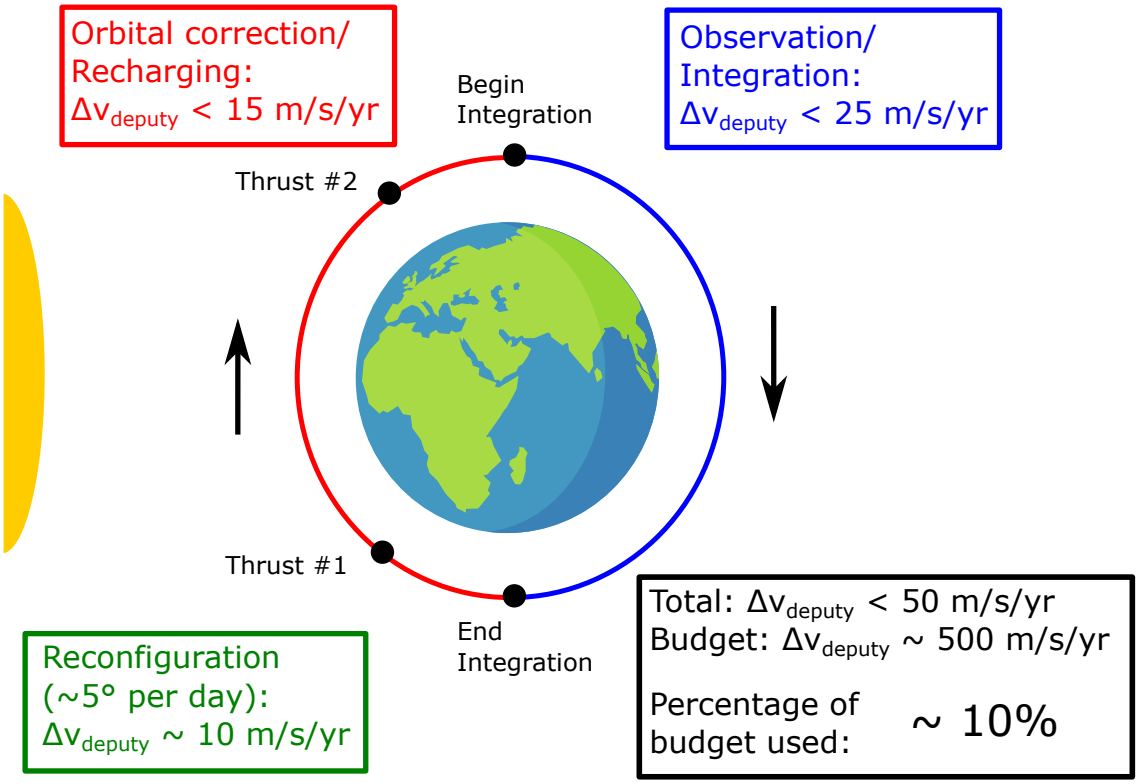

Figure 4.1: Summary of the Δv required by a deputy satellite to correct for orbital perturbations over a year.

Chapter 5

Observability of the Satellite Array

A key part of this mission simulation is how much of the sky is observable over a given year of observations and how the various orbital parameters affect this coverage. In this chapter, we will determine whether an object is observable. Then, we will delve into how much the satellite can see in a given amount of time, both in terms of sky observability (if a star is viewable), as well as the interferometric UV plane coverage.

5.1 Is it observable?

There are two main factors in identifying whether a star is observable:

1. Is the telescope pointing sufficiently far enough away from the Sun?
2. Is the Earth obscuring the star?

For a star to be observable, we must address both criteria. There is a potential third criteria, in whether light from the Earth will interfere with the light path between the spacecraft. However, for our orbital configuration this will not be an issue as the array should always be tangential to the surface of the Earth. Here, Ireland (2019, personal communication) also notes that the reflected light from the Moon is generally not important as long as we restrict science targets to a magnitude of $\sim m_V < 15$. Finally, we don't consider occultations by the moon, as they are generally short and only block a small area of the sky ($\sim 0.5°$). We will now tackle each of the two main criteria in turn.

5.1.1 The Sun

For the spacecraft to see an object, it must be within some angle of the antisolar (opposition) axis, γ. This is so that the satellite array avoids both pointing at the sun, and having the baseline point towards the sun where the sun can interfere with the scientific measurements. A schematic of this is in Fig. 5.1. We want to have a wide angle in order to see as much of the sky as possible. However, for our spacecraft, we note that $\gamma = 60°$ antisolar is the upper limit for how wide we can go with deployable baffling.

The antisolar axis can be found by simply finding the position vector of the Earth with respect to the Sun. This approximation is valid as 1 AU is much larger than the orbital radius, R_{orb}. We will define $t = 0$ such that the spacecraft is on the other end of the Earth from the Sun - that is, the Sun is in the -$\hat{\boldsymbol{x}}$ direction in the Earth-centred inertial (ECI) frame. This is shown in the diagram in Fig. 5.2.

Since we know the angular velocity of the Earth around the Sun ($\omega_\oplus$), we can calculate the position of the Earth at a given time. The Earth is tilted; a phenomena known as

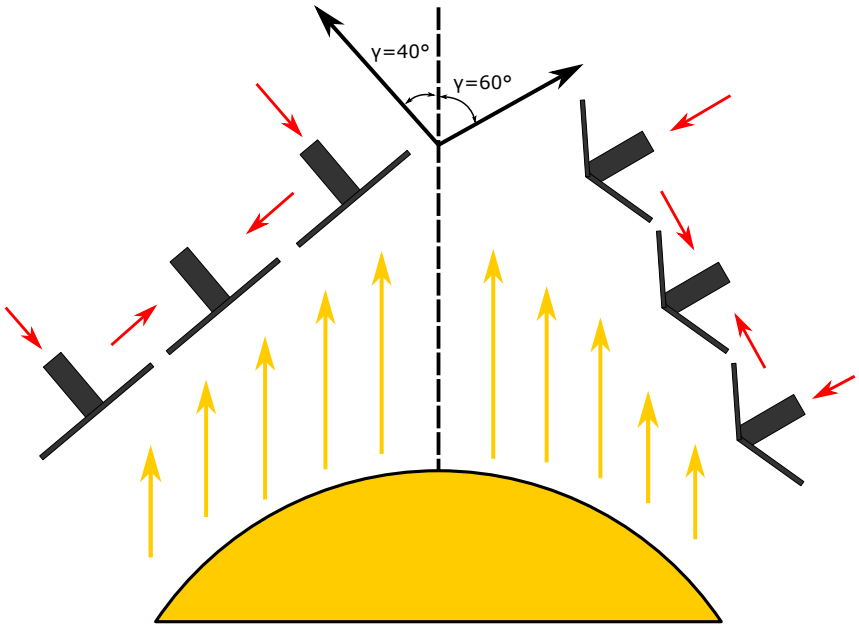

Figure 5.1: Schematic of keeping the satellite array within 40/60° of the antisolar axis. Note that the solar panels can be used to baffle the sun, even for high antisolar angles γ, by folding them inwards slightly.

the obliquity of the ecliptic where $\varepsilon = 23.4°$. Since the ECI frame has the fundamental $\hat{\boldsymbol{x}} - \hat{\boldsymbol{y}}$ plane along the equator, we need to include the obliquity in calculating the Earth's position. Using trigonometry, we find the conversion between ecliptic coordinates (plane of the Earth's orbit around the Sun) to equatorial coordinates (same orientation as the ECI frame, but centred on the Sun) to be (from Seidelmann et al. (1992))

$$\begin{aligned}\boldsymbol{r}_{\text{equatorial}} &= \begin{bmatrix}1 & 0 & 0\\ 0 & \cos(\varepsilon) & -\sin(\varepsilon)\\ 0 & \sin(\varepsilon) & \cos(\varepsilon)\end{bmatrix}\boldsymbol{r}_{\text{ecliptic}}\\ &= \boldsymbol{R}_{\varepsilon}\boldsymbol{r}_{\text{ecliptic}}.\end{aligned} \tag{5.1}$$

Here, the ecliptic coordinate system has the fundamental $\hat{\boldsymbol{x}} - \hat{\boldsymbol{y}}$ plane aligned with the ecliptic, and the $\boldsymbol{x}$ direction aligned with the vernal equinox (Υ). Using this, we can now calculate the Earth's position with respect to the Sun in the equatorial coordinate system, approximating the Earth's orbit as circular:

$$\begin{aligned}\omega_{\oplus} &= \frac{2\pi}{365\cdot 24\cdot 60\cdot 60} \approx 2.0\times 10^{-7}\,\text{Hz}\\ \boldsymbol{r}_{\oplus} &= \boldsymbol{R}_{\varepsilon}\begin{bmatrix}\cos(\omega_{\oplus}t)\\ \sin(\omega_{\oplus}t)\\ 0\end{bmatrix}\\ &= [\cos(\omega_{\oplus}t), \sin(\omega_{\oplus}t)\cos(\varepsilon), \sin(\omega_{\oplus}t)\sin(\varepsilon)].\end{aligned} \tag{5.2}$$

Then, the check to determine whether the object is viewable within an antisolar angle γ is simply

$$\cos^{-1}(\hat{\boldsymbol{s}}\cdot\boldsymbol{r}_{\oplus}) < \gamma. \tag{5.3}$$

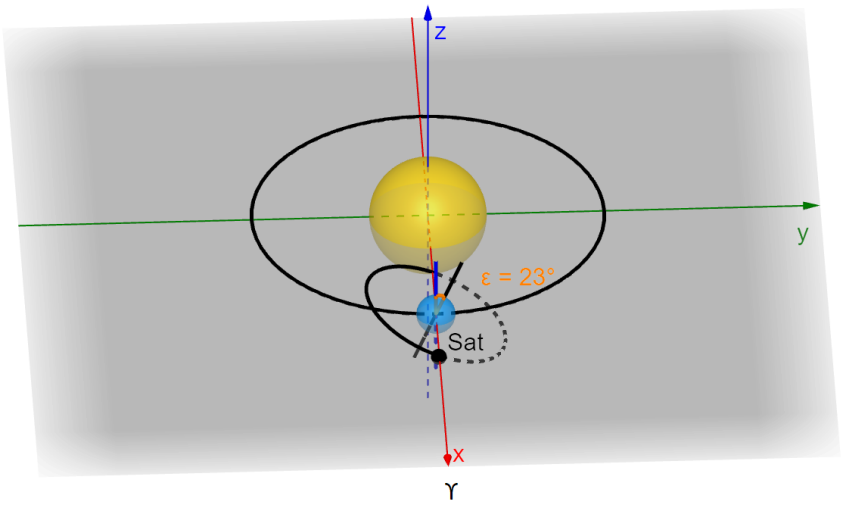

Figure 5.2: Comparing the Ecliptic and Earth-centred inertial (ECI) coordinate frames. The $\hat{\boldsymbol{x}}$ axis aligns with the vernal equinox (Υ).

5.1.2 The Earth

For the Earth's contribution, we simply want to know if the Earth is blocking each satellite's view of the target. First, consider the position of one of the deputy satellites, $\boldsymbol{r}_d$. The deputy can be in one of two states: either the Earth is in between the star and the satellite, or the Earth is behind the satellite with the satellite facing the star. If it is in the latter state, then the solution is trivial: the star is viewable. The situations can be distinguished by taking the dot product of the position vector with the star vector and checking if it is positive:

$$\text{Star is viewable if } \hat{\boldsymbol{s}} \cdot \boldsymbol{r}_d > 0. \tag{5.4}$$

If the dot product is negative, then we have to check more thoroughly. Specifically, we must check that the component of the satellite's position vector perpendicular to $\hat{\boldsymbol{s}}$ is outside the radius of the Earth (R_E). This component is simply the vector rejection of the satellite's position vector with respect to the star, and so the test can be written as

$$|\boldsymbol{r}_d - (\boldsymbol{r}_d \cdot \hat{\boldsymbol{s}})\hat{\boldsymbol{s}}| < R_E. \tag{5.5}$$

To account for the fact that the Earth emits light which could be optically scattered into our field of view, we need to increase the radius of the Earth by some amount. Concerning the following derivation, refer to Fig. 5.3. For a spacecraft with orbital radius R_{orb}, the baseline vector will be a certain angle away from the radius of the Earth. We will call this angle θ, which is given by

$$\theta = \cos^{-1}\left(\frac{R_E}{R_{\text{orb}}}\right). \tag{5.6}$$

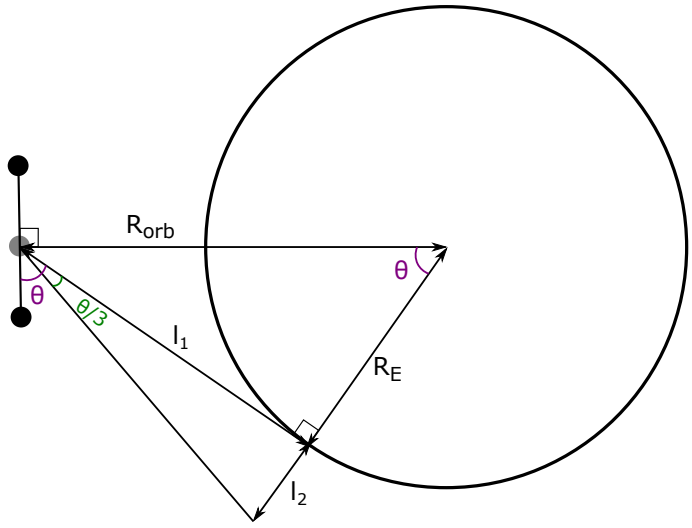

Figure 5.3: Extending the radius of the Earth due to optically scattered light.

We will try and baffle as much of the light that is being emitted in this angle, but we will suppose that the inner $\theta/3$ is too bright to fully block out. Hence the radius of the Earth is essentially extended by $\theta/3$. Calculating this extension in terms of linear distance:

$$\begin{aligned} l_1^2 &= R_{\text{orb}}^2 - R_E^2 \\ l_2 &= l_1 \tan\left(\frac{\theta}{3}\right) \\ \Rightarrow l_2 &= \sqrt{R_{\text{orb}}^2 - R_E^2}\,\tan\left(\frac{\cos^{-1}\left(\frac{R_E}{R_{\text{orb}}}\right)}{3}\right), \end{aligned} \tag{5.7}$$

and so the total effective radius of the Earth is

$$R_{\text{eff}} = R_E + \sqrt{R_{\text{orb}}^2 - R_E^2}\,\tan\left(\frac{\cos^{-1}\left(\frac{R_E}{R_{\text{orb}}}\right)}{3}\right). \tag{5.8}$$

The final test is hence

$$|\boldsymbol{r}_d - (\boldsymbol{r}_d \cdot \hat{\boldsymbol{s}})\hat{\boldsymbol{s}}| < R_{\text{eff}}. \tag{5.9}$$

For a 500 km orbit, the radius is extended by 333 m, leading to an effective equatorial radius of 6378.4 km.

5.2 Satellite sky coverage

With the separate observability criteria determined, the next step is to simulate a year's worth of orbits to identify what parts of the sky are visible for a set of given parameters and during what part of the year. We have a few parameters that we can modify to determine how extensive the sky coverage is for our mission. These include the antisolar angle γ, the chief orbit's parameters (i, Ω) and the radius of the orbit R_{orb}. Of these, the radius does not require much study: a larger orbital radius will reduce the amount of

time the Earth is blocking any stars. The other three parameters (γ, i, and Ω) are more complex and hence their parameter spaces need to be explored.

Another parameter that has not been discussed that must also be considered is integration time. It is fine to say that a target is viewable at any instantaneous moment in time. However, to take measurements we need to integrate the light from the star for an extended period of time without any obstruction. Thus we also need to factor in how long our spacecraft needs to view a star unobstructed. For our tests below, we assume this to be about 45 min - half an orbit at 500 km. This is approximately the maximum time we can expect to integrate for, as the other half of the orbit should be spent recharging the power (as we are in the daylight half of the orbit).

Lastly, the nodal precession of the orbit needs to be considered. The cause of the precession was discussed earlier, with the J_2 perturbation in section 3.2, but we need to explicitly mention this here as the precession may potentially allow us to view many more stars over the course of a year. The precession rate for a circular orbit is directly tied to the inclination of the orbit as we have seen before (recall Equation 3.10):

$$\frac{\mathrm{d}\Omega}{\mathrm{d}t} = -\sigma = -\left(\frac{3\omega J_2 R_E^2}{2R_{\text{orb}}^2}\right)\cos i, \tag{5.10}$$

where J_2 is the coefficient of the first zonal term of the Earth's gravitational field, μ is the gravitational parameter for the Earth and i is the inclination. We can also rearrange this to calculate the inclination required for a given precession rate:

$$i = \cos^{-1}\left(-\frac{2}{3}\frac{\frac{\mathrm{d}\Omega}{\mathrm{d}t}R_{\text{orb}}^2}{\omega J_2 R_E^2}\right). \tag{5.11}$$

To obtain a stable coverage over a year, we should put the satellite array in a heliosynchronous orbit - an orbit that precesses 360° over the course of a year. Substituting this into Equation 5.11 gives us a required chief inclination of $i = 97.37°$, which is a very common orbital configuration for Low Earth Orbit satellites. The other main inclination to consider is 39°. This is the lowest inclination that the rocket company Rocket Lab can achieve (Rocket Lab, 2019), therefore representing the inclination of the highest launch mass. As the Advanced Instrumentation and Tecnology Centre (AITC) where the satellite array will be assembled is close to New Zealand, this is the least expensive custom launch option. We therefore have two inclinations to consider. We also have two antisolar angles - the ambitious $\gamma = 60°$ discussed earlier and a more conservative $\gamma = 40°$.

To start investigating how changing these parameters affect what portion of the sky is observable, a colour plot of star declination (δ) against time was made (Fig. 5.4). The proportion of an orbit that a given declination is observable was plotted on the colour axis, where brighter areas represent a larger percentage of observability. This slice of declinations was plotted over the course of a year ($\sim$5500 orbits) and all other orbital parameters were varied, including inclination (i), orbital longitude (Ω), right ascension (α) and the antisolar angle (γ). An altitude of 500 km is assumed, as well as a maximum separation between the chief and deputy of $|\Delta \boldsymbol{r}_{\max}| = 300$ m.

In Fig. 5.4a and 5.4b, the antisolar angle was set to 180°. This means that the Sun will not be contributing to whether a star is observable, allowing us to see the effects of varying inclination more easily. All the plots, except when explicitly varied, have $\Omega = 90°$

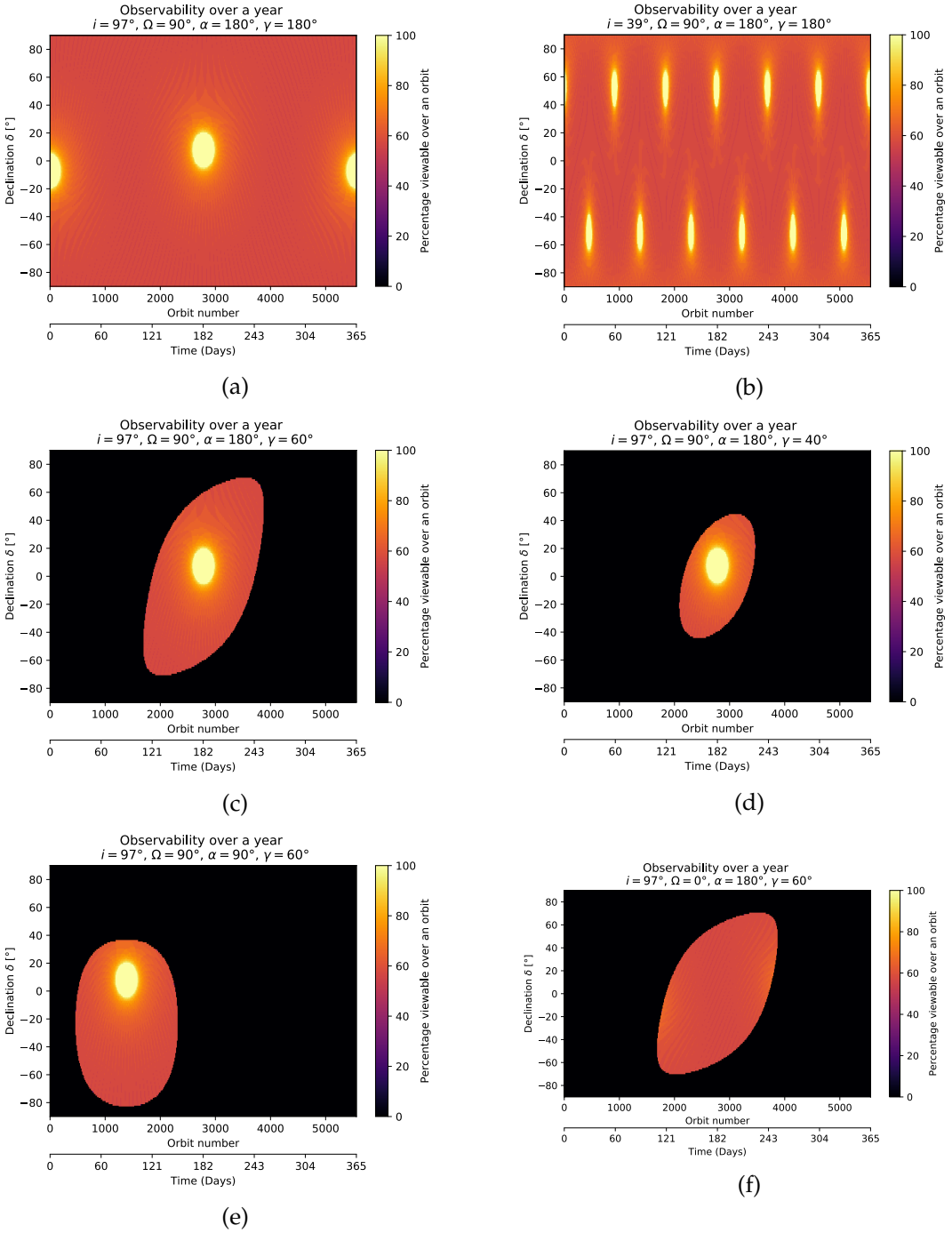

Figure 5.4: Satellite sky coverage of the satellite array, demonstrating the observability of a slice of declinations over the course of a year for different orbital parameters (see main text).

and $\alpha = 180°$. It is very apparent that inclination affects when certain portions of the sky are 100% viewable during an orbit, with a heliosynchronous orbit having larger 100% observable time periods but fewer in number than the 39° orbit. This makes sense when precession is considered - the heliosynchronous orbit will precess once per year, and so we see a single period of this precession in the plot. The 39° orbit on the other hand has a period six times larger, which is due to the $\cos(i)$ dependence on the precession rate. We see these six periods in the plot, showing that a flatter orbit will allow for more times when a given star is maximally viewable for the whole orbit, but the length of those periods will be shorter.

Another feature of interest is the height change of these spots of 100% observability, which can also be accounted for in the change in inclination. The stars which will be 100% observable will be perpendicular to the orbital plane of the orbit, as the Earth will not be blocking the light from the star. Hence for a heliosynchronous orbit, these stars will be at a declination of 7°, while the 39° orbit has these stars at 51°.

Fig. 5.4c is identical to Fig. 5.4a, except that the Sun has been added with an antisolar angle of $\gamma = 60°$. All of the following plots are based on the heliosynchronous orbit. We can see that adding the sun removes most of the observability for the sky, as we are restricted to a window of size $\propto \gamma^2$ deg^2. Making the angle even smaller (40° as in Fig. 5.4d), further decreases the window of observable stars. It is noticeable in this plot that this "window" of observable stars is on an angle. This angle is approximately 23°, highlighting that this tilt is due to the obliquity of the ecliptic. When the array is changed to look at a star with $\alpha = 90°$ (Fig. 5.4e), this obliquity disappears due to the fact that the window for which this star is maximally observable is during the Northern Hemisphere's summer solstice. At this time, Earth's tilt axis is facing away from the Sun, preventing any angular features from showing. It should be noted that changing the right ascension of the star changes both the window of observability with respect to the Sun, and also the spots of maximum observability due to the fact that the array must precess a different amount for the star to be perpendicular to the orbital plane.

Changing Ω in a heliosynchonous orbit changes the time of day at which the array passes over the equator. There are two special cases to examine here: a noon-midnight orbit (where the array passes over the equator during noon/midnight) and a dawn-dusk orbit (where the array passes the equator during dawn/dusk). A dawn-dusk orbit, where the array rides the Earth's terminator between day and night, is ideal for our array as it means we can always point the array towards the night side of the Earth at any point in the orbit. We see this difference in Fig. 5.4f, which shows a noon-midnight orbit compared to the dawn-dusk orbit in Fig. 5.4c. The dawn-dusk orbit allows us to see some stars 100% of the time (when the star is perpendicular to the orbit), but the noon-midnight orbit will not as the stars perpendicular to the orbit are outside the acceptable antisolar angle.

To see the averaged effect of changing these parameters over the course of a year, a few maps of the sky were created. These maps, shown in Fig. 5.5, demonstrate the average yearly observability for a grid of right ascension and declination. Fig. 5.5a and 5.5b compare the difference in inclination between the heliosynchronous and 39°orbit. As we can see, the general shape is the same, though the heliosynchronous orbit has a bright stripe centred on 7° and the 39° orbit has some patches around 51°. These represent the 100% observability patches found in Fig. 5.4. Changing Ω for the heliosynchonous orbit case in plot 5.5c removes this bright stripe, as the orbit no longer has periods where a given star is 100% observable. Interestingly, the heliosynchronous orbit plot indicates

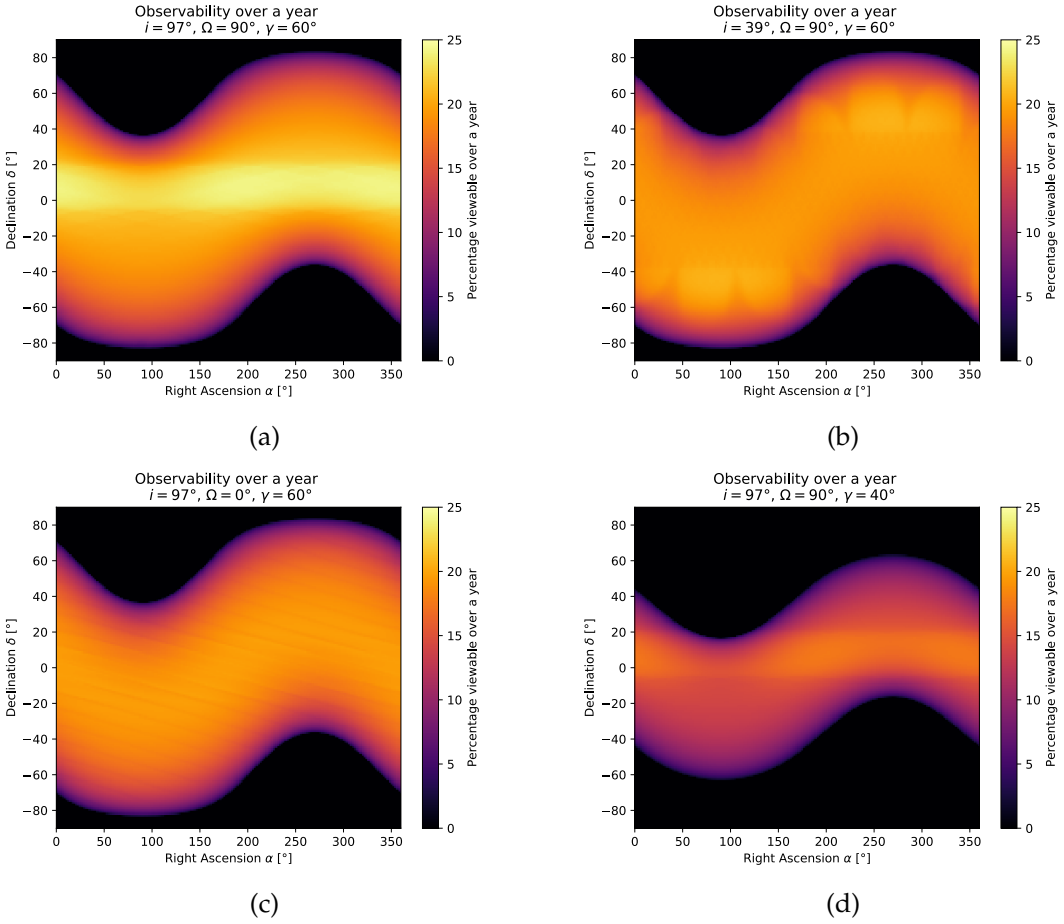

Figure 5.5: Map of the satellite sky coverage of different parts of the sky, as a percentage observable over a year. The orbital parameters are varied for each of the subfigures.

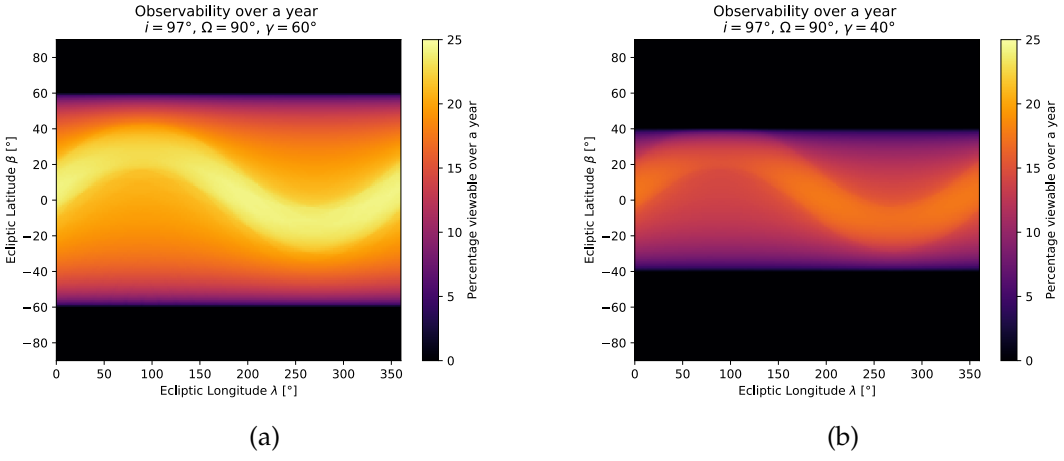

Figure 5.6: Map of the satellite sky coverage of different parts of the sky, as a percentage observable over a year, shown in ecliptic coordinates.

that the observability in the bright patch area is better over the course of a year than for the lower inclination orbit.

Finally, and most interesting of all, is the effect of lowering the antisolar angle in Fig. 5.5d. As expected, the locations where a star cannot be viewed at all increases due to the sun blocking more area. However, even in the observable areas the overall percentage of observability decreases. This is because the smaller window at a given time will lead to a lower percentage when averaged over a year. Ultimately, this tells us that the most critical component with regards to observability is the antisolar angle - we need to maximise this as much as possible through baffling the satellites and other means.

By transforming Fig. 5.5 from equatorial coordinates to ecliptic latitude and longitude (λ, β), we can see the constraints on where the scientific targets have to lie. These are shown in Fig. 5.6. Here, it is obvious that fundamentally the antisolar angle restricts the ecliptic latitude of the potential science targets. That is, for $\gamma = 60°$, the targets need to be within $\beta = \pm 60°$.

Even with the smaller antisolar angle, there are some very appealing targets that lie within 40° of the ecliptic (listed in Table 5.1), such as the ρ Ophiuchus and Taurus star forming regions that could be used to analyse stars in the process of formation. Other objects include the microquasar SS 433, a black hole of a few solar masses located inside a supernova remnant and exhibiting bright emission in the radio, optical and X-ray (Margon, 1984). 3C 273 is also a potential target, which was the first quasar ever discovered (Schmidt, 1963) and is the optically brightest in the sky. All of these have a magnitude of $V < 15$. In addition to these, there are likely many more targets for which a space interferometer, even one as small as this one, could provide critical scientific observations.

Table 5.1: List of potential interesting targets within 40° ecliptic latitude

Object Name	Ecliptic Longitude λ [°]	Ecliptic Latitude β [°]	V Magnitude	Description
SS 433	290	+27	13.0	Microquasar
3C 273	185	+05	14.8	Optically brightest quasar
Rho Ophiuchus	248	-02	–	Nearest star forming region
Taurus Molecular Cloud	72	+04	–	Nearest large star forming region

5.3 Filling the UV plane

As we are using an interferometer, observability is not the only criteria to consider when assessing the performance of the array. We also need to consider how much of the UV plane the interferometer covers. The UV plane spans the possible baseline lengths and position angles - the more of the plane that is sampled, the better the interferometer can function as an imager.

The UV plane is usually defined as perpendicular to the source, with unit vectors $\hat{\boldsymbol{u}}$ being the North-South component and $\hat{\boldsymbol{v}}$ being the East-West component. These can be easily calculated for a given star vector $\hat{\boldsymbol{s}}$ using

$$\hat{\boldsymbol{v}} = \hat{\boldsymbol{s}} \times \hat{\boldsymbol{z}} \qquad\qquad \hat{\boldsymbol{u}} = \hat{\boldsymbol{s}} \times \hat{\boldsymbol{v}}, \tag{5.12}$$

where $\hat{\boldsymbol{z}}$ is the North axis of the Earth. During the simulation of an orbit, the baseline vector at any given moment can be calculated by taking the difference of the two position

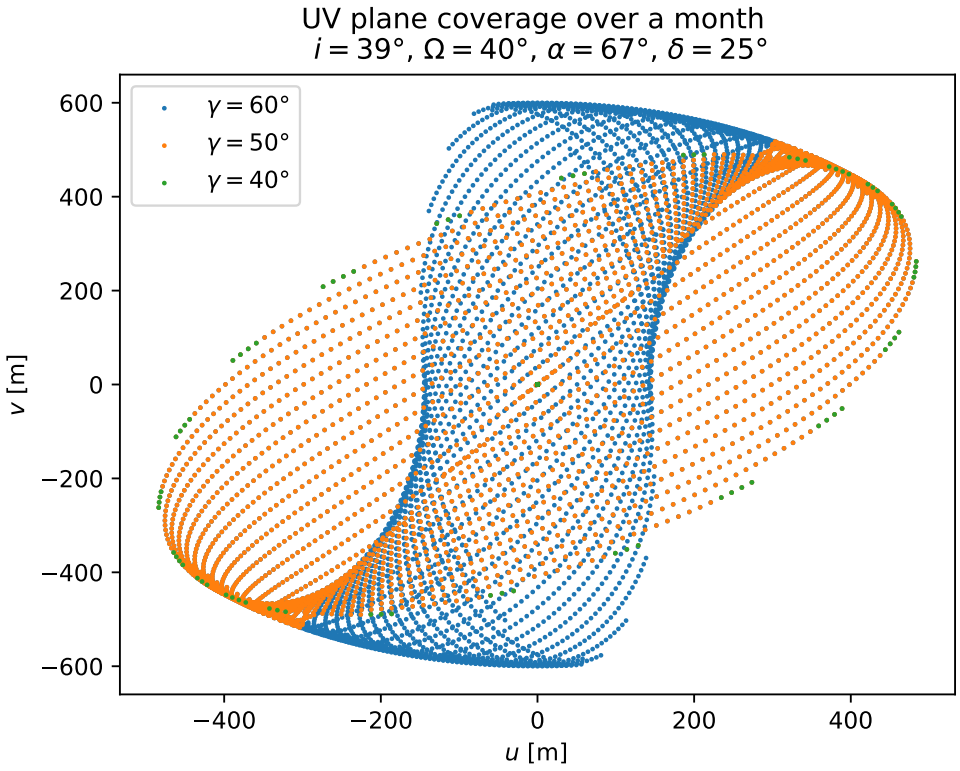

Figure 5.7: UV plane coverage over a month for the satellite array in a 39° orbit with $\Omega = 40°$, $\alpha = 67°$ and $\delta = 25°$. The antisolar angle was varied and plotted in different colours: $\gamma = 50$ also includes $\gamma = 40$ points, and $\gamma = 60$ includes the points from $\gamma = 40$ and $\gamma = 50$. The maximum baseline is $|\Delta \boldsymbol{b}_{\max}| = 600\,\mathrm{m}$.

vectors of the deputies:

$$\Delta \boldsymbol{b}(t) = \boldsymbol{r}_2(t) - \boldsymbol{r}_1(t). \tag{5.13}$$

Then, we can decompose this vector into its $\hat{\boldsymbol{u}}$ and $\hat{\boldsymbol{v}}$ components. The third component in the $\hat{\boldsymbol{s}}$ direction should be zero due to the definition of the orbit. Of course, this is not the case due to perturbations, but we will consider this in future simulations. Completing this gives a number of points on the UV plane with coordinates

$$\begin{aligned} u(t) &= \Delta \boldsymbol{b}(t) \cdot \hat{\boldsymbol{u}} \\ v(t) &= \Delta \boldsymbol{b}(t) \cdot \hat{\boldsymbol{v}}. \end{aligned} \tag{5.14}$$

Due to symmetry, we can also include the negative of this point $(-u(t), -v(t))$. Hence, for each baseline we can fill in two points on the UV plane.

Fig. 5.7 shows the UV coverage of an arbitrary star ($\alpha = 67°$, $\delta = 25°$) for the array in a 39° inclination and $\Omega = 40°$ orbit, over the course of a month from the vernal equinox. The maximum separation between the chief and deputy is $|\Delta \boldsymbol{r}_{\max}| = 300\,\mathrm{m}$, corresponding to a maximum baseline of $|\Delta \boldsymbol{b}_{\max}| = 600\,\mathrm{m}$. The antisolar angle was varied between 40 and 60° and is plotted in different colours.

The first thing of note is that this small interferometer has phenomenal UV coverage if the antisolar angle is large enough. The precession of the orbit, along with the fact

that the deputy spacecraft move with respect to each other constantly means that we can achieve a large variety of baseline lengths, along with position angles. As can also be seen, increasing the antisolar angle dramatically increases the UV coverage of the interferometer, and so again, this angle should be made as large as possible.

Chapter 6

Conclusion and Future Work

In order to analyse exoplanet formation and atmospheres, we require instruments with extremely high resolution and sensitivity; a level at which current instruments fall short. Seemingly, the only future types of instruments that will satisfy both of these requirements is an interferometer located in space, which brings a whole host of technical challenges. Missions from large organisations such as TPF-I from NASA and *Darwin* from ESA were cancelled, leaving a technological gap that has remained since the mid 2000s.

Throughout this thesis we have developed and tested the feasibility of a small scale space-interferometry mission, named the Astrophysical Space-interferometry Pathfinder (ASP), that aims to restart developments in the field of space interferometry. The design of this mission is ambitious: two 3U CubeSats that act as telescopes, and one 6U beam combiner CubeSat located between them. With such a space constraint, and to reduce cost, a single thruster for each satellite would be ideal. The main purpose of this thesis was to identify whether such a design would be feasible.

We attempted to modify a set of equations of motion that accounted for the J_2 perturbation (the oblateness of the Earth) in the local vertical, local horizontal (LVLH) frame, developed by Schweighart & Sedwick (2002). This was found to be fruitless as the sub-orbit motion was lost due to the averaging of the J_2 gradient over an orbit. Despite attempts to re-introduce this gradient, we were not able to effectively use the LVLH equations of motion. Hence, we simply integrated the equations of motion in the Earth-centred inertial (ECI) frame, dealing with the small numerical errors that are present with this approach.

We also briefly considered the effect of atmospheric drag, and calculated that it would cause a displacement along the baseline of the interferometer of 35 cm over the course of half an orbit. From the thruster constraint, this could be compensated by increasing the optical path along the star direction $\Delta s = \Delta \boldsymbol{r} \cdot \hat{\boldsymbol{s}}$ by 70 cm, equating to an angle of 0.1 °at a 600 m baseline. This angle should be small enough to correct with an actuator on the telescope mirror.

An orbital simulation showed that the Δv required to ensure the optical path difference D was kept at zero during integration was at most 5% of the overall Δv budget of 0.04 m/s. We also found that correcting for differential atmospheric drag only required a miniscule 0.3% of the budget. Then, we allowed the spacecraft array to thrust twice to correct for the residual J_2 perturbations over the second half of the orbit, which resulted in a Δv at most around 3%. Finally, we alternated correcting during integration and correcting the rest of the orbit to see whether the total Δv required would remain stable over multiple orbits. It was found that the Δv requirement did increase over multiple orbits, but only by less than 0.5% per orbit, and that this may have been due to numerical errors in the simulation. Changing the target of the interferometry was found to not

require a lot of Δv: a change of 2° in star position at 45° inclination requires about $\Delta v = 10\,\mathrm{mm/s}$; less than the budget of a single orbit. Ultimately, our configuration only required $\sim$10% of the available Δv budget per year; an encouraging result that shows that three thrusters should be enough to perform interferometry with a large amount of headroom.

The final part of the project was to investigate what targets are accessible for the satellite array for a given orbit. While the precession caused by the inclination of the orbit was shown to change at which times a target was viewable for a whole orbit, the most important parameter was found to be the antisolar angle: the maximum angle a star can make with the point directly opposite the sun. This parameter essentially sets the maximum ecliptic latitude for potential targets, and severely affects what proportion of a year a given target is observable. Nevertheless, even with a conservative antisolar angle of 40° we find that a large number of interesting targets are viewable, including the Taurus Molecular Cloud and the microquasar SS 433.

The interferometric UV plane was also simulated, and the array was found to cover a significant proportion of baseline lengths and position angles simply due to being in Low Earth Orbit. The coverage was shown to be tied to the antisolar angle as well, further increasing the need to push this parameter to be as large as possible.

Ultimately, this project has proven to have provided useful insight into the development of the ASP mission, specifically in regards to the feasibility of this ambitious design. The next stage will be to look at the detailed astrophysical science requirements, which will lead to the beam combiner requirements and the design of the baseline. We also need to conduct a full scale control simulation of the array, so that the exact amount of Δv required per orbit can be calculated, as well as revealing the optical path length residuals that we can expect during operation. Currently, this thesis only computed Δv for the largest perturbations, and it is likely that more thrust will be required from the control system as well as for smaller perturbations.

The control system philosophy also needs to be designed, based on both the light from an astrophysical source and the metrology subsystem; an issue which has not been discussed at length in this thesis. The metrology subsystem is the other critical component of the mission as it will define the accuracy with which we know the positions of each of the satellites in the array, which in turn determines the precision to which we can correct the optical paths. Together, the orbital dynamics, science requirements, control design and metrology subsystem can then be combined into a full systems model to perform an in-depth simulation of the array. Finally, constructing some of the components to be used on the spacecraft and performing physical tests on them will provide concrete evidence as to whether this mission can prove once and for all that space interferometry is a feasible technological concept.

If this mission is successful, we hope that this will kickstart the field of space inteferometry again. This would result in a revolution of high resolution astronomy, allowing for amazing science not just in the field of exoplanets, but also for other astronomy fields including compact objects and star formation. There are some truly exciting times ahead, and I hope that I will play a part in getting these techniques off the ground and into space.

Bibliography

Akiyama, K., Alberdi, A., Alef, W., et al. 2019, The Astrophysical Journal, 875, L1, doi: 10.3847/2041-8213/ab0ec7

Angel, J. R. P., Cheng, A. Y. S., & Woolf, N. J. 1986, Nature, 322, 341, doi: 10.1038/322341a0

Angel, J. R. P., & Woolf, N. J. 1997, The Astrophysical Journal, 475, 373, doi: 10.1086/303529

Beichman, C. A., Woolf, N. J., & Lindensmith, C. A. 1999, The Terrestrial Planet Finder (TPF) : a NASA Origins Program to search for habitable planets, Tech. rep., Jet Propulsion Laboratory, California Institute of Technology, Pasadena, California

Blackwood, G. H., Lay, O. P., Deininger, W. D., et al. 2003, in Interferometry in Space, ed. M. Shao, Vol. 4852 (International Society for Optics and Photonics), 463. http://proceedings.spiedigitallibrary.org/proceeding.aspx?doi=10.1117/12.460942

Blakely, R. J. 1995, in Potential Theory in Gravity and Magnetic Applications (Cambridge: Cambridge University Press), 100–127. https://www.cambridge.org/core/product/identifier/CBO9780511549816A038/type/book_part

Boyajian, T. S., McAlister, H. A., van Belle, G., et al. 2012, The Astrophysical Journal, Volume 746, Issue 1, article id. 101, 26 pp. (2012)., 746, doi: 10.1088/0004-637x/746/1/101

Bracewell, R. N. 1978, Nature, 274, 780, doi: 10.1038/274780a0

Buscher, D. F., & Longair, M. 2015, in Practical Optical Interferometry (Cambridge: Cambridge University Press), 1–35. https://www.cambridge.org/core/product/identifier/CBO9781107323933A010/type/book_part

CIRA Working Group. 2012, COSPAR International Reference Atmosphere - 2012, Tech. rep., COSPAR

Clohessy, W., & Wiltshire, R. 2012, Journal of the Aerospace Sciences, 27, 653, doi: 10.2514/8.8704

Cockell, C. S., Herbst, T., Léger, A., et al. 2009, Experimental Astronomy, 23, 435, doi: 10.1007/s10686-008-9121-x

Curtis, H. D. 2014, Orbital Mechanics for Engineering Students, 3rd edn. (Oxford: Elsevier Science and Technology)

Defrère, D., Absil, O., & Beichman, C. A. 2018, in Handbook of Exoplanets, ed. Hans J. Deeg & Juan Antonio Belmonte (Cham: Springer International Publishing), 1229–1255. http://link.springer.com/10.1007/978-3-319-55333-7_82

Dormand, J., & Prince, P. 1980, Journal of Computational and Applied Mathematics, 6, 19, doi: 10.1016/0771-050X(80)90013-3

Enpulsion Spacecraft Technology. 2018, IFM Nano Thruster, Enpulsion. https://www.enpulsion.com/wp-content/uploads/ENP2018-001.F-IFM-Nano-Thruster-Product-Overview.pdf

European Space Agency. 2003, Darwin's six telescopes. https://www.esa.int/spaceinimages/Images/2015/06/Darwin_s_six_telescopes

—. 2013, Second Lagrangian point (L2). http://www.planetary.org/multimedia/space-images/charts/l2-lagrangian-point.html

—. 2015, ESA Requirements on EOL De-orbit, Tech. rep., European Space Agency, Noordwijk

Fizeau, H. 1868, C. R. Acad. Sci., 932

Fridlund, C. 2002, Planetary and Space Science, 50, 101, doi: 10.1016/S0032-0633(01)00056-3

—. 2004, Symposium - International Astronomical Union, 202, 451, doi: 10.1017/S0074180900218470

Garland, G. D. G. D. 1979, Introduction to geophysics : mantle, core, and crust (Saunders), 494. https://books.google.com.au/books/about/Introduction_to_Geophysics.html?id=zWUSAQAAIAAJ&redir_esc=y

GRAVITY Collaboration. 2018, Nature, 563, 657, doi: 10.1038/s41586-018-0731-9

Haniff, C. 2007, New Astronomy Reviews, 51, 565, doi: 10.1016/j.newar.2007.06.002

Jones, E., Oliphant, T., Peterson, P., & ... 2001, SciPy: Open source scientific tools for Python. "http://www.scipy.org/"

Karlsson, A., & Kaltenegger, L. 2003, in Towards Other Earths: DARWIN/TPF and the Search for Extrasolar Terrestrial Planets, ed. M. Fridlund & T. Henning (Heidelberg, Germany: European Space Agency), 41–46. https://ui.adsabs.harvard.edu/abs/2003ESASP.539...41K/abstract

Kasting, J. F., Whitmire, D. P., & Reynolds, R. T. 1993, Icarus, 101, 108, doi: 10.1006/ICAR.1993.1010

Labeyrie, A. 1975, The Astrophysical Journal, 196, L71, doi: 10.1086/181747

Labeyrie, A., Authier, B., de Graauw, T., Kibblewhite, E., & Weigelt, G. 1985, in Kilometric Optical Arrays in Space, Vol. 226 (Cargese, Italy: European Space Agency), 27–33. https://ui.adsabs.harvard.edu/#abs/1985ESASP.226...27L/abstract

Labeyrie, A., Praderie, F., Steinberg, J., Vatoux, S., & Wouters, F. 1980, in Optical and Infrared Telescopes for the 1990's, ed. A. Hewitt (Tucson, USA: Kitt Peak National Observatory), 1020. https://ui.adsabs.harvard.edu/#abs/1980oits.conf.1020L/abstract

Labeyrie, A., Schneider, J., Boccaletti, A., et al. 2000, in Darwin and astronomy : the infrared space interferometer (Stockholm, Sweden: ESA Publications), 244. http://adsabs.harvard.edu/abs/2000ESASP.451...21L

Lacour, S., Nowak, M., Wang, J., et al. 2019, Astronomy & Astrophysics, 623, L11, doi: 10.1051/0004-6361/201935253

Lawson, P. 2000, Principles of Long Baseline Stellar Interferometry (JPL). https://ecommons.cornell.edu/handle/1813/41240

Le Duigou, J. M., Ollivier, M., Léger, A., et al. 2006, in Space Telescopes and Instrumentation I: Optical, Infrared, and Millimeter, 62651M, ed. J. C. Mather, H. A. MacEwen, & M. W. M. de Graauw, Vol. 6265 (Orlando, USA: International Society for Optics and Photonics), 62651M. http://proceedings.spiedigitallibrary.org/proceeding.aspx?doi=10.1117/12.671091

Léger, A., Fontecave, M., Labeyrie, A., et al. 2011, Astrobiology, 11, 335, doi: 10.1089/ast.2010.0516

Léger, A., Mariotti, J., Mennesson, B., et al. 1996, Icarus, 123, 249, doi: 10.1006/ICAR.1996.0155

Margon, B. 1984, Annual Review of Astronomy and Astrophysics, 22, 507, doi: 10.1146/annurev.aa.22.090184.002451

Martinache, F., & Ireland, M. J. 2018, Astronomy & Astrophysics, 619, A87, doi: 10.1051/0004-6361/201832847

Mayor, M., & Queloz, D. 1995, Nature, 378, 355, doi: 10.1038/378355a0

McCready, L., Pawsey, J. L., & Payne-Scott, R. 1947, Proceedings of the Royal Society of London. Series A. Mathematical and Physical Sciences, 190, 357, doi: 10.1098/rspa.1947.0081

Mennesson, B., & Mariotti, J. M. 1997, Icarus, 128, 202, doi: 10.1006/ICAR.1997.5731

Michelson, A. A., & Pease, F. G. 1921, The Astrophysical Journal, 53, 249, doi: 10.1086/142603

Moe, M. M., Wallace, S. D., & Moe, K. 2013, in The Upper Mesosphere and Lower Thermosphere: A Review of Experiment and Theory, Volume 87 (American Geophysical Union (AGU)), 349–356. http://doi.wiley.com/10.1029/GM087p0349

Monnier, J. D. 2003, Reports on Progress in Physics, 66, 789, doi: 10.1088/0034-4885/66/5/203

Monnier, J. D., Kraus, S., Ireland, M. J., et al. 2018, Experimental Astronomy, 46, 517, doi: 10.1007/s10686-018-9594-1

Montenbruck, O., & Gill, E. 2000, in Satellite Orbits (Berlin, Heidelberg: Springer Berlin Heidelberg), 53–116. http://link.springer.com/10.1007/978-3-642-58351-3_3

More, J. J., Garbow, B. S., & Hillstrom, K. E. 1980, User Guide for Minpack-1, Tech. rep., Argonne National Laboratory

National Aeronautics and Space Administration. 2019, LUVIOR final report, Tech. rep., NASA

National Research Council. 1997, Satellite Gravity and the Geosphere (Washington, D.C.: National Academies Press), doi: 10.17226/5767. http://www.nap.edu/catalog/5767

Noordam, J. E., Atherton, P. D., & Greenaway, A. H. 1985, in Kilometric Optical Arrays in Space, Vol. 226 (Cargese, Italy: European Space Agency), 63–69. https://ui.adsabs.harvard.edu/#abs/1985ESASP.226...63N/abstract

Ohnaka, K., Weigelt, G., & Hofmann, K.-H. 2017, Nature, 548, 310, doi: 10.1038/nature23445

Paladini, C., Baron, F., Jorissen, A., et al. 2018, Nature, 553, 310, doi: 10.1038/nature25001

Pettit, D. 2012, The Tyranny of the Rocket Equation, NASA. https://www.nasa.gov/mission_pages/station/expeditions/expedition30/tryanny.html

Quanz, S. P., Kammerer, J., Defrère, D., et al. 2018, in Optical and Infrared Interferometry and Imaging VI, ed. A. Mérand, M. J. Creech-Eakman, & P. G. Tuthill, Vol. 10701 (SPIE), 37. https://www.spiedigitallibrary.org/conference-proceedings-of-spie/10701/2312051/Exoplanet-science-with-a-space-based-mid-infrared-nulling-interferometer/10.1117/12.2312051.full

Quanz, S. P., Absil, O., Angerhausen, D., et al. 2019

Rocket Lab. 2019, Payload User's Guide, Tech. rep., Rocket Lab

Roettenbacher, R. M., Monnier, J. D., Korhonen, H., et al. 2016, Nature, 533, 217, doi: 10.1038/nature17444

Rousselet-Perraut, K., Benisty, M., Mourard, D., et al. 2010, Astronomy and Astrophysics, 516, L1, doi: 10.1051/0004-6361/201014720

Sagan, C., Thompson, W. R., Carlson, R., Gurnett, D., & Hord, C. 1993, Nature, 365, 715, doi: 10.1038/365715a0

Schmidt, M. 1963, Nature, 197, 1040, doi: 10.1038/1971040a0

Schweighart, S. A., & Sedwick, R. J. 2002, Journal of Guidance, Control, and Dynamics, 25, 1073, doi: 10.2514/2.4986

Seidelmann, P. K., United States Naval Observatory. Nautical Almanac Office., & Great Britain. Nautical Almanac Office. 1992, Explanatory supplement to the Astronomical almanac (University Science Books), 752. http://adsabs.harvard.edu/abs/1992esta.book.....S

Shao, M. 1998, in Astronomical Interferometry, ed. R. D. Reasenberg, Vol. 3350 (International Society for Optics and Photonics). http://proceedings.spiedigitallibrary.org/proceeding.aspx?doi=10.1117/12.317092

Stachnik, R. V., & Gezari, D. Y. 1985, in Kilometric Optical Arrays in Space, Vol. 226 (Cargese, Italy: European Space Agency), 35–42. https://ui.adsabs.harvard.edu/#abs/1985ESASP.226...35S/abstract

Stachnik, R. V., Melroy, P., McCormack, E. F., Arnold, D., & Gezari, D. Y. 1984, in Instrumentation in Astronomy V, ed. A. Boksenberg & D. L. Crawford, Vol. 0445 (London, United Kingdom: International Society for Optics and Photonics), 358–369. http://proceedings.spiedigitallibrary.org/proceeding.aspx?articleid=1236660

Traub, W. A., & Carleton, N. P. 1985, in Kilometric Optical Arrays in Space, Vol. 226 (Cargese, Italy: European Space Agency), 43–48. https://ui.adsabs.harvard.edu/#abs/1985ESASP.226...43T/abstract

van Cittert, P. 1934, Physica, 1, 201, doi: 10.1016/S0031-8914(34)90026-4

Zernike, F. 1938, Physica, 5, 785, doi: 10.1016/S0031-8914(38)80203-2

Zotter, F. 2008, Spherical Harmonics Symmetries. https://iaem.at/ambisonics/xchange/fileformat/docs/spherical-harmonics-symmetries

Appendix

A.1 Quaternions

Quaternions are an extension of the complex number system and are useful for performing rotations. A quaternion is a number of the form

$$\boldsymbol{q} = a + b\boldsymbol{i} + c\boldsymbol{j} + d\boldsymbol{k}, \tag{A.1}$$

where $\boldsymbol{i}, \boldsymbol{j}, \boldsymbol{k}$ are the "fundamental quaternion units". Here, a is denoted the real part and $[b, c, d]$ is denoted the vector part of $\boldsymbol{q}$.

A quaternion can represent a rotation through so called "axis-angle" representation. Given an angle θ and an axis $\hat{\boldsymbol{u}} = [u_x, u_y, u_z]$, the respective quaternion is

$$\boldsymbol{q}(\hat{\boldsymbol{u}}, \theta) = \cos\frac{\theta}{2} + \sin\frac{\theta}{2}(u_x\boldsymbol{i} + u_y\boldsymbol{j} + u_z\boldsymbol{k}), \tag{A.2}$$

where the default rotation is in the counter-clockwise direction. Note that the quaternion must be normalised for a rotation. The norm of a quaternion, using the generic quaternion in equation A.1, is $|\boldsymbol{q}| = \sqrt{a^2 + b^2 + c^2 + d^2}$. The normalised quaternion is then simply $\hat{\boldsymbol{q}} = \frac{\boldsymbol{q}}{|\boldsymbol{q}|}$.

The multiplication of two quaternions (as above) is given by the Hamilton product. Consider two quaternions $\boldsymbol{q}_1, \boldsymbol{q}_2$ with real parts a_1, a_2 and vector parts $\boldsymbol{u}_1 = [b_1, c_1, d_1], \boldsymbol{u}_2 = [b_2, c_2, d_2]$ respectively. The result of the Hamilton product ($\boldsymbol{q}_3$ with real part a_3 and vector part $\boldsymbol{u}_3 = [b_3, c_3, d_3]$) is given by

$$\begin{aligned} a_3 &= a_1a_2 - \boldsymbol{u}_1 \cdot \boldsymbol{u}_2 \\ \boldsymbol{u}_3 &= a_1\boldsymbol{u}_2 + a_2\boldsymbol{u}_1 + \boldsymbol{u}_1 \times \boldsymbol{u}_2. \end{aligned} \tag{A.3}$$

Two rotations, represented as two quaternions, can be combined into one quaternion using the Hamilton product. Consider a rotation comprised of first undergoing $\boldsymbol{q}_1$ and then $\boldsymbol{q}_2$. The combined rotation is simply

$$\boldsymbol{q} = \boldsymbol{q}_2\boldsymbol{q}_1. \tag{A.4}$$

To apply a rotation (represented by $\boldsymbol{q}$) to an arbitrary vector, $\boldsymbol{u}$, the vector must first be represented as a quaternion with real part equal to zero as follows:

$$\boldsymbol{p} = u_x\boldsymbol{i} + u_y\boldsymbol{j} + u_z\boldsymbol{k}. \tag{A.5}$$

The rotated vector is then the vector component of the following function:

$$\boldsymbol{Q}(\boldsymbol{u}, \boldsymbol{q}) = \boldsymbol{q}\boldsymbol{p}\boldsymbol{q}^{-1}, \tag{A.6}$$

where $\boldsymbol{q}^{-1}$ is the inverse quaternion, which for a unit quaternion is defined by

$$\boldsymbol{q}^{-1} = a - b\boldsymbol{i} - c\boldsymbol{j} - d\boldsymbol{k}. \tag{A.7}$$

The inverse quaternion is equivalent to performing a rotation in the other direction (clockwise).

A.2 The geopotential model

The non-sphericity of the Earth contributes significantly to orbital perturbations, in particular the J_2 zonal term. A short derivation of this perturbing force follows.

The gravitational field is a conservative vector field, with field potential U. Outside the Earth, Laplace's equation holds:

$$\nabla^2 U = 0. \tag{A.8}$$

In spherical coordinates, given by

$$\begin{aligned} x &= r\sin\theta\cos\phi \\ y &= r\sin\theta\sin\phi \\ z &= r\cos\theta, \end{aligned} \tag{A.9}$$

Laplace's equation transforms into

$$\frac{1}{r^2}\frac{\partial}{\partial r}\left(r^2\frac{\partial U}{\partial r}\right) + \frac{1}{r^2\sin\theta}\frac{\partial}{\partial\theta}\left(\sin\theta\frac{\partial U}{\partial\theta}\right) + \frac{1}{r^2\sin^2\phi}\frac{\partial^2 U}{\partial\phi^2} = 0. \tag{A.10}$$

The solutions to this equation are of the form of spherical harmonics (Garland, 1979):

$$U = \frac{1}{r^{1+n}}P_n^m(\cos\theta)[A_n^m\cos m\phi + B_n^m\sin m\phi], \tag{A.11}$$

where $P_n^m(\cos\theta)$ are the associated Legendre polynomials, given for $m \leq n$ by

$$P_n^m(\cos\theta) = \frac{(1-\cos^2\theta)^{m/2}}{2^n n!}\frac{\mathrm{d}^{n+m}(\cos^2\theta - 1)^n}{\mathrm{d}(\cos\theta)^{n+m}}. \tag{A.12}$$

Spherical harmonics form an orthonormal basis, and hence the full solution is a sum over all m and n (known as the order and degree of the polynomials) (Blakely, 1995):

$$\begin{aligned} U &= \sum_{n=0}^{\infty}\sum_{m=0}^{n}\left[\frac{1}{r^{1+n}}P_n^m(\cos\theta)[A_n^m\cos m\phi + B_n^m\sin m\phi]\right] \\ &= \frac{1}{r}\sum_{n=0}^{\infty}\left[A_n^0\frac{1}{r^n}P_n^0(\cos\theta) + \sum_{m=0}^{n}\frac{1}{r^n}P_n^m(\cos\theta)[A_n^m\cos m\phi + B_n^m\sin m\phi]\right]. \end{aligned} \tag{A.13}$$

Now, we know that the monopole term ($n = 0$) must give the spherically symmetric potential, and so

$$A_0^0 = -\mu. \tag{A.14}$$

Furthermore, the dipole terms ($n = 1$) can vanish by choosing the origin at the centre of the Earth (National Research Council, 1997), and so the potential becomes

$$U = \frac{1}{r}\left[-\mu + \sum_{n=2}^{\infty}A_n^0\frac{1}{r^n}P_n^0(\cos\theta) + \sum_{n=2}^{\infty}\sum_{m=0}^{n}\frac{1}{r^n}P_n^m(\cos\theta)[A_n^m\cos m\phi + B_n^m\sin m\phi]\right]. \tag{A.15}$$

Finally, we will transform into dimensionless coefficients by multiplying by $-1/\mu R_E^n$,

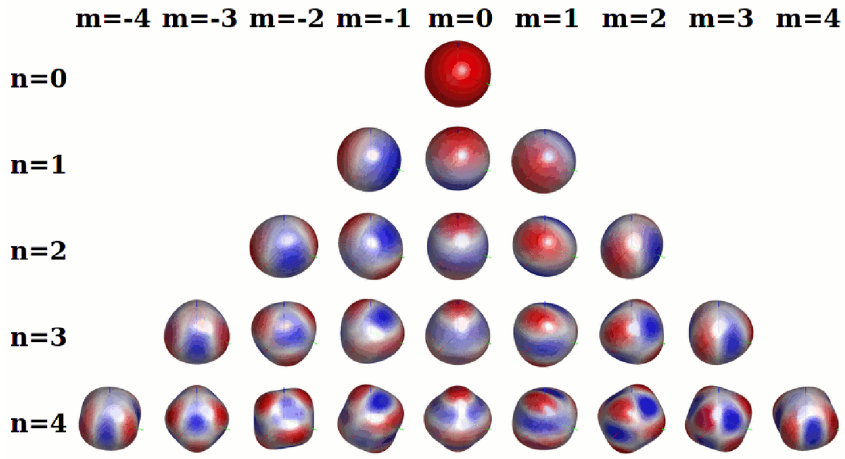

Figure A.1: Spherical harmonics of different orders (m) and degrees (n). Figure taken from Zotter (2008)

Table A.1: Low order geopotential coefficients. Note that $J_n = C_n^0$. Table taken from Montenbruck & Gill (2000)

C_n^m	$m=0$	1	2	3
$n=0$	+1.00			
1	0.00	0.00		
2	-1.08×10^{-3}	0.00	$+1.57 \times 10^{-6}$	
3	$+2.53 \times 10^{-6}$	$+2.18 \times 10^{-6}$	$+3.11 \times 10^{-7}$	$+1.02 \times 10^{-7}$
S_n^m	$m=0$	1	2	3
$n=0$	0.00			
1	0.00	0.00		
2	0.00	0.00	-9.03×10^{-7}	
3	0.00	$+2.68 \times 10^{-7}$	-2.12×10^{-7}	$+1.98 \times 10^{-7}$

where R_E is the equatorial radius of the Earth:

$$J_n = -\frac{A_n^0}{\mu R_E^n} \qquad C_n^m = -\frac{A_n^m}{\mu R_E^n} \qquad S_n^m = -\frac{B_n^m}{\mu R_E^n}, \tag{A.16}$$

and so

$$U = -\frac{\mu}{r}\left[1 + \sum_{n=2}^{\infty} J_n \left(\frac{R_E}{r}\right)^n P_n^0(\cos\theta) + \sum_{n=2}^{\infty}\sum_{m=0}^{n} \left(\frac{R_E}{r}\right)^n P_n^m(\cos\theta)[C_n^m \cos m\phi + S_n^m \sin m\phi]\right]. \tag{A.17}$$

The terms with coefficients J_n are known as "zonal" terms, as that part of the potential does not depend on the longitude. If $n = m$, then the C_n^m and S_n^m terms do not change sign with latitude - this means that the sphere is divided into "sectors" bounded by meridians of longitude (Montenbruck & Gill, 2000). Hence these terms are known as sectoral harmonics. All other terms divide the sphere into regions known as "tesserae" and so are known as tesseral harmonics. The larger the value of n and m, the smaller the size of these regions. A variety of harmonics are shown in Fig. A.1 to illustrate the difference between these terms.

A table of the low order and degree geopotential coefficients is shown in Table A.1. Here, we can see that the J_2 zonal term is the most important by several orders of magnitude, and represents the Earth's oblateness term. Truncating the series at this point yields

$$\begin{aligned} U &= -\frac{\mu}{r}\left[1 + J_2\left(\frac{R_E}{r}\right)^2 P_2^0(\cos\theta)\right] \\ &= -\frac{\mu}{r}\left[1 + J_2\frac{R_E^2}{2r^2}(3\cos^2\theta - 1)\right]. \end{aligned} \tag{A.18}$$

The J_2 potential term is hence

$$U_{J_2} = -J_2\frac{\mu R_E^2}{2r^3}(3\cos^2\theta - 1). \tag{A.19}$$

Converting into cartesian coordinates:

$$\begin{aligned} U_{J_2} &= -J_2\frac{\mu R_E^2}{2r^3}\left(3\frac{z^2}{r^2} - 1\right) \\ &= -J_2\frac{\mu R_E^2}{2}\left(3\frac{z^2}{r^5} - \frac{1}{r^3}\right) \\ &= -J_2\frac{\mu R_E^2}{2}\left(\frac{3z^2}{(x^2+y^2+z^2)^{\frac{5}{2}}} - \frac{1}{(x^2+y^2+z^2)^{\frac{3}{2}}}\right). \end{aligned} \tag{A.20}$$

The force is the negative gradient of the potential, and so

$$\begin{aligned} F_{J_2,x} = -\frac{\partial U_{J_2}}{\partial x} &= J_2\frac{\mu R_E^2}{2}\left(-\frac{5}{2}\frac{3z^2}{(x^2+y^2+z^2)^{\frac{7}{2}}}\cdot 2x + \frac{3}{2}\frac{1}{(x^2+y^2+z^2)^{\frac{5}{2}}}\cdot 2x\right) \\ &= J_2\frac{\mu R_E^2}{2}\left(-\frac{15xz^2}{r^7} + \frac{3x}{r^5}\right) \\ &= J_2\frac{3\mu R_E^2 x}{2r^5}\left(1 - 5\frac{z^2}{r^2}\right) \end{aligned} \tag{A.21}$$

$$F_{J_2,y} = -\frac{\partial U_{J_2}}{\partial y} = J_2\frac{3\mu R_E^2 y}{2r^5}\left(1 - 5\frac{z^2}{r^2}\right) \tag{A.22}$$

$$\begin{aligned} F_{J_2,z} = -\frac{\partial U_{J_2}}{\partial z} &= J_2\frac{\mu R_E^2}{2}\left(-\frac{5}{2}\frac{3z^2}{(x^2+y^2+z^2)^{\frac{7}{2}}}\cdot 2z + \frac{6z}{(x^2+y^2+z^2)^{\frac{5}{2}}} + \frac{3}{2}\frac{1}{(x^2+y^2+z^2)^{\frac{5}{2}}}\cdot 2z\right) \\ &= J_2\frac{\mu R_E^2}{2}\left(-\frac{15z^3}{r^7} + \frac{9z}{r^5}\right) \\ &= J_2\frac{3\mu R_E^2 z}{2r^5}\left(3 - 5\frac{z^2}{r^2}\right). \end{aligned} \tag{A.23}$$

Hence, the force vector due to J_2 is equal to

$$\boldsymbol{F}_{J_2} = J_2\frac{3\mu R_E^2}{2r^5}\left[\left(1 - 5\frac{z^2}{r^2}\right)(x\hat{\mathbf{x}} + y\hat{\mathbf{y}}) + \left(3 - 5\frac{z^2}{r^2}\right)z\hat{\mathbf{z}}\right]. \tag{A.24}$$

A.3 Derivation of the J2 LVLH equations of motion

We will derive the equations of motion for a satellite influenced by the J_2 oblateness perturbation with respect to a circular reference orbit in the local vertical, local horizontal (LVLH) frame. For the first half of the derivation, see Schweighart & Sedwick (2002).

In the absence of perturbations, the reference orbit is rotating with an angular velocity given by

$$\begin{aligned} \boldsymbol{\omega} &= \omega \hat{\boldsymbol{\eta}} \\ \omega &= \sqrt{\frac{\mu}{R_{\text{orb}}^3}}. \end{aligned} \tag{A.25}$$

Through averaging the angular velocity over the J_2 perturbation, we have that the velocity must be adjusted by a factor c, given by

$$\begin{aligned} c &= \sqrt{1+s} \\ s &= \frac{3J_2R_E^2}{8R_{\text{orb}}^2}(1+3\cos 2i) \\ \boldsymbol{\omega} &= \omega c \hat{\boldsymbol{\eta}}. \end{aligned} \tag{A.26}$$

The main long term effect of J_2 is nodal precession, where the longitude of the ascending node Ω drifts over time. Hence we must correct this through adjusting the reference orbit. The position of the reference orbit at a time t in the Earth-centred inertial (ECI) frame is given by

$$\begin{aligned} \boldsymbol{r}_{\text{ref}} = R_{\text{orb}}([&\cos\Omega(t)\cos\theta(t) - \sin\Omega(t)\sin\theta(t)\cos i(t)]\hat{\boldsymbol{x}} \\ &+[\sin\Omega(t)\cos\theta(t) - \cos\Omega(t)\sin\theta(t)\cos i(t)]\hat{\boldsymbol{y}} \\ &+[\sin\theta(t)\sin i(t)]\hat{\boldsymbol{z}}), \end{aligned} \tag{A.27}$$

where

$$\begin{aligned} i(t) &= i_{\text{ref}} - \frac{\sigma}{k}\sin i_{\text{ref}} & \sigma &= \left(\frac{3\omega J_2 R_E^2}{2R_{\text{orb}}^2}\right)\cos i_{\text{ref}} \\ \Omega(t) &= \Omega_0 - \sigma t & k &= \omega c + \sigma \cos i_{\text{ref}} \\ \theta(t) &= kt. \end{aligned} \tag{A.28}$$

The velocity of the reference orbit is found by taking the derivative:

$$\begin{aligned} \dot{\boldsymbol{r}}_{\text{ref}} = R_{\text{orb}}([&-\sin\Omega(t)\cos\theta(t)\dot{\Omega}(t) - \cos\Omega(t)\sin\theta(t)\dot{\theta}(t) - \\ &\cos\Omega(t)\sin\theta(t)\cos i(t)\dot{\Omega}(t) - \sin\Omega(t)\cos\theta(t)\cos i(t)\dot{\theta}(t)]\hat{\boldsymbol{x}} \\ &+[\cos\Omega(t)\cos\theta(t)\dot{\Omega}(t) - \sin\Omega(t)\sin\theta(t)\dot{\theta}(t) - \\ &\sin\Omega(t)\sin\theta(t)\cos i(t)\dot{\Omega}(t) + \cos\Omega(t)\cos\theta(t)\cos i(t)\dot{\theta}(t)]\hat{\boldsymbol{y}} \\ &+[\cos\theta(t)\sin i(t)\dot{\theta}(t)]\hat{\boldsymbol{z}}), \end{aligned} \tag{A.29}$$

where

$$\begin{aligned}\dot{\Omega}(t) &= -\sigma \\ \dot{\theta}(t) &= k.\end{aligned} \tag{A.30}$$

The base equations of motion for a satellite in the LVLH frame is the Hill-Clohessy-Wiltshire (HCW) equations (Equation 3.1). Adding the J_2 potential and counteracting the adjustments to the reference orbit given above produces a set of differential equations,

$$\begin{aligned}\ddot{\rho} &= 2\omega c\dot{\xi} + (5c^2 - 2)\omega^2\rho - 3\omega^2 J_2 \frac{R_E^2}{R_{\text{orb}}}\left[\frac{1}{2} - \frac{3\sin^2 i_{\text{ref}} \sin^2 kt}{2} - \frac{1 + 3\cos 2i_{\text{ref}}}{8}\right] \\ \ddot{\xi} &= -2\omega c\dot{\rho} - 3\omega^2 J_2 \frac{R_E^2}{R_{\text{orb}}} \sin^2 i_{\text{ref}} \sin kt \cos kt \\ \ddot{\eta} &= -(3c^2 - 2)\omega^2\eta.\end{aligned} \tag{A.31}$$

Finally, Schweighart & Sedwick (2002) corrected the cross-track motion of the satellites (η direction). The parameters for this correction as defined by Schweighart & Sedwick (2002) are as follows:

$$\begin{aligned}i_{\text{sat}} &= \frac{\dot{\eta_0}}{kR_{\text{orb}}} + i_{\text{ref}} \\ \Delta\Omega_0 &= \frac{\eta_0}{R_{\text{orb}} \sin i_{\text{ref}}} \\ \gamma_0 &= \cot^{-1}\left[\frac{\cot i_{\text{ref}} \sin i_{\text{sat}} - \cos i_{\text{sat}} \cos \Delta\Omega_0}{\sin \Delta\Omega_0}\right] \\ \Phi_0 &= \arccos(\cos i_{\text{sat}} \cos i_{\text{ref}} + \sin i_{\text{sat}} \sin i_{\text{ref}} \cos \Delta\Omega_0) \\ \Delta\dot{\Omega}_{\text{sat}} &= -\frac{3\omega J_2 R_E^2}{2R_{orb}^2} \cos i_{\text{sat}} \\ \Delta\dot{\Omega}_{\text{ref}} &= -\frac{3\omega J_2 R_E^2}{2R_{orb}^2} \cos i_{\text{ref}} \\ q &= \omega c - (\cos\gamma_0 \sin\gamma_0 \cot \Delta\Omega_0 - \sin^2\gamma_0 \cos i_{\text{sat}})(\Delta\dot{\Omega}_{\text{sat}} - \Delta\dot{\Omega}_{\text{ref}}) \\ &\quad - \Delta\dot{\Omega}_{\text{sat}} \cos i_{\text{sat}} \\ l &= -R_{\text{orb}} \frac{\sin i_{\text{sat}} \sin i_{\text{ref}} \sin \Delta\Omega_0}{\sin \Phi_0}(\Delta\dot{\Omega}_{\text{sat}} - \Delta\dot{\Omega}_{\text{ref}}).\end{aligned} \tag{A.32}$$

Using the above, the two equations below must be solved simultaneously to find m and ϕ:

$$\begin{aligned}m\sin(\phi) &= \eta_0 \\ l\sin(\phi) + qm\cos(\phi) &= \dot{\eta_0}.\end{aligned} \tag{A.33}$$

The cross-track motion is then described by the differential equation

$$\ddot{\eta} = -q^2\eta + 2lq\cos(qt + \phi). \tag{A.34}$$

Putting it all together gives us the final set of three coupled differential equations,

$$\begin{aligned}
\ddot{\rho} &= 2\omega c\dot{\xi} + (5c^2-2)\omega^2\rho - 3\omega^2 J_2 \frac{R_E^2}{R_{\text{orb}}}\left[\frac{1}{2} - \frac{3\sin^2 i_{\text{ref}}\sin^2 kt}{2} - \frac{1+3\cos 2i_{\text{ref}}}{8}\right] \\
\ddot{\xi} &= -2\omega c\dot{\rho} - 3\omega^2 J_2 \frac{R_E^2}{R_{\text{orb}}}\sin^2 i_{\text{ref}}\sin kt\cos kt \\
\ddot{\eta} &= -q^2\eta + 2lq\cos(qt+\phi),
\end{aligned} \tag{A.35}$$

which can be simplified a bit through trigonometric identities:

$$\begin{aligned}
\ddot{\rho} &= 2\omega c\dot{\xi} + (5c^2-2)\omega^2\rho - 3\omega^2 J_2 \frac{R_E^2}{R_{\text{orb}}}\frac{3\cos 2kt\sin^2 i_{\text{ref}}}{4} \\
\ddot{\xi} &= -2\omega c\dot{\rho} - 3\omega^2 J_2 \frac{R_E^2}{R_{\text{orb}}}\sin^2 i_{\text{ref}}\sin kt\cos kt \\
\ddot{\eta} &= -q^2\eta + 2lq\cos(qt+\phi).
\end{aligned} \tag{A.36}$$

The given solutions by Schweighart & Sedwick (2002) assume certain initial conditions for $t = 0$. To generalise the equations, a set of solutions for arbitrary initial conditions at $t = t_0$ were created, requiring the following coefficients.

$$\begin{aligned}
\alpha &= \omega\sqrt{1-s} \\
\beta &= \frac{2c}{\sqrt{1-s}} \\
\gamma &= \beta^2 - 1 \quad [-] \\
\delta &= \frac{\alpha}{k} = \frac{\omega\sqrt{1-s}}{k} \\
\zeta &= \frac{3\omega^2 J_2 R_E^2}{4\delta(\alpha^2-4k^2)R_{\text{orb}}}\sin^2(i_{\text{ref}})
\end{aligned} \tag{A.37}$$

$$\begin{aligned}
\kappa_1 &= \beta^2\rho_0 + \frac{\beta}{\alpha}\dot{\xi}_0 - \beta\zeta(\delta^2-4)\cos(2kt_0) \\
\kappa_2 &= \xi_0 - \frac{\beta}{\alpha}\dot{\rho}_0 + \frac{1}{2}\zeta(\delta^2-4)(\gamma\delta-3\beta)\sin(2kt_0) \\
\kappa_3 &= -\gamma\rho_0 - \frac{\beta}{\alpha}\dot{\xi}_0 - \zeta(4\beta-3\delta)\cos(2kt_0) \\
\kappa_4 &= \frac{1}{\alpha}\dot{\rho}_0 + 2\zeta(\beta\delta-3)\sin(2kt_0) \\
\kappa_5 &= \zeta(\beta\delta^2-3\delta) \\
\kappa_6 &= \frac{\zeta\delta}{2}(3\beta\delta-\gamma\delta^2-4) \\
\kappa_7 &= \eta_0 \\
\kappa_8 &= \frac{\dot{\eta}_0 - l\sin(qt_0+\phi)}{q}.
\end{aligned} \tag{A.38}$$

The final equations for position are then

$$\begin{aligned}
\rho(t) &= \kappa_1 + \kappa_3 \cos(\alpha(t-t_0)) + \kappa_4 \sin(\alpha(t-t_0))) + \kappa_5 \cos(2kt) \\
\xi(t) &= \kappa_2 - \frac{\alpha\gamma}{\beta}\kappa_1(t-t_0) + \beta\kappa_4 \cos(\alpha(t-t_0)) - \beta\kappa_3 \sin(\alpha(t-t_0)) + \kappa_6 \sin(2kt) \\
\eta(t) &= \kappa_7 \cos(q(t-t_0)) + l(t-t_0)\sin(qt+\phi) + \kappa_8 \sin(q(t-t_0)).
\end{aligned} \tag{A.39}$$

We can substitute κ_3 and κ_4 for a trigonometric function to simplify the motion further, as was done in section 2.2. Setting

$$\begin{aligned}
\kappa_3 &= A_1 \cos\varphi_1 & \kappa_4 &= A_1 \sin\varphi_1 \\
\kappa_7 &= A_2 \cos\varphi_2 & \kappa_8 &= A_2 \sin\varphi_2,
\end{aligned} \tag{A.40}$$

we then have

$$\begin{aligned}
\rho(t) &= \kappa_1 + A_1 \cos\varphi_1 \cos(\alpha(t-t_0)) + A_1 \sin\varphi_1 \sin(\alpha(t-t_0))) + \kappa_5 \cos(2kt) \\
\xi(t) &= \kappa_2 - \frac{\alpha\gamma}{\beta}\kappa_1(t-t_0) + \beta A_1 \sin\varphi_1 \cos(\alpha(t-t_0)) - \beta A_1 \cos\varphi_1 \sin(\alpha(t-t_0)) + \kappa_6 \sin(2kt) \\
\eta(t) &= A_2 \cos\varphi_2 \cos(q(t-t_0)) + l(t-t_0)\sin(qt+\phi) + A_2 \sin\varphi_2 \sin(q(t-t_0)),
\end{aligned} \tag{A.41}$$

which becomes

$$\begin{aligned}
\rho(t) &= \kappa_1 + A_1 \cos(\alpha(t-t_0) - \varphi_1) + \kappa_5 \cos(2kt) \\
\xi(t) &= \kappa_2 - \frac{\alpha\gamma}{\beta}\kappa_1(t-t_0) - \beta A_1 \sin(\alpha(t-t_0) - \varphi_1) + \kappa_6 \sin(2kt) \\
\eta(t) &= A_2 \cos(q(t-t_0) - \varphi_2) + l(t-t_0)\sin(qt+\phi).
\end{aligned} \tag{A.42}$$

To check if these equations are the same as the solutions given in Schweighart & Sedwick (2002), we can substitute in their given initial velocity conditions for $t_0 = 0$:

$$\begin{aligned}
\dot{\xi}_0 &= -2\rho_0\omega c + \frac{3J_2 R_E^2 \omega^2}{4kR_{\text{orb}}} \sin^2(i_{\text{ref}}) \\
&= -\alpha\beta\rho_0 + \frac{\zeta\delta(\alpha^2 - 4k^2)}{k} \\
&= -\alpha\beta\rho_0 + \zeta\alpha(\delta^2 - 4)
\end{aligned} \tag{A.43}$$

$$\begin{aligned}
\dot{\rho}_0 &= \xi_0\omega\left(\frac{1-s}{2c}\right) \\
&= \frac{\alpha}{\beta}\xi_0.
\end{aligned} \tag{A.44}$$

Through substitution, we see that the equation coefficients become

$$\begin{aligned}
\kappa_1 &= 0 \\
\kappa_2 &= 0 \\
\kappa_3 &= \rho_0 - \kappa_5 \\
\kappa_4 &= \frac{\xi_0}{\beta}.
\end{aligned}$$

Here, note that κ_5 and κ_6 are equivalent to the Schweighart coefficients α_{SCH} and β_{SCH}

respectively. Substituting the cross track motion initial conditions, the equations then become:

$$\begin{aligned}
\rho(t) &= (\rho_0 - \alpha_{\text{SCH}})\cos\big(\omega t\sqrt{1-s}\big) + \frac{\sqrt{1-s}}{2c}\xi_0 \sin\big(\omega t\sqrt{1-s}\big) + \alpha_{\text{SCH}}\cos(2kt) \\
\xi(t) &= \xi_0 \cos\big(\omega t\sqrt{1-s}\big) - \frac{2c}{\sqrt{1-s}}(\rho_0 - \alpha_{\text{SCH}})\sin\big(\omega t\sqrt{1-s}\big) + \beta_{\text{SCH}}\sin(2kt) \\
\eta(t) &= (lt+m)\sin(qt+\phi),
\end{aligned} \tag{A.45}$$

which is the same as the equations given in Schweighart & Sedwick (2002).

We can also check if they reduce to the solutions of the HCW equations (Equation 3.1) under the substitution that $J_2 = 0$. Here, the coefficients end up as

$$\begin{aligned}
s &= 0 & \kappa_1 &= 4\rho_0 + \frac{2\dot{\xi}_0}{\omega} \\
c &= 1 & \kappa_2 &= \xi_0 - \frac{2\dot{\rho}_0}{\omega} \\
k &= \omega & \kappa_3 &= -3\rho_0 - \frac{2\dot{\xi}_0}{\omega} \\
\alpha &= \omega & \kappa_4 &= \frac{\dot{\rho}_0}{\omega} \\
\beta &= 2 & \kappa_5 &= 0 \\
\gamma &= 3 & \kappa_6 &= 0 \\
\delta &= 1 & \kappa_7 &= \eta_0 \\
\zeta &= 0 & \kappa_8 &= \frac{\dot{\eta}_0}{\omega} \\
q &= \omega & & \\
l &= 0. & &
\end{aligned}$$

Substituting these in and setting $t_0 = 0$ for simplicity, we obtain

$$\begin{aligned}
\rho(t) &= 4\rho_0 + \frac{2\dot{\xi}_0}{\omega} - (3\rho_0 + \frac{2\dot{\xi}_0}{\omega})\cos(\omega t) + \frac{\dot{\rho}_0}{\omega}\sin(\omega t) \\
\xi(t) &= \xi_0 - \frac{2\dot{\rho}_0}{\omega} - 6\omega\rho_0 t - 3\dot{\xi}_0 t + \frac{2\dot{\rho}_0}{\omega}\cos(\omega t) + (6\rho_0 + \frac{4\dot{\xi}_0}{\omega})\sin(\omega t) \\
\eta(t) &= \eta_0 \cos(\omega t) + \frac{\dot{\eta}_0}{\omega}\sin(\omega t),
\end{aligned} \tag{A.46}$$

which are the general solutions of the HCW equations with initial conditions at $t_0 = 0$.